Properties of the Quark Gluon Plasma from Lattice QCD

DISSERTATION ZUR ERLANGUNG DES DOKTORGRADES DER NATURWISSENSCHAFTEN (DR. RER. NAT.) DER FAKULTÄT FÜR PHYSIK DER UNIVERSITÄT REGENSBURG

vorgelegt von

Simon Wolfgang Mages

aus

Regensburg

im Jahr 2015

Promotionsgesuch eingereicht am: 27. Januar 2015
Das Promotions-Kolloquium fand statt am: 2. März 2015
Die Arbeit wurde angeleitet von: Prof. Dr. Andreas Schäfer

Prüfungsausschuss:

Vorsitzender	Prof. Dr. Christoph Strunk
1. Gutachter	Prof. Dr. Andreas Schäfer
2. Gutachter	Prof. Dr. Kálmán Szabó
weiterer Prüfer	PD Dr. Falk Bruckmann

Properties of the Quark Gluon Plasma from Lattice QCD

Abstract

Quantum Chromodynamics (QCD) is the theory of the strong interaction, the theory of the interaction between the constituents of composite elementary particles (hadrons). In the low energy regime of the theory, standard methods of theoretical physics like perturbative approaches break down due to a large value of the coupling constant. However, this is the region of most interest, where the degrees of freedom of QCD, the color charges, form color-neutral composite elementary particles, like protons and neutrons. Also the transition to more energetic states of matter like the quark gluon plasma (QGP), is difficult to investigate with perturbative approaches. A QGP is a state of strongly interacting matter, which existed shortly after the Big Bang and can be created with heavy ion collisions for example at the LHC at CERN. In a QGP the color charges of QCD are deconfined.

This thesis explores ways how to use the non-perturbative approach of lattice QCD to determine properties of the QGP. It focuses mostly on observables which are derived from the energy momentum tensor, like two point correlation functions. In principle these contain information on low energy properties of the QGP like the shear and bulk viscosity and other transport coefficients. The thesis describes the lattice QCD simulations which are necessary to measure the correlation functions and proposes new methods to extract these low energy properties.

The thesis also tries to make contact to another non-perturbative approach which is Improved Holographic QCD. The aim of this approach is to use the Anti-de Sitter/Conformal Field Theory (AdS/CFT) correspondence to make statements about QCD with calculations of a five dimensional theory of gravity. This thesis contributes to that work by constraining the parameters of the model action by comparing the predictions with those of measurements with lattice QCD.

Contents

1 Introduction **1**

1.1 Standard Model . . . 1
1.2 High Energy Physics Agenda . . . 2
1.3 Lattice Efforts . . . 4
1.4 Non-Lattice Efforts . . . 5
1.5 Outline . . . 5

2 Concepts **7**

2.1 Lattice QCD . . . 7
2.1.1 Continuum Theory . . . 7
2.1.2 Discretization . . . 9
2.1.3 Smearing . . . 11
2.1.4 Finite Temperature Spectral Representation . . . 15
2.2 Energy Momentum Tensor and Transport . . . 17
2.2.1 Energy Momentum Tensor . . . 18
2.2.2 Equation of State . . . 24
2.2.3 Hydrodynamics . . . 26
2.2.4 Kubo Relations . . . 28
2.3 Wilson Flow . . . 32
2.3.1 Definition . . . 33
2.3.2 Smearing Properties . . . 34
2.3.3 Scale Setting . . . 36
2.3.4 Anisotropy Tuning . . . 37
2.3.5 Renormalization . . . 38
2.4 AdS/CFT Correspondence . . . 39
2.4.1 Maldacenas Conjecture . . . 40
2.4.2 Improved Holographic QCD . . . 41

3 Methods **43**

3.1 Effective Mass . . . 43
3.1.1 General . . . 44

3.1.2 Ground State Width . . . 45
3.2 Correlation Matrix Method . . . 49
3.2.1 Defining the Problem . . . 50
3.2.2 The Generalized Eigenvalue Problem . . . 50
3.2.3 Different Approaches . . . 55
3.2.4 Modification of the GEP . . . 59
3.2.5 SDGEP Performance . . . 62
3.2.6 Summary . . . 64
3.3 Maximum Entropy Method . . . 65
3.3.1 General . . . 66
3.3.2 Generic Default Model . . . 68
3.3.3 Modified MEM Kernels . . . 69
3.3.4 Extensions using Multiple Operators . . . 71
3.3.5 Summary . . . 74
3.4 Spectral Fit . . . 74
3.4.1 Least Squares Fit . . . 74
3.4.2 Differentially Smeared Fit . . . 76
3.5 Reconstructed Correlator . . . 78
3.5.1 Concept . . . 79
3.5.2 Sum Rules . . . 80
3.5.3 Thermal Moments . . . 81
3.6 Statistics . . . 82
3.6.1 Resampling Methods . . . 82
3.6.2 Decorrelated Data Analysis . . . 85

4 Numerical Results **88**
4.1 Data . . . 88
4.1.1 Setup . . . 88
4.1.2 Momentum Space Correlators from the Lattice . . . 89
4.1.3 Anisotropic Renormalization . . . 92
4.1.4 Discretization Errors and Scaling . . . 94
4.1.5 Assessing Finite Volume Errors . . . 96
4.2 Transport Coefficients . . . 97
4.2.1 First Order: Shear Viscosity . . . 97
4.2.2 Second Order: λ_3 . . . 104
4.2.3 Second Order: κ . . . 111
4.3 Improved Holographic QCD . . . 116
4.4 Equation of State with the Wilson flow . . . 119

5 Conclusion and Outlook **124**

A Calculation of Wilson Flow Smeared Correlators **126**

References **142**

To my family.

Chapter 1

Introduction

1.1 Standard Model

In summer 2012 the standard model of particle physics was completed: This discovery, which "is compatible with the production and decay of the Standard Model Higgs boson" [1, 28], put the last remaining piece into the puzzle. Its theoretical development started decades ago with the unification of the electromagnetic and the weak force in the 1960s [45]. Since then the incorporation of the Higgs sector and of the strong force in the theory of Quantum Chromodynamics (QCD) led to a model of the fundamental particles and interactions, whose predictions are very well confirmed by experiment.

But despite its great success there are still unanswered questions. The electroweak sector contains interesting fundamental topics such as the violation of charge-parity symmetry (CP) or neutrino masses, which are not completely understood. Also the strong sector contains a lot of intrinsically difficult questions, for example in the physics of the strongly interacting medium which is created at high energy particle collisions and modifies the interactions of the fundamental particles. And last but not least the standard model has to be incomplete in principle, because of its lack of a description of dark matter, dark energy, and the fourth fundamental force, gravity.

This thesis will be focused on theoretical tools which can be used in the framework of lattice QCD to tackle some of the questions on physics in a strongly interacting thermal medium like the quark gluon plasma (QGP), which is created at high energy heavy ion collisions. For this kind of physics it suffices to only consider the strong interaction as the energy scales of the other sectors are well separated from the temperature scale at which a QGP forms ($T_c \sim 160$ MeV) and the QCD coupling gets large ($\Lambda_{QCD} \sim 200$ MeV).

QCD is the theory of the strong interaction, which holds together composite elementary particles (hadrons) by confining all color degrees of freedom of the

constituents (partons). At zero temperature these colored degrees of freedom cannot be observed isolated, only color-neutral objects appear as asymptotic states. This property is called confinement. At finite temperatures above the QCD phase transition (or equivalently at high energies) this is not the case any more. The strength of the interaction decreases sufficiently to allow the partons to behave as free particles perturbed by an interaction. In particular color is not confined in this regime and acts similar to an electric charge. This justifies the usage of the standard method of theoretical (particle) physics, a perturbative expansion in the coupling. Therefore, in the high energy regime QCD is a well understood and tested theory. Problems emerge in the low energy regime and in the transition to the low energy regime. Then one has to use non-perturbative approaches like lattice QCD. The two properties, confinement and asymptotic freedom, make the strong sector special in the Standard Model – and difficult to handle.

1.2 High Energy Physics Agenda

In about the last decade a paradigm shift in the High Energy Physics (HEP) community took place. Before that, most people wanted to investigate physics for a clean zero temperature and density environment and if possible with low multiplicity events. The hope was that this way it is easiest to find clear signals of exciting New Physics (i.e. non Standard Model physics) which was expected to happen at a slightly higher energy than the currently available colliders could deliver. The best example for this is the search for supersymmetric extensions of the standard model, which were predicted to be detectable well inside the energy range of the next highest energy collider. However, the measurements at the LHC showed ever tighter bounds for the range of parameters in which new physics can hide from experimenters. This caused a lot of people switching to more "dirty" work with high multiplicity events at heavy ion collisions and to study the finite temperature behaviour of the fundamental theory which is in this energy range dominantly QCD.

The observable effects from the hot QCD medium may be classified into two categories. One of them contains modifications of the properties of states like heavy quarkonia propagating in the medium. The other consists of parameters of the medium itself, e.g. hydrodynamic low energy coefficients like viscosities. Observables related to both classes can be measured in experiment.

Relative probabilities for the creation of heavy bound states in heavy ion collisions compared to scaled results for proton-proton collisions are a frequently used observable related to the in-medium modifications of states (the so called nuclear modification factor R_{AA}). These measurements report e.g. a suppression of char-

monium bound states: The higher the energy, the stronger the suppression. This effect can already be explained by a simple model of a static quark-antiquark-potential with Coulomb core and linearly rising part plugged into a Schrödinger equation. At zero temperature, i.e. without the medium effects, this model will give some ground state of the system and excited states.

At finite temperature in the medium this model has to be modified to include e.g. a Debye-like screening of the strong color charges of the quarks. This modifies (weakens) the interaction at large distances which reduces the phase space available for the bound states. As the wave function of the excited states spreads over a wider spatial range, the states are more sensitive to the in-medium modification and vanish at lower temperatures than the more tightly bound ground states. But at high enough temperatures also the ground states dissolve. This explains at least qualitatively the effect of quarkonium suppression or the "melting" of the resonances. A nice review of the charmonium system is given in [93] with some more up to date experimental references in [5, 6, 27].

The other set of observables are the properties of the medium itself. At high-energy heavy ion collisions this medium is expected to be a QGP of unconfined quarks and gluons. Important observable quantities are the transport coefficients [72]. The most prominent among them is the shear viscosity η or its ratio with the entropy density η/s. This quantity is of special interest for several reasons. As viscosity it is related to dynamical dissipative processes and therefore to the generation of entropy in the QCD medium. Entropy generation in and thermalization of the QCD medium is a big problem theoretically, as the colliding heavy ions are isolated from the environment. Therefore it is not possible to sum over some degrees of freedom of the environment, which is the usual way to introduce entropy in an otherwise unitary time evolution. Additionally it was shown in string theory that a lower bound in η/s of $1/4\pi$ exists for gauge theories in the strong coupling limit. This was in particular worked out within AdS/CFT duality [56].

On the experimental side η/s has an influence on the dynamical flow behaviour of the medium and therefore on the elliptic flow parameter v_2 after freezeout with hadronization. Measurements of this parameter in heavy ion collisions suggest a value of η/s of the order of 0.12 for RHIC energies and of order 0.2 for LHC energies [43]. As energies at RHIC are smaller than those at LHC the QCD coupling is larger. This behaviour indicates that for even larger couplings than at RHIC the limit of $1/4\pi \sim 0.08$ from AdS/CFT might actually be reachable. However, the experimental values for η/s could suffer from systematic uncertainties in the extraction caused by the known large fluctuations in the initial state [79] or magnetic field effects [13]. To reliably make contact between theory and experiment, one also needs predictions from AdS/CFT with finite coupling corrections,

which might be generically large [86]. Therefore, it is important to obtain a QCD prediction at realistic coupling strength from lattice QCD.

1.3 Lattice Efforts

Since decades lattice QCD studies have been published on the topic of reconstructing transport properties of the QGP [33, 34, 55, 67, 69, 70, 76, 81, 83, 84]. There is a common problem inherent in most of these analyses: Some properties of the finite temperature integral kernel $K(\omega, \tau)$ make it difficult to access the low energy behaviour of the shear spectral function. This kernel links the spectral functions to Euclidean correlators, the quantities which are accessible by lattice QCD calculations. In the last years smearing was used very successfully to reduce the influence of high energy properties of lattice configurations and to reveal low energy properties, e.g. the topological susceptibility [8, 24, 52]. The Wilson flow [58] also has the potential to help at revealing low energy properties of QCD: It gives an analytic prescription of a method to examine a quantum field theory at a given length scale which increases with the square root of the flow time. This also gives a link to renormalization properties of the energy momentum tensor [31, 87], the correlator of which has to be measured to access the viscosities. The flow is also readily available on the lattice as an infinitesimal smearing prescription and has already found important applications, e.g. for scale setting and determination of the anisotropy [19, 20].

On a related finite temperature problem, however, the lattice QCD approach could already yield very important results, also with dynamical quarks: It could determine the equation of state [18, 22] and the fact that the nature of the phase transition at vanishing chemical potential is an analytic crossover and not a first or second order phase transition [40]. This crossover takes place between the confining hadronic phase below the temperature of the transition T_c and the quark gluon plasma phase above. Other parts of the phase diagram at non-vanishing chemical potential are difficult to access for the lattice approach because of the sign problem: It makes the Euclidean action complex and thus not suited for importance sampling, an important ingredient for every lattice QCD study [39].

Modifications of the properties of heavy bound states by the quark gluon plasma have often been calculated before. In these calculations one has to determine the spectral function of the corresponding channels. Usually, the Maximum Entropy Method (MEM) is used to do so. Most of these calculations are done in the quenched approximation [2, 34, 35, 77, 80, 90], because MEM requires data with low statistical errors to reconstruct the spectral function reliably. Now, studies using dynamical quarks become slowly available as well [21]. All these studies are

limited by the quality of the reconstruction of the spectral function.

1.4 Non-Lattice Efforts

There are a lot of different approaches to describe the physics which is relevant in the quark gluon plasma. Some are based on models or effective descriptions of resummed higher order diagrams like the Hard Thermal Loops framework [16]. The discovery of dualities between some quantum field theories and string theories made possible the development of a new class of holographic descriptions [7, 65]. While most of the dualities concern field theories which are not like QCD or only share some of its properties, some frameworks try to explicitly tailor effective string theory or super gravity descriptions to fit phenomenological needs for a description of QCD. Some of these descriptions, e.g. the framework of Improved Holographic QCD, are able to describe properties, as different as bound state energies in the confining phase and the equation of state in the deconfined phase, qualitatively or even quantitatively [46–49]. These models, however, need external input from phenomenology or lattice calculations to fix all free parameters. But after that one obtains a nonperturbative description of static properties and dynamic processes in the quark gluon plasma.

1.5 Outline

The remaining parts of the thesis are organized into three main chapters. The next chapter 2 contains an introduction of the concepts used in the thesis. This includes a general outline of lattice QCD (section 2.1), the necessary finite temperature field theory to get from lattice QCD to properties of the QGP (section 2.2), an introduction to all the properties of the Wilson flow which are relevant for the current work on improving the reconstruction of QGP properties (section 2.3), and an introduction to a completely independent way to get information on the strongly coupled QCD physics via AdS/CFT correspondence (section 2.4).

The following chapter 3 is a collection of the methods employed to get physical – mostly spectral – information from the lattice QCD data, which is measured in the form of expectation values of Euclidean correlators. The methods described include basic effective mass fits (section 3.1), the Correlation Matrix Method or Variational Method (section 3.2), the Maximum Entropy Method for reconstruction of complete spectral function without an ansatz (section 3.3), spectral fits using an ansatz (section 3.4), and a method to get some physical information directly from the correlators without any spectral reconstruction (section 3.5). This chapter also contains all the statistical methods for error estimation and dealing

with correlated data in section 3.6.

Chapter 4 is devoted to a presentation of the numerical results. First of all, the data sets and the parameters of the simulations, which are used in most of the numerical results of the thesis, are discussed (section 4.1). The physical results presented afterwards range from a determination of a set of transport coefficients of the QGP (section 4.2) and of the equation of state using the Wilson flow (section 4.4), to the comparison of lattice data with data from Improved Holographic QCD in order to help constraining the parameters involved in the framework (section 4.3).

Chapter 5 contains conclusions and an outlook.

Chapter 2

Concepts

2.1 Lattice QCD

2.1.1 Continuum Theory

To construct lattice QCD, one naturally starts from the continuum theory. QCD on continuous flat spacetime with Minkowski metric is defined by its action

$$S[\psi, \bar{\psi}, A] = \int \mathrm{d}^4 x \mathcal{L}[\psi, \bar{\psi}, A](x) \tag{2.1}$$

with the help of a Lagrangian $\mathcal{L}[\psi, \bar{\psi}, A]$. This Lagrangian can be written as a sum of the pure gauge part $\mathcal{L}_G[A]$, which depends only on the bosonic degrees of freedom A, and the fermionic part $\mathcal{L}_F[\psi, \bar{\psi}, A]$, which depends additionally on the fermionic degrees of freedom ψ and their Dirac conjugates $\bar{\psi}$. The fermionic part is minimally coupled to the gauge fields, i.e. it depends on the gauge fields only trough the covariant derivative. The gauge field of the strong interaction A lives in $\mathfrak{su}(3)$ while the fermionic fields are spinors and live in the Clifford algebra $Cl(1,3)$.

The Lagrangians have the form

$$\mathcal{L}_G[A] = \frac{1}{2g^2} \mathrm{tr}[F_{\mu\nu}[A](x) F^{\mu\nu}[A](x)] \tag{2.2}$$

$$\mathcal{L}_F[\psi, \bar{\psi}, A] = \bar{\psi}(\not{D}[A](x) + m)\psi. \tag{2.3}$$

In this Lagrangian g denotes the strong coupling constant, m the mass of the fermionic field, $\not{D}[A](x) = \not{\partial} + \mathrm{i}\not{A}(x)$ the covariant derivative in Feynman slash notation, and $F_{\mu\nu}[A](x) = -\mathrm{i}[D_\mu[A](x), D_\nu[A](x)]$ the strong field strength tensor. From the structure of the field strength tensor one directly sees a source of non-linearity of the theory: As elements of $\mathfrak{su}(3)$ the A_μ do not commute like the corresponding fields in Quantum Electrodynamics. This is also the reason for the

self-interaction of the gluon fields.[1]

Because QCD is a gauge theory, its action and Lagrangian are constructed in such a way that they do not violate gauge invariance. In addition all observables have to be constructed in a gauge invariant way. In essence this means that the action and the observables must be built from gauge invariant and covariant quantities only, like the field strength F, the covariant derivative D, and fermionic "scalar products" of the form $\bar{\psi}...\psi$.

As all the work for this thesis is done with Euclidean metric, only the analytically continued version of the theory is considered from now on. Performing this Wick-rotation one gets an Euclidean version of the action S_E.

The most important observable of a theory is usually the spectrum of the theory, i.e. the energies E_n of a set of basis states $|n\rangle$ of a Hilbert space with a well defined set of quantum numbers [44]. This observable is accessible both in the Minkovski and Euclidean version of the theories. E.g. one can measure Euclidean correlation functions $\langle O_2(t)O_1(0)\rangle_T$ of operators O_1 and O_2 at times 0 and t with a defined set of quantum numbers. The key to extract the energies E_n of the correlators is the spectral representation of the correlators

$$\langle O_2(t)O_1(0)\rangle = \sum_n \langle 0|\, O_2(t)\, |n\rangle \, \langle n|\, O_1(0)\, |0\rangle \, e^{-tE_n}. \tag{2.4}$$

Other important observables are the matrix elements of operators $\langle 0|\, O_2(t)\, |n\rangle$, which may also be extracted from Equ. (2.4). The state with the given quantum numbers and the lowest energy E_0 is the easiest one to measure, as for large Euclidean times t the sum on the right hand side of Equ. (2.4) has only a contribution from the lowest state and it is simply proportional to e^{-tE_0}.

To measure Euclidean correlators one expresses them as a path integral

$$\langle O_2(t)O_1(0)\rangle = \frac{1}{Z}\int \mathrm{D}[\Phi] e^{-S_E[\Phi]} O_2[\Phi(.,t)] O_1[\Phi(.,0)] \tag{2.5}$$

with functional equivalents $O_1[.]$ and $O_2[.]$ of the operators O_1 and O_2, the functional of the Euclidean action $S_E[.]$, the partition function

$$Z = \int \mathrm{D}[\Phi] e^{-S_E[\Phi]} \tag{2.6}$$

and the integration measure $\mathrm{D}[\Phi]$ over paths Φ. The "paths" Φ in the context of a field theory are configurations of field variables on the complete space-time manifold. In the current context of QCD the path is the configuration of the gauge

[1] All Dirac, color, and flavour indices are usually suppressed for convenience in all formulae in this work. Most of this work is done on the gluonic side of the theory where Dirac and flavour indices do not even appear in the first place.

field A and of all flavours of dynamical fermion fields ψ.

2.1.2 Discretization

The last section proposed to measure observables in QCD by the evaluation of the Euclidean path intergral

$$\langle O \rangle = \int \mathrm{D}[\Phi] e^{-S_E[\Phi]} O[\Phi]/Z. \tag{2.7}$$

In the perturbative treatment the next step would be to expand the expression in a small parameter like a coupling. But in QCD the coupling is not small at low energies which invalidates this approach.

Lattice QCD proposes to directly evaluate the path integral in Equ. (2.7). But there is a serious problem: The path integral is an infinite dimensional integral over real degrees of freedom, $\mathrm{D}[\Phi] = \prod_x \mathrm{d}\Phi(x)$. To make the dimension finite, one can put the theory on a torus to make the physical volume finite and then discretize spacetime to make the number of degrees of freedom finite. In the simplest case this gives a four dimensional hypercubic lattice Λ with periodic boundary conditions, n_t equidistant lattice sites in temporal direction, n_s equidistant lattice sites in each of the three spatial directions, and the lattice spacing a. This gives a finite dimensional integral with $\mathrm{D}[\Phi] = \prod_{n \in \Lambda} \mathrm{d}\Phi(x_n)$.

The resulting integral has still a way too high dimension to integrate numerically. But the $e^{-S_E(\Phi)}$ factor suppresses contributions of most paths exponentially such that an importance sampling Monte-Carlo procedure can work. In importance sampling the exponential factor is interpreted as a probability density function $\rho(\Phi)$ and the evaluation of the path integral becomes a sum over paths which are distributed as $\rho[\Phi] \sim e^{-S_E[\Phi]}$

$$\frac{\int \mathrm{D}[\Phi]\rho[\Phi]O[\Phi]}{\int \mathrm{D}[\Phi]\rho[\Phi]} = \frac{1}{N} \sum_{\substack{n=1 \\ P[\Phi_n] \propto \rho[\Phi]}}^{N} O[\Phi_n] + \mathcal{O}\left(\frac{1}{\sqrt{N}}\right). \tag{2.8}$$

To explicitly preserve gauge invariance at finite lattice spacing, in the discretized action the gauge fields A_μ are replaced by the gauge links $U_\mu = \exp(iaA_\mu)$. Also the integration over space becomes a sum over all lattice points and the derivatives are replaced by finite differences. The main principle, which a discretized lattice action S_E^a has to obey, is that it has to reproduce the continuum action S_E in the limit of vanishing lattice spacing

$$S_E^a \overset{a \to 0}{\to} S_E + \mathcal{O}(a^n), \tag{2.9}$$

where n is the order of the lattice artefacts. For any result obtained in a lattice simulation, a continuum limit has to be performed to get results valid for the continuum theory of QCD. That means that a series of simulations at different lattice spacings has to be performed as well as an extrapolation of the results to zero lattice spacing. The higher the order n of the lattice artefacts is, the coarser the lattice spacings can be to still get results close to the continuum. This is important to save computing time, as finer lattice spacings are more expensive to simulate. The observables measured on the lattice also contain lattice artefacts and one should try to balance both to minimize the combined error including lattice artefacts.

As the lattice action only has to correspond to the continuum action in the continuum limit, one has a lot of freedom to construct the lattice action and to engineer an action with small lattice artefacts [88]. Actions with smaller artefacts are generically more expensive to simulate, so again one faces a trade-off between lattice artefacts and a cheap action. In this thesis an (an)isotropic version of a tree level Symanzik improved gauge action and a Wilson fermion action are used:

$$\begin{aligned} S_G &= \beta \left\{ \frac{1}{\xi_g} \sum_{n,i>j} \{c_0^s P_{ij}(n) + c_1^s (R_{ij}(n) + R_{ji}(n))\} \right. \\ &\quad \left. + \xi_g \sum_{n,k} \left(c_0^t P_{k4}(n) + c_1^t R_{k4}(n) + c_2^t R_{4k}(n) \right) \right\}, \qquad (2.10) \\ P_{\mu\nu}(n) &= 1 - \frac{1}{3} ReTr\{U_\mu(n) U_\nu(n+\hat{\mu}) U_\mu^\dagger(n+\hat{\nu}) U_\nu^\dagger(n)\}, \qquad (2.11) \\ R_{\mu\nu}(n) &= 1 - \frac{1}{3} ReTr\{U_\mu(n) U_\mu(n+\hat{\mu}) U_\nu(n+2\hat{\mu}) \\ &\quad \times U_\mu^\dagger(n+\hat{\mu}+\hat{\nu}) U_\mu^\dagger(n+\hat{\nu}) U_\nu^\dagger(n)\}, \qquad (2.12) \\ S_F &= \sum_{n,m} \bar{\psi}(n) K(n,m) \psi(n), \qquad (2.13) \end{aligned}$$

$$\begin{aligned} K &= \delta_{n,m} - \kappa_t \left\{ (1-\gamma_4) U_4(n) \delta_{n+\hat{4},m} + (1-\gamma_4) U_4^\dagger(n+\hat{4}) \delta_{n-\hat{4},m} \right\} \\ &\quad - \kappa_s \sum_i \left\{ (r-\gamma_i) U_i(n) \delta_{n+\hat{i},m} + (r-\gamma_i) U_i^\dagger(n+\hat{i}) \delta_{n-\hat{i},m} \right\} \\ &\quad - \kappa_s \left\{ c_t \sum_i \sigma_{4i} F_{4i}(n) + r c_s \sum_{i>j} \sigma_{ij} F_{ij}(n) \right\} \delta_{n,m}, \qquad (2.14) \\ \xi_f &= \frac{\kappa_t u_t}{\kappa_s u_s}, c_t = \frac{1}{u_s u_t^2}, c_s = \frac{1}{u_s^3}. \qquad (2.15) \end{aligned}$$

More details on these actions are given in [91]. In most parts of the thesis, the gauge anisotropy ξ_g and the fermionic anisotropy ξ_f parameters are set to 1, i.e. the isotropic version is used, unless stated otherwise.

The fermionic fields in the action are Grassmann valued. Therefore the integrals over the fermionic degrees of freedom simplify drastically and they can be integrated out. This process results in an effective theory where the gauge links U are the only degrees of freedom. But the effective action contains the so called fermion determinant. It is the determinant of the Dirac operator, which is in the discretized case a sparse $(12n_s^3n_t)^2$ matrix, making it very expensive to evaluate. In addition it makes the effective action non-local, which removes the possibility to use some algorithms, e.g. the multilevel algorithm for noise reduction presented in the next section 2.1.3. Even though the fermion determinant is needed for the representation of the full dynamics of QCD on the lattice, it is often set to 1. This cheaper approximation is called "quenched approximation".

In principle, one also has to remove the other ingredient used to make the path integral finite dimensionally: The finite space-time volume. The limit of infinite spacial volume has always to be performed, or at least a check that changing the spatial volume significantly does not change the results. The Euclidean temporal direction, however, is special. The formal equivalence between Euclidean field theory and statistical physics makes it possible to identify the finite size of the periodic Euclidean temporal direction as the inverse temperature $\beta = 1/T$ of the field theory. This enables the study of finite temperature field theory, when one does not perform the limit of infinite β and keeps β finite instead.

2.1.3 Smearing

Lattice QCD as outlined in the last section 2.1.2 has the feature that all statistical errors scale like $const N^{-1/2}$ with the number of configurations N. This enables the use of a straightforward "technique" to obtain more precise results with less statistical errors: Drowning the problem in computing power. But this strategy entails some problems: Computing power is a finite resource and especially for the expensive simulations with dynamical fermions at the physical point this is clearly not a feasible solution. Also for some problems the *const* in the scaling law is large such that an unrealistically high value of N is needed to obtain errors of the results in physically interesting regimes of at most a few percent. This is the case for example for correlators of the energy momentum tensor which are interesting for transport properties of the quark gluon plasma: There the value of the correlator decays for dimensional reasons as τ^{-5} for small distances in Euclidean time, which results in a very poor signal to noise ratio for the correlator at large distances where the transport properties are encoded.

There are two possible solutions how to minimize the statistical noise [62, 66]:

- Modification of the simulation or

- Modification of the measurement.

The first solution is chosen in the noise reduction technique called "multilevel algorithm"[2]. The second alternative leads to smearing techniques.

The multilevel algorithm is sketched in Fig. 2.1. In the standard Monte Carlo simulation the complete lattice is updated in every step and a correlator is measured. The error scales as $N^{-1/2}$. In the multilevel algorithm the complete lattice is updated only every f-th step. Between the big updates, the two subvolumes – each containing one operator of the correlator – are updated independently with a layer of the lattice fixed as boundary condition between the two subvolumes. Such updates are possible for a local lattice action. The correlator only depends on the fields on the boundary and therefore can be calculated also after averaging the operator measurements on the independently updated configurations. This reduces the statistical error on each correlator measurement by a factor of $f^{-1/2}$. The correlator is then only averaged over N/f averages of the measured operators. But in total, the error then scales approximately as $(N/f)^{-1/2}(f^{-1/2})^2 = (fN)^{-1/2}$, which means that it can be a factor of $f^{-1/2}$ smaller. This significant error reduction is only valid if a large part of the statistical error comes from the short distance fluctuations around an operator in one compartment. This strategy has been used successfully for pure Yang-Mills theory in [62, 66, 67, 70]. For full QCD with dynamical quarks this prescription cannot be applied, because the action is non-local due to the fermion determinant.

Smearing prescriptions on the other hand do not modify the simulation but instead the measurement of the observables and are independent of the locality of the action. The effect of smearing is sketched in Fig. 2.2. Smearing also averages over short distance fluctuations in the measurement of the observables, from which correlators can be built, like the multilevel algorithm. But unlike the multilevel algorithm, smearing averages over the short distance fluctuations on a single configuration rather than over the fluctuations over configurations separated in simulation time. Smearing can be implemented in two different ways: One can construct an operator which is extended over a larger range of the lattice and is not local anymore or one can construct a lattice of smeared links which incorporate the information of their unsmeared neighbours and measure the standard local operators on them.[3] As smearing makes the operators non-local, the results are not identical to the ones obtained in continuum theory with local operators. They are

[2]This "multilevel algorithm" has nothing to do with the "multilevel method" or "multigrid method" to invert the lattice Dirac operator explained in e.g. [41, 42]

[3]The smearing described here is different from the smearing in the action, which is used to improve scaling properties of the action. The smearing here is only applied for the measurement on configurations generated with any action, smeared or unsmeared.

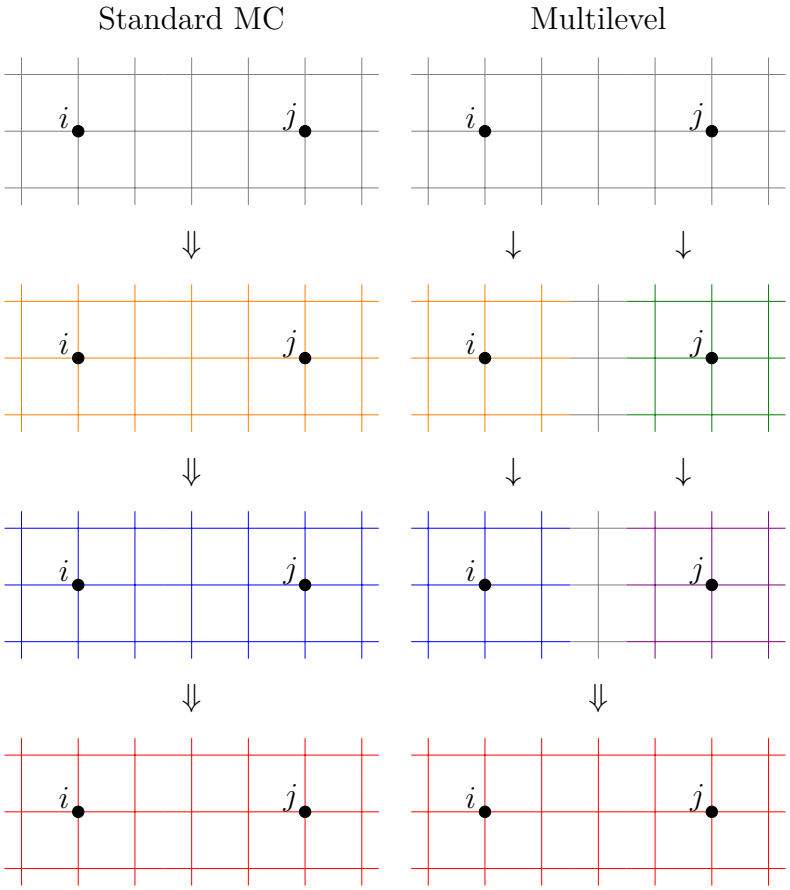

Figure 2.1: The multilevel algorithm compared to the standard Monte Carlo procedure. For details see main text.

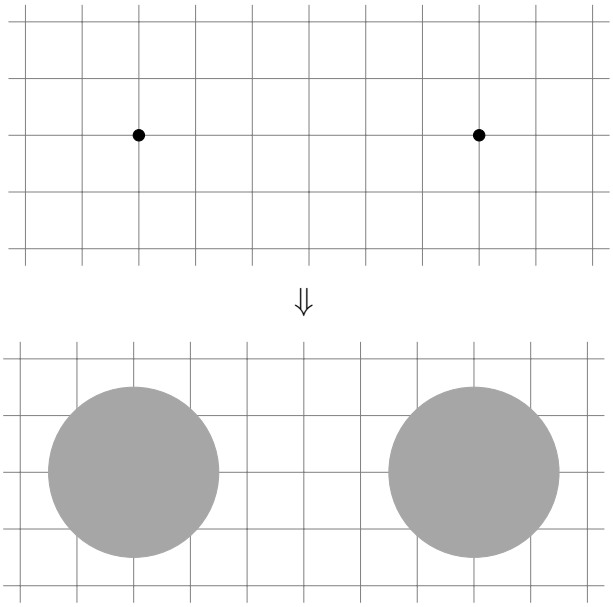

Figure 2.2: The effect of smearing on the measurement of an operator compared to the unsmeared counterpart. For details see main text.

some observable with the same quantum numbers but without the short distance contributions. To obtain the proper observable in the continuum limit and to recover the full ultraviolet contributions, one has to apply the smearing with an effective smearing radius which vanishes in the continuum limit.

A widely used smearing procedure is stout smearing [75]. Like all gauge smearing procedures stout smearing is a prescription how to average over a local set of gauge links to produce a smeared or "fat" link. This new link U'_μ is a function of the old links U_μ and defined as

$$U'_\mu = \mathrm{e}^{\mathrm{i}Q_\mu} U_\mu, \tag{2.16}$$

$$Q_\mu = \frac{\mathrm{i}}{2}\left(\Omega^\dagger_\mu - \Omega_\mu - \frac{1}{3}\mathrm{tr}[\Omega^\dagger_\mu - \Omega_\mu]\right), \tag{2.17}$$

$$\Omega_\mu = \left(\rho_{Stout} \sum_{\nu \neq \mu} C_{\mu\nu}\right) U^\dagger_\mu, \tag{2.18}$$

with $C_{\mu\nu}$ being the staple in the $\mu\nu$ plane. One can of course iterate the smearing procedure N_{Stout} times to produce even smoother field configurations. The resulting smearing radius is then given by

$$r_{smear} = a\sqrt{8\rho_{Stout} N_{Stout}}. \tag{2.19}$$

The smearing used in this thesis is stout link smearing, if not stated differently.

2.1.4 Finite Temperature Spectral Representation

Having defined lattice QCD as Euclidean field theory on a finite and discretized space time suitable for numerical treatment in the computer, it is now important to know how the Euclidean observables in these simulations relate to the Minkovski observables of real physics. In this context one often introduces spectral representations or spectral functions. This section presents some relations of thermal field theory which are important to understand the measurements done on the lattice. For a more detailed discussion the references [14] and [57] can be recommended.

In this presentation only the bosonic case is considered as this case applies to all the correlators of the energy momentum tensor which will be the main observables in this thesis. Most concepts carry over to the fermionic case and whenever important formulae are derived and needed in the thesis, they will be stated in the fermionic version as well.

Given two bosonic field operators $\hat{\phi}_i(x)$ and $\hat{\phi}_j(x)$ at Minkovski space time point $x = (t, \vec{x}) = (x^0, \vec{x})$ one can define the usual Green's functions and correlators

$$\Pi^{>}_{ij}(q) = \int \mathrm{d}t\mathrm{d}^3\vec{x} e^{iq\cdot x} \left\langle \hat{\phi}_i(x)\hat{\phi}^\dagger_j(0)\right\rangle \tag{2.20}$$

$$\Pi^{<}_{ij}(q) = \int \mathrm{d}t\mathrm{d}^3\vec{x} e^{iq\cdot x} \left\langle \hat{\phi}^\dagger_j(0)\hat{\phi}_i(x)\right\rangle \tag{2.21}$$

$$\Pi^{R}_{ij}(q) = i\int \mathrm{d}t\mathrm{d}^3\vec{x} e^{iq\cdot x} \left\langle \left[\hat{\phi}_i(x), \hat{\phi}^\dagger_j(0)\right]\theta(t)\right\rangle \tag{2.22}$$

$$\rho_{ij}(q) = \int \mathrm{d}t\mathrm{d}^3\vec{x} e^{iq\cdot x} \left\langle \frac{1}{2}\left[\hat{\phi}_i(x), \hat{\phi}^\dagger_j(0)\right]\right\rangle \tag{2.23}$$

with $\Pi^R_{ij}(q)$ called the retarded correlator, $\rho_{ij}(q)$ the spectral function, the Minkovski momentum $q = (q^0, \vec{q}) = (\omega, \vec{q})$, and the Heaviside function θ.

In Euclidean space one can only measure the Euclidean correlator

$$\Pi^{E}_{ij}(\tilde{q}) = \int_0^\beta \mathrm{d}\tau\mathrm{d}^3\vec{x} e^{i\tilde{q}\cdot\tilde{x}} \left\langle \hat{\phi}_i(\tilde{x})\hat{\phi}^\dagger_j(0)\right\rangle \tag{2.24}$$

where $\tilde{q} = (i\tilde{q}_0, \vec{q})$ is an Euclidean momentum, $\tilde{x} = (-i\tau, \vec{x}) = (-i\tilde{x}_0, \vec{x})$ is an Euclidean position, and $\beta = 1/T$ the inverse temperature.

From these definitions and the integral representation of the Heaviside function

$$\theta(t) = i\int_{-\infty}^{\infty} \frac{\mathrm{d}\omega}{2\pi}\frac{e^{-i\omega t}}{\omega + i0^+} \tag{2.25}$$

one finds the relation for the retarded correlator and the spectral function

$$\Pi^R_{ij}(q) = \int_{-\infty}^{\infty} \frac{\mathrm{d}p^0}{\pi}\frac{\rho_{ij}(p^0, \vec{q})}{p^0 - q^0 + i0^+}. \tag{2.26}$$

Using

$$\frac{1}{\Delta \pm i0^+} = P\left(\frac{1}{\Delta}\right) \mp i\pi\delta(\Delta) \tag{2.27}$$

with the principal value P gives then the simple relation

$$\Im\Pi^R_{ij}(q) = \rho_{ij}(q). \tag{2.28}$$

Also, by plugging in the definition of the thermal expectation value and of the Heisenberg operators

$$\langle . \rangle = Tr\left[e^{-\beta\hat{H}}.\right] \tag{2.29}$$

$$\hat{O}(t,\vec{x}) = e^{it\hat{H}}\hat{O}(0,\vec{x})e^{-it\hat{H}} \tag{2.30}$$

and inserting complete sets of energy eigenstates into the definitions of $\Pi^>_{ij}(q)$ and $\Pi^<_{ij}(q)$, one gets a Kubo-Martin-Schwinger (KMS) relation between them

$$\Pi^>_{ij}(q) = e^{\beta q^0}\Pi^<_{ij}(q). \tag{2.31}$$

This directly relates them also to the spectral function

$$\rho_{ij}(q) = \frac{1}{2}\left(\Pi^>_{ij}(q) - \Pi^<_{ij}(q)\right) \tag{2.32}$$

$$= \frac{1}{2}\left(1 - e^{-\beta q^0}\right)\Pi^>_{ij}(q). \tag{2.33}$$

By inverse Fourier transformation of Equ. (2.20) and analytic continuation of the field operators one can additionally show for the spatially Fourier transformed Euclidean correlator

$$C(\tau,\vec{q}) := \int \mathrm{d}^3\vec{x}e^{i\vec{q}\cdot\vec{x}}\left\langle\hat{\phi}_i(\tilde{x})\hat{\phi}^\dagger_j(0)\right\rangle \tag{2.34}$$

$$= \int \mathrm{d}^3\vec{x}e^{i\vec{q}\cdot\vec{x}}\int\frac{\mathrm{d}^4p}{(2\pi)^4}e^{-ip\cdot\tilde{x}}\Pi^>_{ij}(p) \tag{2.35}$$

$$= \int_{-\infty}^{\infty}\frac{\mathrm{d}p^0}{2\pi}e^{-p^0\tau}\Pi^>_{ij}(p^0,\vec{q}) \tag{2.36}$$

$$= \int_{-\infty}^{\infty}\frac{\mathrm{d}p^0}{\pi}\frac{e^{-p^0\tau}}{1-e^{-\beta p^0}}\rho_{ij}(p^0,\vec{q}) \tag{2.37}$$

Plugging this into the defining equation of the Euclidean correlator Equ. (2.24) and performing the τ integral one arrives at

$$\Pi^E_{ij}(\tilde{q}) = \int_{-\infty}^{\infty}\frac{\mathrm{d}p^0}{\pi}\frac{\rho_{ij}(p^0,\vec{q})}{p^0 - i\tilde{q}_0}. \tag{2.38}$$

If $\hat{\phi}_i = \hat{\phi}_j^\dagger$, which is true in many cases of interest, the spectral function is antisymmetric in $p^0 \to -p^0$ and Equ. (2.37) can be simplified to

$$C_h(\tau, \vec{q}) = \int_0^\infty \frac{\mathrm{d}\omega}{\pi} \frac{\cosh\left(\left(\frac{\beta}{2} - \tau\right)\omega\right)}{\sinh\left(\frac{\beta}{2}\omega\right)} \rho_{ij}(\omega, \vec{q}). \tag{2.39}$$

This equation can be understood as a finite temperature and continuous spectrum generalization of the basic Equ. (2.4). It is essential for lattice studies of spectral properties of a theory as it connects the spectral function of Minkovski space-time on the right hand side with an observable which is directly accessible in Euclidean space-time on the left hand side. In principle, an accurate measurement of the left hand side followed by inversion of the integral transformation can yield the spectral function. However, this inversion leads to a lot of technical problems as discussed in detail in section 3.3.

Equs. (2.37) and (2.39) are valid for bosonic operators. This already covers a large class of interesting observables including bilinears of fermionic operators which couple to mesons. For baryons one needs the analogous relation for fermionic operators which read

$$C^F(\tau, \vec{q}) := \int_{-\infty}^\infty \frac{\mathrm{d}p^0}{\pi} \frac{e^{-p^0\tau}}{1 + e^{-\beta p^0}} \rho_{ij}(p^0, \vec{q}) \tag{2.40}$$

$$C_h^F(\tau, \vec{q}) := \int_0^\infty \frac{\mathrm{d}\omega}{\pi} \frac{\sinh\left(\left(\frac{\beta}{2} - \tau\right)\omega\right)}{\sinh\left(\frac{\beta}{2}\omega\right)} \rho_{ij}(\omega, \vec{q}). \tag{2.41}$$

These are the same relations as for bosonic operators up to a sign. This sign is exactly the sign difference between the Bose-Einstein and Fermi-Dirac distributions and cause the difference in statistics. Equ. (2.41) is again valid for operators which satisfy $\hat{\phi}_i = \hat{\phi}_j^\dagger$.

In later parts of the thesis the spatially Fourier transformed Euclidean correlators $C(\tau, \vec{q})$ will be called simply Euclidean correlators as the completely Fourier transformed Euclidean correlators $\Pi^E(\tilde{q})$ will not appear again.

2.2 Energy Momentum Tensor and Transport

As stated in the introduction, strongly interacting matter at high energies is in a quark gluon plasma state. This state behaves in first approximation more like an interacting fluid than a gas of quasi free particles. To describe such a medium in relativistic parameter regions the language of relativistic hydrodynamics can be used. In experiments at heavy ion colliders it was determined that the medium created in such collisions in fact behaves like a nearly perfect fluid. Relativistic

hydrodynamics is formulated in terms of one of the most basic observables of any physical theory, the energy momentum tensor.[4]

2.2.1 Energy Momentum Tensor

The energy momentum tensor is a symmetric[5] tensor field $T_{\mu\nu}(x)$ at $x = (\tau, \vec{x})$. It is the conserved Noether current associated with space-time translations

$$\nabla_\nu T^{\mu\nu}(x) = 0. \tag{2.42}$$

On the diagonal, its entries are the energy density $T^{00} = \epsilon$ and the pressure $T^{ii} = P$. The off diagonal elements are the momentum density $T^{0i} = T^{i0}$ and the shear stress or momentum flux $T^{ij} = T^{ji}$. As only flat Euclidean space-time is considered in most parts of this thesis, usually there is no distinction made between covariant and contravariant indices and covariant and partial derivatives.

For pure gauge theories it is given as

$$T_{\mu\nu}(x) = F_{\mu\sigma}(x)F_{\nu\sigma}(x) - \frac{1}{4}\delta_{\mu\nu}F_{\rho\sigma}(x)F_{\rho\sigma}(x), \tag{2.43}$$

where $F_{\mu\nu}(x)$ is the field-strength tensor and a trace over the suppressed color indices is understood. This expression is traceless in the classical theory. In quantum theory $F_{\mu\sigma}F_{\nu\sigma}$ and $F_{\rho\sigma}F_{\rho\sigma}$ renormalize differently and there is a contribution to the trace from the conformal anomaly. Most observables built from the energy momentum tensor, which are considered in this thesis, are built from the traceless part $\Theta_{\mu\nu}$ of the full $T_{\mu\nu}$ only. Therefore in the following the renormalization of the traceless contribution is discussed only. A method to renormalize the trace part will be discussed separately in section 2.3.5.

General Non-perturbative Anisotropic Renormalization Strategy

This prescription is quite general and is therefore discussed for a general setting. In the end it uses an existing set of renormalization factors of the isotropic lattice to determine the absolute scale of renormalization factors.

Let O_i be a set of N multiplicatively renormalizable observables[6], $\hat{O}_i$ the corresponding set of discretized operators for the O_i, and Z_i a set of renormalization

[4]Some authors prefer the term "stress tensor" instead of "energy momentum tensor".

[5]In most cases of relevance, like the standard model and general relativity, the energy momentum tensor is symmetric. There are, however, exceptions to this rule, e.g. in generalizations of general relativity like Einstein-Cartan theory.

[6]This is not a restriction of this prescription as one can always find a basis of multiplicatively renormalizable observables.

factors such that

$$\langle O_i \rangle = Z_i \langle \hat{O}_i \rangle. \tag{2.44}$$

In general, the renormalization factors and the lattice expectation values of the discretized operators depend on the discretization, while the observables are discretization independent.

$$Z_i = Z_i(a, \xi), \tag{2.45}$$
$$\langle \hat{O}_i \rangle = \langle \hat{O}_i \rangle (a, \xi), \tag{2.46}$$
$$O_i = O_i. \tag{2.47}$$

As the observables do not depend on the discretization, they have in particular to be equal for different choices of the discretization[7], e.g. for different anisotropies[8]. This gives us

$$\begin{aligned} \langle O_i \rangle &= Z_i(\xi_0) \langle \hat{O}_i \rangle (\xi_0) \\ &= Z_i(\xi_1) \langle \hat{O}_i \rangle (\xi_1). \end{aligned} \tag{2.48}$$

As one can measure the discretized expectation values, Equ. (2.48) is sufficient to measure at any given temperature the ratios of the renormalization factors $Z_i(\xi_0)/Z_i(\xi_1)$, provided that the expectation value of the observables is not zero (as is the case for the energy momentum tensor).

But also the case of vanishing expectation values can be resolved. The simplest option is to use correlators at a finite physical distance.

Let $o_i(x)$ be the four-density corresponding to the operator O_i, i.e.

$$O_i = \int \mathrm{d}^4 x o_i(x), \tag{2.49}$$

and $\hat{o}_i(x)$ the discretized density. Both have the same renormalization constant Z_i

$$\langle o_i(x) \rangle = Z_i \langle \hat{o}_i(x) \rangle. \tag{2.50}$$

Then one can construct $N(N+1)/2$ independent correlators $C_{ij}(\tau)$[9] which are

[7] This statement is strictly true only in the continuum limit. In the following it is assumed that the lattices are fine enough.

[8] As only the case of different anisotropies is covered here, the lattice spacing argument a is dropped in the following.

[9] This can also be done with correlators separating the operators in spatial direction.

new observables still only depending on the same N renormalization factors Z_i. The correlators may be defined as

$$C_{ij}(\tau) := \int \mathrm{d}^3\langle \vec{x} o_i(x) o_j(0)\rangle \tag{2.51}$$

$$= Z_i Z_j \int \mathrm{d}^3\vec{x}\langle \hat{o}_i(x)\hat{o}_j(0)\rangle. \tag{2.52}$$

Like the observables O_i, their correlators $C_{ij}(\tau)$ are independent of the discretization, their discretized densities, however, are again discretization dependent:

$$C_{ij}(\tau) = C_{ij}(\tau) \tag{2.53}$$

$$\hat{o}_i(x) = \hat{o}_i(\xi, x) \tag{2.54}$$

Following the same arguments which lead to Equ. (2.48) one gets here

$$\begin{aligned} C_{ij}(\tau) &= Z_i(\xi_0) Z_j(\xi_0) \int \mathrm{d}^3 x \langle \hat{o}_i(x)\hat{o}_j(0)\rangle(\xi_0) \\ &= Z_i(\xi_1) Z_j(\xi_1) \int \mathrm{d}^3 x \langle \hat{o}_i(x)\hat{o}_j(0)\rangle(\xi_1). \end{aligned} \tag{2.55}$$

Equ. (2.55) is now an overdetermined system of equations for the ratios of renormalization factors $Z_i(\xi_0)/Z_i(\xi_1)$ which allows for a fit of these ratios. The choice of τ for this system sets the renormalization scale.

Having determined the ratios of renormalization factors non-perturbatively, of course one still has to get the absolute scale of the factors. For this it is usually the most convenient choice to simulate using an isotropic reference lattice because usually some of the factors are degenerate. Such a case allows also for the determination of ratios between some of the anisotropic renormalization factors and to build some observables which do not renormalize multiplicatively in the anisotropic but in the isotropic setting. For all other observables and to get the absolute scale of the renormalization factors one needs the isotropic factors from somewhere else.

Renormalization Structure of the Energy Momentum Tensor

On the isotropic lattice the renormalized traceless energy-momentum tensor is

$$\Theta^{iso}_{\mu\nu} = Z^{iso}_{\mu\nu}\theta^{iso}_{\mu\nu} \tag{2.56}$$

$$\theta^{iso}_{\mu\nu} = F^{iso}_{\mu\sigma}F^{iso}_{\nu\sigma} - \frac{1}{4}\delta_{\mu\nu}F^{iso}_{\rho\sigma}F^{iso}_{\rho\sigma}, \tag{2.57}$$

where $Z^{iso}_{\mu\nu} = Z^{diag}$ for $\mu = \nu$, $Z^{iso}_{\mu\nu} = Z^{rest}$ for $\mu \neq \nu$, and $F^{iso}_{\mu\nu}$ is a discretization of the field-strength tensor on an isotropic lattice.

On the anisotropic lattice this has to be modified introducing different renormalization factors depending on the anisotropy $\xi = a_s/a_t$. The operators have to be built from irreducible representations of the remaining cubic symmetry group of the lattice. Every representation gets its individual renormalization factor. The relevant building blocks in terms of quadratics of the anisotropic field strength tensor $F^{\overline{iso}}_{\mu\nu}$ are given in Tab. 2.1.

operators	E and B	Z factor
$\sum_i {F^{\overline{iso}}_{0i}}^2$	$\sum_i E_i^2$	Z^{EE_0}
${F^{\overline{iso}}_{0i}}^2 - {F^{\overline{iso}}_{0j}}^2$	$E_i^2 - E_j^2$	Z^{EE_1}
$F^{\overline{iso}}_{0i} F^{\overline{iso}}_{0j}$	$E_i E_j$	Z^{EE_2}
$\sum_{i<j} {F^{\overline{iso}}_{ij}}^2$	$\sum_k B_k^2$	Z^{BB_0}
${F^{\overline{iso}}_{ij}}^2 - {F^{\overline{iso}}_{jk}}^2$	$B_k^2 - B_i^2$	Z^{BB_1}
$F^{\overline{iso}}_{ij} F^{\overline{iso}}_{jk}$	$B_k B_i$	Z^{BB_2}
$F^{\overline{iso}}_{0i} F^{\overline{iso}}_{ji}$	$E_i B_k$	Z^{EB}

Table 2.1: Operators belonging to irreducible representations of the cubic group in terms of the anisotropic field strength tensor $F^{\overline{iso}}_{\mu\nu}$.

Therefore one has

$$\Theta^{\overline{iso}}_{00} = Z^{EE_0}\theta^{EE_0}_{00} + Z^{BB_0}\theta^{BB_0}_{00} \tag{2.58}$$

$$\Theta^{\overline{iso}}_{kk} = Z^{EE_0}\theta^{EE_0}_{kk} + Z^{BB_0}\theta^{BB_0}_{kk} + Z^{EE_1}\theta^{EE_1}_{kk} + Z^{BB_1}\theta^{BB_1}_{kk} \tag{2.59}$$

$$\Theta^{\overline{iso}}_{0k} = Z^{EB}\theta^{EB}_{0k} \tag{2.60}$$

$$\Theta^{\overline{iso}}_{kl} = Z^{EE_2}\theta^{EE_2}_{kl} + Z^{BB_2}\theta^{BB_2}_{kl}, \tag{2.61}$$

where

$$\theta_{00}^{EE_0} = +\frac{1}{2}\sum_i \overline{F_{0i}^{iso}}^2 = +\frac{1}{2}\sum_i E_i^2 \tag{2.62}$$

$$\theta_{00}^{BB_0} = -\frac{1}{2}\sum_{i<j} \overline{F_{ij}^{iso}}^2 = -\frac{1}{2}\sum_l B_l^2 \tag{2.63}$$

$$-\frac{1}{3}\theta_{00}^{EE_0} = \theta_{kk}^{EE_0} = -\frac{1}{6}\sum_i \overline{F_{0i}^{iso}}^2 = -\frac{1}{6}\sum_i E_i^2 \tag{2.64}$$

$$-\frac{1}{3}\theta_{00}^{BB_0} = \theta_{kk}^{BB_0} = +\frac{1}{6}\sum_{i<j} \overline{F_{ij}^{iso}}^2 = +\frac{1}{6}\sum_k B_k^2 \tag{2.65}$$

$$\theta_{kk}^{EE_1} = +\frac{1}{3}(2\ \overline{F_{0k}^{iso}}^2 - \sum_{i\neq k} \overline{F_{0i}^{iso}}^2) = +\frac{1}{3}(2E_k^2 - \sum_{i\neq k} E_i^2) \tag{2.66}$$

$$\theta_{kk}^{BB_1} = -\frac{1}{3}(2\sum_{i<j,i\neq k\neq j} \overline{F_{ij}^{iso}}^2 - \sum_{i\neq k} \overline{F_{ki}^{iso}}^2) = -\frac{1}{3}(2B_k^2 - \sum_{j\neq k} B_j^2) \tag{2.67}$$

$$\theta_{0k}^{EB} = \sum_{l\neq k} \overline{F_{0l}^{iso}}\,\overline{F_{kl}^{iso}} = \sum_{l\neq k}\sum_{k\neq i\neq l} E_l B_i \tag{2.68}$$

$$\theta_{kl}^{EE_2} = \overline{F_{k0}^{iso}}\,\overline{F_{l0}^{iso}} = E_k E_l \tag{2.69}$$

$$\theta_{kl}^{BB_2} = \sum_{k\neq i\neq l} \overline{F_{ki}^{iso}}\,\overline{F_{li}^{iso}} = B_l B_k. \tag{2.70}$$

This gives a total of 7 Z factors in the anisotropic case instead of 2 in the isotropic case: In the isotropic case $Z^{EE_0} = Z^{BB_0} = Z^{EE_1} = Z^{BB_1} = Z^{diag}$ and $Z^{EB} = Z^{EE_2} = Z^{BB_2} = Z^{rest}$.

If the discussion is restricted to the diagonal elements of $\Theta_{\mu\nu}^{\overline{iso}}$, there are 4 relevant factors Z^{EE_0}, Z^{EE_1}, Z^{BB_0}, and Z^{BB_1} in the anisotropic case instead of just the single factor Z^{diag} of the isotropic case.

Renormalization of Expectation Values

In expectation values $\langle\Theta_{kk}^{XX_1}\rangle = 0$ due to symmetry between the three spatial directions and $\langle\Theta_{0k}^{EB}\rangle = \langle\Theta_{kl}^{XX_2}\rangle = 0$ due to symmetry between positive and negative directions of a single spatial dimension. Therefore for the renormalization of the expectation value of the energy momentum tensor itself only the two Z factors Z^{XX_0} are important.

For the determination of these two diagonal renormalization factors, one can make use of [17] where the renormalized entropy density $s = (\epsilon + p)/T$ is calculated.[10] This known value can then be used to directly calculate the diagonal

[10] As s is very small below T_c, this renormalization introduces a large uncertainty. However, as the renormalization factor is independent of the temperature, one can perform a simulation with the same β above T_c which allows to determine the renormalization factor with reasonable accuracy already using only limited statistics.

isotropic renormalization factor Z^{diag} via

$$\begin{aligned}\frac{sT}{4} =& \langle \Theta_{11}^{iso} \rangle \\ =& Z^{diag} \langle \theta_{11}^{iso} \rangle \end{aligned} \tag{2.71}$$

by measuring $\langle \theta_{11}^{iso} \rangle$ on an isotropic lattice. To get Z^{XX_0} one can measure $\langle \theta_{11}^{XX_0} \rangle$ on both the isotropic lattice and the anisotropic lattice and directly use

$$Z^{XX_0} \langle \theta_{11}^{XX_0} \rangle = Z^{diag} \langle \theta_{11}^{XX_0,iso} \rangle. \tag{2.72}$$

For the determination of Z^{XX_1} one can also use the degeneracy of the factors in the isotropic Z^{diag}. But as $\langle \Theta_{kk}^{XX_1} \rangle = 0$ one has to consider one correlator, e.g.

$$\left(Z^{XX_1}\right)^2 \int \mathrm{d}\vec{x} \langle \theta_{11}^{XX_1}(\tau, \vec{x}) \theta_{11}^{XX_1}(0, \vec{0}) \rangle = \left(Z^{diag}\right)^2 \int \mathrm{d}\vec{x} \langle \theta_{11}^{XX_1,iso}(\tau, \vec{x}) \theta_{11}^{XX_1,iso}(0, \vec{0}) \rangle, \tag{2.73}$$

or more correlators and solve the overdetermined system, as described above.

By using the three equations (or alternatively an overdetermined system with cross-correlators like in Equ. (2.48))

$$\left(Z^{EE_2}\right)^2 \int \mathrm{d}\vec{x} \langle \theta_{12}^{EE_2}(\tau, \vec{x}) \theta_{12}^{EE_2}(0, \vec{0}) \rangle = \left(Z^{rest}\right)^2 \int \mathrm{d}\vec{x} \langle \theta_{12}^{EE_2,iso}(\tau, \vec{x}) \theta_{12}^{EE_2,iso}(0, \vec{0}) \rangle, \tag{2.74}$$

$$\left(Z^{BB_2}\right)^2 \int \mathrm{d}\vec{x} \langle \theta_{12}^{BB_2}(\tau, \vec{x}) \theta_{12}^{BB_2}(0, \vec{0}) \rangle = \left(Z^{rest}\right)^2 \int \mathrm{d}\vec{x} \langle \theta_{12}^{BB_2,iso}(\tau, \vec{x}) \theta_{12}^{BB_2,iso}(0, \vec{0}) \rangle, \tag{2.75}$$

$$\left(Z^{EB}\right)^2 \int \mathrm{d}\vec{x} \langle \theta_{01}^{EB}(\tau, \vec{x}) \theta_{01}^{BB_2}(0, \vec{0}) \rangle = \left(Z^{rest}\right)^2 \int \mathrm{d}\vec{x} \langle \theta_{01}^{EB,iso}(\tau, \vec{x}) \theta_{01}^{EB,iso}(0, \vec{0}) \rangle \tag{2.76}$$

one can find the relative factors Z^{EE_2}/Z^{BB_2} and Z^{EB}/Z^{BB_2} by using the degeneracy of the isotropic factors. But for the absolute factor one has to use a different ansatz than for Z^{diag}, because all the scalar expectation values proportional to Z^{rest} vanish in that case.

The correlators of the energy momentum tensor can be written using a general tensor decomposition as [55, 67]

$$\langle \Theta_{ij}(x) \Theta_{kl}(y) \rangle = A(x-y)(\delta_{ik}\delta_{jl} + \delta_{il}\delta_{jk}) + B(x-y)\delta_{ij}\delta_{kl}, \tag{2.77}$$

where i, j, k, and l are spatial indices. This statement is valid for the continuum and makes use of periodic boundary conditions and the cubic symmetry in the spatial directions. This makes it possible to rewrite correlators of non-diagonal

spatial components in terms of correlators of diagonal components of the energy momentum tensor and to relate the diagonal and non-diagonal renormalization factors in a non-perturbative way

$$\langle \Theta_{12}(\tau,\vec{x})\Theta_{12}(0,\vec{0})\rangle = \frac{1}{4}\langle(\Theta_{11}-\Theta_{22})(\tau,\vec{x})(\Theta_{11}-\Theta_{22})(0,\vec{0})\rangle \tag{2.78}$$

$$\Leftrightarrow \left(Z^{rest}\right)^2 \langle \theta_{12}(\tau,\vec{x})\theta_{12}(0,\vec{0})\rangle = \frac{1}{4}\left(Z^{diag}\right)^2 \langle(\theta_{11}-\theta_{22})(\tau,\vec{x})(\theta_{11}-\theta_{22})(0,\vec{0})\rangle. \tag{2.79}$$

To summarize: This prescription allows to determine all renormalization factors of the isotropic and anisotropic energy momentum tensor up to a single overall renormalization factor. This last factor can for example be taken from measurements of the entropy density in [17].

2.2.2 Equation of State

Calculating the equation of state in lattice QCD is an important task, as its results directly concern cosmological studies of the early universe and present heavy-ion collision experiments. Its calculation in full QCD made big progress in the last years with fully controlled continuum extrapolated results at physical quark masses being available for $2+1$ flavours [18] and even first results for $2+1+1$ flavours [22]. For the pure SU(3) Yang-Mills theory there are very precise results available [17].

The equation of state connects the thermodynamic pressure P with the energy density ϵ. For an ideal relativistic gas it reads

$$\epsilon = 3P. \tag{2.80}$$

From this follows that the trace of the energy momentum tensor vanishes

$$T^{\mu}_{\mu} = T^{00} - 3T^{ii} = \epsilon - 3P = 0. \tag{2.81}$$

Any deviation from this behaviour indicates a deviation from the ideal non-interacting gas. The trace of the energy momentum tensor is therefore also called interaction measure

$$I = T^{\mu}_{\mu} = \epsilon - 3P. \tag{2.82}$$

A quark gluon plasma is strongly interacting for temperatures which are of the order of the transition temperature T_c and therefore has $I \neq 0$. This is also connected to the breaking of conformal symmetry, as if the theory were conformal,

there would not be a trace anomaly and $I = 0$. As it is strongly interacting, perturbative techniques cannot be used to calculate the equation of state and the lattice field theory toolset comes in again.

To calculate the trace anomaly on the lattice, one needs to renormalize the trace of the energy momentum tensor properly. In section 2.2.1 only the non-perturbative relative renormalization of the traceless parts was discussed. The renormalised value of the trace can be obtained by measuring the action density s_g and the non-perturbative β function [17, 38]

$$\frac{I}{T^4} = n_t^4 a \frac{\mathrm{d}\beta}{\mathrm{d}a} \left(\langle s_g \rangle_{n_s^3 \times n_t} - \langle s_g \rangle_{n_s^3 \times n_t^{sub}} \right), \tag{2.83}$$

with n_t and n_s the lattice sizes in lattice units in temporal and spatial direction. The subtraction is done to cancel divergences in the cutoff with the measurement on a lower temperature lattice sufficiently below the phase transition where the hadron/glueball resonance gas model works well.

To complete the non-perturbative renormalization of the energy momentum tensor of the last section 2.2.1, one still needs to get the renormalized value for the diagonal entries of the energy momentum tensor. This can be done by integrating a thermodynamics relation to get the pressure

$$\frac{P(T)}{T^4} - \frac{P(T_0)}{T_0^4} = \int_{T_0}^{T} \frac{I(T')}{T'^4} \mathrm{d}T'. \tag{2.84}$$

The constant of integration can be fixed by again comparing to the hadron/glueball resonance gas model.

Having a precise determination of the equation of state at hand, like [17], one can also adapt the strategy from section 2.2.1 to renormalize also correlators containing the trace of the energy momentum tensor. To account for the additive renormalization, one has to consider differences of the trace at different temperatures but the same coupling like in Equ. (2.83)

$$\begin{aligned} I_T - I_{T'} =& \langle T_\mu^\mu \rangle_T - \langle T_\mu^\mu \rangle_{T'} \\ =& Z_{tr} \left(\langle \theta \rangle_T - \langle \theta \rangle_{T'} \right), \end{aligned} \tag{2.85}$$

where Z^{tr} is the renormalization factor for the trace, θ is a lattice discretization of the trace, and $\langle . \rangle_T$ is the expectation value at the temperature T. Connected correlators are then built like

$$\langle T(\tau, \vec{x}) T(0, \vec{0}) \rangle = Z_{tr}^2 \left(\langle \theta(\tau, \vec{x}) \theta(0, \vec{0}) \rangle - \langle \theta(\tau, \vec{x}) \rangle \langle \theta(0, \vec{0}) \rangle \right). \tag{2.86}$$

2.2.3 Hydrodynamics

After the introduction of the energy momentum tensor in section 2.2.1, this section contains relations from relativistic hydrodynamics to cover the connection between the energy momentum tensor and the transport properties in an quark gluon plasma. The presentation here follows the references [15, 73, 74, 82] and uses co- and contravariant notation with Minkovski signature to be able to formulate dynamics.

Relativistic hydrodynamics is a covariant description of the properties of the energy momentum tensor of a dynamic medium, which is locally close to thermodynamic equilibrium. It is an effective description of the long wavelength properties and systematically structured as an expansion in gradients of the local constituting parameters of the medium. These parameters are the energy density ϵ, the pressure P, the flow 4-velocity u^μ, which is connected to the momentum density $\mathcal{P}^\mu$ via $\mathcal{P}^\mu = \epsilon u^\mu$ with $g_{\mu\nu}u^\mu u^\nu = -1$, and in theories with conserved charges also their currents J^μ. In QCD for example there is a conserved current for every quark flavour. In quenched QCD or pure Yang-Mills theory there are no conserved currents apart from the momentum density.

The microscopic description of the medium usually defines a relation between the pressure P and the energy density ϵ via the equation of state $P = P(\epsilon)$ which was introduced in section 2.2.2. Then there are four independent parameters left, which are fixed using the conservation of the energy momentum tensor $\nabla_\mu T^{\mu\nu} = 0$. This completely determines the fluid dynamics.

In lowest (zeroth) order in the gradient expansion

$$T^{\mu\nu} = \sum_{n=0}^{\infty} T_n^{\mu\nu}, \tag{2.87}$$

the energy momentum tensor can be written as

$$T_0^{\mu\nu} = \epsilon u^\mu u^\nu + P\Delta^{\mu\nu}, \tag{2.88}$$

where $\Delta := g^{\mu\nu} + u^\mu u^\nu$ acts as projection operator on the spatial directions of the local co-moving frame.

The first transport coefficients show up at first order in the gradients. To this order there are two new independent terms which are compatible with the symmetry of $T_{\mu\nu}$

$$T_1^{\mu\nu} = -\eta\sigma^{\mu\nu} - \zeta\Delta^{\mu\nu}\nabla_\alpha u^\alpha, \tag{2.89}$$

$$\sigma^{\mu\nu} := \Delta^{\mu\alpha}\Delta^{\nu\beta}\left(\nabla_\alpha u_\beta + \nabla_\beta u_\alpha - \frac{2}{3}\Delta_{\alpha\beta}\nabla_\gamma u^\gamma\right). \tag{2.90}$$

The term $\sigma^{\mu\nu}$ is also called the shear tensor. These terms come with two new coefficients, the shear viscosity η and the bulk viscosity ζ, which are the first transport coefficients. Stopping at first order in relativistic hydrodynamics introduces conceptual complications: The resulting equations allow for propagation of signals faster than light which violates causality. By including second order terms one can get rid of this problem.

The next order with two gradients per term gives rise to 15 possible new terms. To be able to write them in a rather compact way some new notation is introduced.

$$\Omega^{\mu\nu} := \frac{1}{2}\Delta^{\mu\alpha}\Delta^{\nu\beta}\left(\nabla_\alpha u_\beta - \nabla_\beta u_\alpha\right) \tag{2.91}$$

is called the vorticity tensor. The most general case also contains terms which are only relevant for curved space-time. For these one needs the Riemann curvature tensor $R^{\mu\nu\alpha\beta}$, the Ricci tensor $R^{\mu\nu} = R^{\mu}{}_{\alpha}{}^{\nu\alpha}$ and the Ricci scalar $R = R^{\mu}_{\mu}$. Also a notation is introduced for pairs of indices which are space-projected, symmetrized, and trace-subtracted. For the curvature tensor this notation looks like

$$R^{\mu\langle\nu\alpha\rangle\beta} := \frac{1}{2}R^{\mu\kappa\sigma\beta}\left(\Delta^{\nu}_{\kappa}\Delta^{\alpha}_{\sigma} + \Delta^{\nu}_{\sigma}\Delta^{\alpha}_{\kappa} - \frac{2}{3}\Delta^{\nu\alpha}\Delta_{\kappa\sigma}\right). \tag{2.92}$$

In this notation the second order terms are given as

$$\begin{aligned}
T_2^{\mu\nu} =& \eta\tau_\pi\left(u\cdot\nabla\sigma^{\mu\nu} + \frac{\nabla\cdot u}{3}\sigma^{\mu\nu}\right) + \eta\tau_\pi^*\frac{\nabla\cdot u}{3}\sigma^{\mu\nu} \\
&+ \kappa\left(R^{\langle\mu\nu\rangle} - 2u_\alpha u_\beta R^{\alpha\langle\mu\nu\rangle\beta}\right) + 2\kappa^* u_\alpha u_\beta R^{\alpha\langle\mu\nu\rangle\beta} \\
&+ \lambda_1\sigma_\lambda{}^{\langle\mu}\sigma^{\nu\rangle\lambda} + \lambda_2\sigma_\lambda{}^{\langle\mu}\Omega^{\nu\rangle\lambda} - \lambda_3\Omega_\lambda{}^{\langle\mu}\Omega^{\nu\rangle\lambda} + \lambda_4\nabla^{\langle\mu}\ln s\nabla^{\nu\rangle}\ln s \\
&+ \Delta^{\mu\nu}\left(-\zeta\tau_\Pi u\cdot\nabla\nabla\cdot u + \xi_1\sigma^{\alpha\beta}\sigma_{\alpha\beta} + \xi_2(\nabla\cdot u)^2\right) \\
&+ \Delta^{\mu\nu}\left(\xi_3\Omega^{\alpha\beta}\Omega_{\alpha\beta} + \xi_4\nabla_{\alpha\perp}\ln s\nabla^{\alpha}_{\perp}\ln s + \xi_5 R + \xi_6 u^\alpha u^\beta R_{\alpha\beta}\right).
\end{aligned} \tag{2.93}$$

In this expression there are also 15 new coefficients which are – for obvious reasons – called second order transport coefficients. Together with some properties and the first order coefficients they are listed in Tab. 2.2. These properties classify the coefficients in different categories, e.g. whether they are only relevant for curved space-time or whether they affect small fluctuations about equilibrium and flat space linearly.[11]

The most important property of a coefficient for studies in Euclidean space-time is whether it is a dynamical or a thermodynamical one. A term is thermodynamical if it can give a contribution to the energy momentum tensor $T^{\mu\nu}$ in equilibrated

[11] Also coefficients which influence $T^{\mu\nu}$ only in curved space-time like κ are still relevant, because they mix in the Kubo relations with other transport coefficients, compare reference [74].

coefficient	order	type	linearity	geometry
η	1.	dynamical	linear	flat
ζ	1.	dynamical	linear	flat
τ_π	2.	dynamical	linear	flat
τ_π^*	2.	dynamical	nonlinear	flat
κ	2.	thermodynamical	linear	curved
κ^*	2.	thermodynamical	linear	curved
λ_1	2.	dynamical	nonlinear	flat
λ_2	2.	dynamical	nonlinear	flat
λ_3	2.	thermodynamical	nonlinear	flat
λ_4	2.	thermodynamical	nonlinear	flat
τ_Π	2.	dynamical	linear	flat
ξ_1	2.	dynamical	nonlinear	flat
ξ_2	2.	dynamical	nonlinear	flat
ξ_3	2.	thermodynamical	nonlinear	flat
ξ_4	2.	thermodynamical	nonlinear	flat
ξ_5	2.	thermodynamical	linear	curved
ξ_6	2.	thermodynamical	linear	curved

Table 2.2: First and second order transport coefficients from relativistic hydrodynamics.

systems. In the general context equilibrium means a time independent density matrix and a time independent geometry. All other terms are of dynamical nature. An important consequence of a coefficient being thermodynamical is that it can be calculated using only retarded correlators at vanishing Minkovski frequency. They are up to powers of i identical to Euclidean frequency correlators at vanishing Euclidean frequency and can therefore be in principle straightforwardly evaluated in an Euclidean lattice simulation. In contrast, the dynamical coefficients require an evaluation of the retarded correlator at non-vanishing Minkovski frequency, i.e. they require analytic continuation of the Euclidean lattice results which is an intrinsically difficult task.

2.2.4 Kubo Relations

Section 2.2.3 introduced the transport coefficients as effective parametrization of macroscopic properties of any microscopic theory, which is slightly out of equilibrium. This section deals with possible ways to calculate these coefficients from measurements in simulations performed with Euclidean metric. This section will only reproduce results and details as far as they are relevant for the understanding of the thesis. For derivations and further details, the references [12, 15, 73, 74, 82, 89] may be considered.

Transport coefficients can be divided into two groups, dynamical and thermodynamical ones. Dynamical transport coefficients require analytical continuation

to Minkovski time, i.e. reconstructing the spectral function from an Euclidean two point correlation function. This is inherently a difficult task to perform on the lattice. This point will be made more explicit in later paragraphs of this section and a standard strategy to solve these problems is discussed in section 3.3.

The second group, the thermodynamical transport coefficients, are in principle easier accessible for Euclidean lattice QCD simulations, because they do not need analytic continuation of the Euclidean results and can be calculated directly from Euclidean observables.

Dynamical Transport Coefficients

The observables which can be measured in lattice QCD are Euclidean correlators. Two point correlation functions for example are defined as

$$C_{\mu\nu,\rho\sigma}(\tau,\vec{q}) = T^{-5}\int \mathrm{d}^3\vec{x}e^{i\vec{q}\cdot\vec{x}}\left(\langle\Theta_{\mu\nu}(x)\Theta_{\rho\sigma}(0)\rangle - \langle\Theta_{\mu\nu}(x)\rangle\langle\Theta_{\rho\sigma}(0)\rangle\right), \tag{2.94}$$

where a suitable power of the temperature T is introduced to make the correlator dimensionless. Any trivial constant contribution to the correlator is subtracted giving the connected part of the total correlator. These correlators are connected to their spectral functions $\rho_{\mu\nu,\rho\sigma}(\tau,\vec{q})$ via the integral transformation Equ. (2.39), which is reproduced here in slightly more convenient notation

$$C_{\mu\nu,\rho\sigma}(\tau,\vec{q}) = \int_0^\infty \mathrm{d}\omega K(\tau,\omega)\rho_{\mu\nu,\rho\sigma}(\omega,\vec{q}) \tag{2.95}$$

$$K(\tau,\omega) = \frac{\cosh(\omega(\tau-1/(2T)))}{\sinh(\omega/(2T))}, \tag{2.96}$$

with the finite temperature kernel $K(\tau,\omega)$.

Transport properties are low energy or long wavelength properties of the theory and are therefore encoded in the low energy properties of the spectral functions. For the two channels which are relevant for the viscosity the important relations are [69, 89]

$$\pi\lim_{\omega\to0}\lim_{q\to0}\frac{\rho_{13,13}(\omega,q)}{\omega} = \eta \tag{2.97}$$

$$\pi\lim_{\omega\to0}\lim_{q\to0}\frac{\rho_{33,33}(\omega,q)}{\omega} = \frac{4}{3}\eta+\zeta, \tag{2.98}$$

with the bulk viscosity ζ and the momentum taken parallel to the 3-direction $\vec{q} = q\vec{e}_3$. At the temperatures relevant for phenomenology, the bulk viscosity ζ is expected to be much smaller than the shear viscosity η. Therefore it is also possible to determine the shear viscosity η from $\rho_{33,33}$.

Finite Temperature Kernel

To get the dynamic transport properties from the Euclidean correlator, the most straightforward strategy is to first measure the Euclidean correlator from Equ. (2.94), then to invert the integral transformation Equ. (2.95) somehow, and finally to take the limit of the spectral function for vanishing energy to obtain the transport coefficient following Equs. (2.97) and (2.98). However, there exist, not surprisingly, several problems in this approach.

A quite obvious problem is directly related to the integral transformation Equ. (2.95). The Euclidean correlator can be measured only at a very limited number of points in Euclidean time. From that one wants to reconstruct a "continuous" spectral function to get a well defined zero frequency limit from. So the problem of solving Equ. (2.95) for ρ is ill posed in the first place. There are several ansätze to deal with that problem, e.g. the Maximum Entropy Method (MEM) [4, 9], presented in section 3.3. However, this method has always had problems resolving not only the integrated spectral weight of the spectral function in an extended region in ω but also to get the value of the spectral function at a single point of ω – in this case for $\omega = 0$.

In this thesis an ansatz for the spectral function will be used and the data will be fitted by the numerically evaluated integral. An ansatz provides a continuous spectral function and has no problems with an underdetermined system of equations as long as the number of parameters of the ansatz is smaller than the number of points at which the Euclidean correlator is measured.

A second problem is that the kernel is basically a cosh kernel which gives exponentially small weight to contributions of low frequency in the Euclidean correlator. This makes it hard to measure the correlator precisely enough to have a signal not only for the higher energy contributions, but also for the low energy end of the spectrum. Additionally, this exponentially strong background weight from high energies has to be disentangled from the transport signal in the analysis. Moreover, the decay of excited contributions in Euclidean time is not as useful as one might expect it to be: The decay is only cosh-like so that contributions at all energies give a contribution to the correlator also at maximum distance in Euclidean time, i.e. in the middle of the correlator at $\tau = 1/(2T)$. For the current application this problem is additionally aggravated by the dimension of the spectral function which enhances high energy contributions by an additional factor of ω^4 for large energies. The effect of the finite high energy contribution in the middle of the correlator can be demonstrated by comparison with the analytically

known tree-level expectation values [67]

$$\rho^{t.l.}_{1313}(\omega,\vec{0}) = \frac{1}{10}\frac{d_A}{(4\pi)^2}\frac{\omega^4}{\tanh(\omega/4T)} + \left(\frac{2\pi}{15}\right)^2 d_A T^4 \omega\delta(\omega) \tag{2.99}$$

$$C^{t.l.}_{1313}(\tau,\vec{0}) = \frac{32 d_A}{5\pi^2}\left(\int_0^\infty \mathrm{d}s s^4 \frac{\cosh^2((1-2T\tau)s)}{\sinh^2(s)} - \frac{\pi^4}{72}\right). \tag{2.100}$$

In this case $C^{t.l.}_{1313}(1/2T,\vec{0}) = (28\pi^2 d_A)/225$, while the part corresponding to transport yields only $(4\pi^2 dA)/225$ which is only 1/7 of the total value for maximum Euclidean time separation. A strategy how to remedy this problem is given in section 3.4.2.

Another problem directly connected to the kernel is that it is in leading order insensitive to the low frequency behaviour, i.e. to transport [3]. Expanding the kernel in powers of ω yields

$$K(\tau,\omega) = \frac{2T}{\omega} + \left(\frac{1}{6T} - \tau + T\tau^2\right)\omega + \mathcal{O}(\omega^3). \tag{2.101}$$

The divergence for small frequencies is just a technical problem which can be overcome because the spectral function itself is linear in ω for small ω (compare e.g. Equs. (2.97), (2.98)). This shows that the leading low frequency contribution is a term which does not depend on the Euclidean time τ and provides only one real number as information. To get a value for the transport coefficient, one should be able to resolve the transport peak, i.e. both the width and the height of a contribution to the spectral function at low omega. One can expect that the leading order effect of the transport peak in the correlator scales with the spectral weight, i.e. the area of the peak, which would then be the information contained in the constant part. More information from a term of next to leading order in the kernel is needed to determine the transport coefficient but this is suppressed by two powers of ω. This is not a problem if the transport peak is very broad. For the high energy limit, however, the transport peak becomes a δ-like contribution, which might render the hope for a very broad peak optimistic. The alternative is to maximize sensitivity to the low energy part of the spectrum, which is the reason to include data with small finite momentum.

Thermodynamical Transport Coefficients

From Euclidean correlators like those in Equ. (2.94) one can also construct relations for thermodynamical transport coefficients. But in contrast to the dynamical coefficients no reconstruction of a spectral function is necessary. Instead the corresponding Kubo relations involve simply the Euclidean correlators themselves.

Like the dynamical transport coefficients the thermodynamical transport co-

efficients are low energy or long wavelength properties. But this is achieved by considering the limit of low spatial momenta instead of the limit of small Minkovski time frequencies. For the two second order thermodynamical transport coefficients considered in this thesis, κ and λ_3, these relations read [74]

$$\kappa = \lim_{q_3 \to 0} \frac{\partial^2}{\partial q_3^2} C_{12,12}(\vec{q}), \tag{2.102}$$

$$\lambda_3 = -4 \lim_{p_3, q_3 \to 0} \frac{\partial^2}{\partial p_3 \partial q_3} C_{\lambda_3}(\vec{p}, \vec{q}) \tag{2.103}$$

where

$$C_{\mu\nu,\rho\sigma}(\vec{q}) = T \int d\tau C_{\mu\nu,\rho\sigma}(\tau, \vec{q}) \tag{2.104}$$

and a correlator $C_{\lambda_3}(\vec{p}, \vec{q})$ containing a three point correlation function is introduced

$$C_{\lambda_3}(\vec{p}, \vec{q}) = C_{\lambda_3,2}(\vec{p} + \vec{q}) + C_{\lambda_3,3}(\vec{p}, \vec{q}) \tag{2.105}$$

$$C_{\lambda_3,2}(\vec{q}) = T^{-4} \int \mathrm{d}^4\vec{x} e^{i\vec{q}\cdot\vec{x}} \langle X_{x0y0}(x) \Theta_{12}(0) \rangle \tag{2.106}$$

$$C_{\lambda_3,3}(\vec{p}, \vec{q}) = T^{-4} V_4 \int \mathrm{d}^4\vec{x} \int \mathrm{d}^4\vec{y} e^{i\vec{q}\cdot\vec{x}} e^{i\vec{p}\cdot\vec{y}} \langle \Theta_{10}(x) \Theta_{20}(y) \Theta_{12}(0) \rangle. \tag{2.107}$$

The observable X_{x0y0} used in Equ. (2.106) originates from a contact term and reads

$$X_{x0y0} = -F_{xz} F_{yz} \tag{2.108}$$

where $x, y, z \in \{1, 2, 3\}, x \neq z \neq y$. It is a part of the xy component of the energy momentum tensor Θ and therefore renormalizes accordingly.

2.3 Wilson Flow

A particularly interesting and promising concept in lattice QCD is the Wilson flow [58]. It can be used as a tool for understanding topological properties of the gauge fields, as an alternative method to set the scale in lattice calculations, and as an alternative to determine the gauge anisotropy [19, 20].

2.3.1 Definition

The Wilson flow was introduced in reference [61] in the context of trivializing maps of field space. A trivializing map is a map $\mathcal{F}$ such that

$$\mathcal{F} : V \in SU(3) \to SU(3) \ni U \tag{2.109}$$

$$\langle O \rangle = \frac{1}{\mathcal{Z}} \int \mathrm{D}[U] O(U) e^{-S(U)} \to \langle O \rangle = \frac{1}{\mathcal{Z}} \int \mathrm{D}[V] O(\mathcal{F}(V)). \tag{2.110}$$

The path integral of a field theory becomes trivial, if such a map $\mathcal{F}$ can be found. This map then contains all the dynamics of the theory, Monte-Carlo sampling procedures become trivial, and therefore there are in particular no problems with the critical slowing down due to emergence of topological sectors.

In reference [61] such a map was explicitly constructed for pure gauge theories as result of a flow in field space

$$\frac{\mathrm{d}}{\mathrm{d}t} V_t = Z_t(V_t) V_t \tag{2.111}$$

$$V_0 = U \tag{2.112}$$

$$\mathcal{F}^{-1}(U) = V \tag{2.113}$$

$$= V_{t=1}. \tag{2.114}$$

The generator of this flow is given as a power series in the flow time

$$Z_t(U) = \sum_{n=0}^{\infty} t^n Z^{(n)}(U). \tag{2.115}$$

The first order in this series is given by the gradient of the action

$$Z^{(0)}(U) = -g_0^2 \left\{ \partial_{x,\mu} S(U) \right\}. \tag{2.116}$$

This flow truncated at the first order is called Wilson flow or for obvious reasons also gradient flow.

For the Wilson gauge action one gets an explicit form for the first order generator

$$\begin{aligned} Z^{(0)}(U)(x,\mu) = &- \sum_{\nu \neq \mu} \mathcal{P} \Big\{ U(x,\mu) U(x+\hat{\mu},\nu) U(x+\hat{\nu},\mu)^{-1} U(x,\nu)^{-1} \\ &+ U(x,\mu) U(x+\hat{\mu}-\hat{\nu},\nu)^{-1} U(x-\hat{\nu},\mu)^{-1} U(x-\hat{\nu},\nu) \Big\} \end{aligned} \tag{2.117}$$

$$\mathcal{P}\{M\} = \frac{1}{2}(M - M^\dagger) - \frac{1}{6}\mathrm{tr}(M - M^\dagger). \tag{2.118}$$

This gives exactly the generator of a stout smearing step of Equ. (2.17).

In continuum language the Wilson flow is equivalently defined with the flow

$B_\mu(t,x)$

$$\frac{\mathrm{d}}{\mathrm{d}t}B_\mu = D_\nu G_{\nu\mu} \tag{2.119}$$

$$B_\mu|_{t=0} = A_\mu, \tag{2.120}$$

where t denotes the flow time, G the Euclidean field strength tensor, and D the Euclidean covariant derivative:

$$G_{\mu\nu} = \partial_\mu B_\nu - \partial_\nu B_\mu + [B_\mu, B_\nu] \tag{2.121}$$

$$D_\mu = \partial_\mu + [B_\mu, .]. \tag{2.122}$$

From Equ. (2.119) one can also see that the inverse flow time has the unit energy squared.

2.3.2 Smearing Properties

As seen in the last section, the Wilson flow is well defined in the compact and non-compact formulation of a gauge theory. In the compact formulation it can be defined via the generator of a stout smearing step

$$\frac{\mathrm{d}}{\mathrm{d}t}V_\mu = \mathrm{i}Q_\mu V_\mu, \tag{2.123}$$

$$V_\mu|_{t=0} = U_\mu, \tag{2.124}$$

where V_μ is the flow of the lattice fields U_μ, t is the flow time, and Q_μ the generator of stout smearing steps with $\rho_{Stout} = 1$ from Equ. (2.17). On the lattice, Equ. (2.123) can be integrated up to any desired flow time numerically. As it is generated by stout smearing steps, it can also be integrated up approximately by applying a number of stout smearing steps with the resulting flow time being $8t = 8\rho_{Stout}N_{Stout}a^2 = r^2_{smear}$.

To make this smoothing operation on gauge configurations more explicit, one can consider the action of the flow on the gauge fields in leading order of perturbation theory in the bare coupling g_0 [58]

$$B_\mu(t,x)/g_0 = A^t_\mu(x) = \int \mathrm{d}^4 y K^t(x-y)A_\mu(y) + \mathcal{O}(g_0), \tag{2.125}$$

$$K^t(z) = \frac{e^{-z^2/4t}}{(4\pi t)^2}. \tag{2.126}$$

This shows the smoothing effect directly as Gaussian filter with a radius of $r_{smear} = \sqrt{8t}$.

As the gauge fields themselves are not gauge invariant quantities, they are no

observables. To see the effect of the smoothing operation on observables, one therefore has to construct gauge invariant combinations like scalars or correlators. While sections 2.3.3 and 2.3.4 below discuss some important applications of the effects on scalar observables, this section will concentrate on the effect on correlators.

The physical picture is as follows: The flow is a smearing operation which acts on a length scale $r_{smear} = \sqrt{8t}$. This affects the ultraviolet contributions to the correlator at distances $\tau \lesssim r_{smear}$ or $\omega \gtrsim \pi/r_{smear}$, e.g. by reducing the spectral weight in the spectral representation of the correlator. The infrared contributions to the correlator at distances $\tau \gg r_{smear}$ or $\omega \ll \pi/r_{smear}$ should be virtually unchanged, corresponding to an invariant spectral function in that regime. As the focus of this thesis is mainly on the infrared parts of spectral functions to obtain transport coefficients of the quark gluon plasma, it is enough that the infrared spectral function is invariant. The details of how the flow changes the short distance part of the correlator can also be worked out using perturbation theory. An analogous argument as for the frequency in the spectral function applies for the spatial momentum of observables. The effect of the flow should be strongest at large momenta and smear out these contributions.

In the remaining part of the section the effects of the flow on the correlator of the energy momentum tensor in leading order in perturbation theory are given. Details of the calculations using Equ. (2.125) are worked out in appendix A. The calculation uses translation invariance, partial integration, and builds the energy momentum tensor $\Theta^t_{\mu\nu}$ at flow time t directly from the gauge fields A^t_μ at flow time t.

For any local observables O_1 and O_2 which behave like

$$O^t(x) = \int \mathrm{d}^4 y K^t(x-y) O(y) \tag{2.127}$$

at finite flow time t, one can derive for their two point correlator the relation

$$C^t_{O_1,O_2}(\tau,\vec{p}) = e^{-2t\vec{p}^2} \int \mathrm{d}y_0' K_1^{2t}(\tau - y_0') C_{O_1,O_2}(y_0',\vec{p}) \tag{2.128}$$

$$K_1^t(\tau) = \frac{e^{-\tau^2/4t}}{\sqrt{4\pi\tau}}. \tag{2.129}$$

As the energy momentum tensor is built from a product of two fields at the same point which both are smeared out by the flow, the effective smearing radius is changed. The two point function is then given by

$$C^t_{\mu\nu,\rho\sigma}(\tau,\vec{p}) = e^{-t\vec{p}^2} \int \mathrm{d}x_0 K_1^t(\tau - x_0) C_{\mu\nu,\rho\sigma}(x_0,\vec{p}) + \mathcal{O}(g_0) + \mathcal{O}(t). \tag{2.130}$$

The correction $\mathcal{O}(t)$ comes from expanding the product.

Equ. (2.130) connects the correlation function at finite flow time with the one at zero flow time by convoluting it with a Gaussian in Euclidean time. Although this equation is only valid for small flow times t and leading order perturbation theory, i.e. at the highest energies, one can see directly the effect of the non-locality induced by the smearing of the flow. This will be visible as a strong deviation from the expected form of an Euclidean correlation function for short distances: Instead of a sharp peak at finite lattice spacing, which develops to the expected $1/\tau^5$ divergence in the continuum limit, one gets a smooth bump. This structure is independent of the lattice spacing when the lattice cutoff at π/a is at a higher energy than the cutoff induced by the Wilson flow smearing scale at π/r_{smear}.

Another correlation function, which is used in the thesis, is the three point function of the energy momentum tensor for finite momentum integrated over Euclidean time. At finite flow time and at leading order this results in

$$C^t_{\mu\nu,\rho\sigma,\kappa\eta}(p,q) = e^{-\frac{1}{2}(p^2+q^2+(p+q)^2)t} C_{\mu\nu,\rho\sigma,\kappa\eta}(p,q) + \mathcal{O}(g_0) + \mathcal{O}(t). \tag{2.131}$$

As the Gaussian kernels $K^t(\tau)$ are properly normalized to 1, the only factor remaining after integration over Euclidean time is the Gaussian suppression of finite Euclidean momenta. Again this result is only valid for small flow times and at first order in perturbation theory, which is not the regime of interest for transport studies.

2.3.3 Scale Setting

Using the perturbative relations given in section 2.3.1 one can derive the behaviour of scalar quantities like

$$E = \frac{1}{4} G^a_{\mu\nu} G^a_{\mu\nu}, \tag{2.132}$$

which is basically a definition of the gauge action. This quantity has dimension 4 and can be made dimensionless by multiplying it with a suitable power of the flow time, t^2E. This quantity was discussed in detail in reference [58] both for the lattice and perturbatively. There it is noted that it is possible to define a scale based on the fact that E at finite flow time is a physical renormalized quantity. This is done by requiring

$$t^2\langle E\rangle\Big|_{t=t_0} = 0.3 \tag{2.133}$$

for a scale t_0. The parameter 0.3 is chosen such that one is safely in a region of linear behaviour of $t^2\langle E\rangle$ with the flow time t and that it is readily available on the lattice in a region with negligible cutoff effects. However, this choice is in principle arbitrary.

In reference [19] a different but related scale was proposed which is defined by

$$t\frac{\mathrm{d}}{\mathrm{d}t}\{t^2\langle E\rangle\}\Big|_{t=w_0^2} = 0.3. \tag{2.134}$$

Compared to t_0 the scale w_0 has the advantage that it has by about a factor of 4 reduced cutoff effects. For the scale w_0 it was also shown that it is sufficient to consider the gradient flow defined by the gradient of the Wilson gauge action in contrast to considering the more expensive gradient of the improved Symanzik gauge action.

2.3.4 Anisotropy Tuning

In analogy to setting the scale in lattice QCD simulations in section 2.3.3, one can also use the Wilson flow to measure and tune the anisotropy of the lattice as shown in reference [20]. This is achieved by measuring the scale independently using observables built from the mixed spacial-temporal contribution to E

$$E_{st} = \sum_{\mu \text{ or } \nu \text{ temporal}} \frac{1}{4} G^a_{\mu\nu} G^a_{\mu\nu}, \tag{2.135}$$

and the one built from the purely spacial contribution

$$E_{ss} = \sum_{\mu \text{ and } \nu \text{ spacial}} \frac{1}{4} G^a_{\mu\nu} G^a_{\mu\nu}. \tag{2.136}$$

Because of the symmetry between spacial and temporal directions the expectation values $\langle E_{st}\rangle$ and $\langle E_{ss}\rangle$ of both observables should yield half the value of $\langle E\rangle$, as long as both are measured in the same units. That means that the ratio of both observables in lattice units measured at a fixed flow time in physical units is proportional to the squared renormalized gauge anisotropy ξ_g. The same is valid for the observables used to define the scale with the w_0 scale

$$R_E := t\frac{\mathrm{d}}{\mathrm{d}t}\{t^2\langle E_{ss}\rangle\}\Big|_{t=w_0^2} \Big/ t\frac{\mathrm{d}}{\mathrm{d}t}\{t^2\langle E_{st}\rangle\}\Big|_{t=w_0^2} \tag{2.137}$$

such that in the end

$$R_E = \xi_g^2. \tag{2.138}$$

The calculation of R_E requires the integration of the anisotropic Wilson flow which in turn requires the knowledge of ξ_g. Therefore Equ. (2.138) becomes a self consistency equation and one has to tune the bare anisotropy to fulfill this equation. To completely define this choice of discretized anisotropy, one also needs to redefine the scale w_0 in the anisotropic setting, which can easily be done by using the spacial part of Equ. (2.134)

$$t\frac{\mathrm{d}}{\mathrm{d}t}\{t^2\langle E_{ss}\rangle\}\Big|_{t=w_0^2} = 0.15. \tag{2.139}$$

2.3.5 Renormalization

The continuous Wilson flow as defined in Equ. (2.119) yields finite renormalized fields and products of fields at positive flow times as shown in reference [63]. Also all observables measured at finite flow time are finite renormalized quantities with improved discretization errors. This property can be used to investigate the renormalization structure of the energy-momentum tensor.

Additionally reference [63] showed that local products of gauge fields at positive flow time can be expanded in renormalized local operators at zero flow time. This was used by reference [87] to derive the perturbative structure of the coefficients appearing in the expansion and to relate them to the MS continuum renormalization scheme for small flow time.

In particular, for the trace density $E(t,x)$ and the density of the traceless part $Y(t,x)$ of the energy-momentum tensor at finite flow time, one finds the expansions

$$Y_{\mu\nu}(t,x) = \alpha_Y(t)\left[T_{\mu\nu}(x) - \frac{\delta_{\mu\nu}}{4}T_{\sigma\sigma}(x)\right] + \mathcal{O}(t) \tag{2.140}$$

$$E(t,x) = \langle E(t,x)\rangle + \alpha_E(t)T_{\mu\mu}(x) + \mathcal{O}(t) \tag{2.141}$$

with the full renormalized energy-momentum tensor densities at vanishing flow time T. The $\mathcal{O}(t)$ corrections in the operator product expansion absorb contributions of operators of dimension 6 and higher which are accompanied by a factor of at least t^1. The factors α_E and α_Y can be given in a perturbative expansion [87].

More interesting in the context of lattice QCD are non-perturbative strategies like the one proposed in reference [31]. One can introduce a probe observable ϕ_τ at fixed positive flow time τ and define an effective coefficient $\alpha_E^{eff}(t)$ by

$$\left\langle \phi_{t_0} \int \mathrm{d}^4x[E(t,x) - \langle E(t,x)\rangle]\right\rangle =: \alpha_E^{eff}(t)\left\langle \phi_\tau \int \mathrm{d}^4x T_{\mu\mu}(x)\right\rangle. \tag{2.142}$$

By construction $\alpha_E^{eff}(t) = \alpha_E(t) + \mathcal{O}(t)$. This way one can construct an expression

for a properly renormalized trace of the energy-momentum tensor

$$T_{\mu\mu}(x) = \frac{1}{\alpha_E^{eff}(t)}[E(t,x) - \langle E(t,x)\rangle] + \mathcal{O}(t). \tag{2.143}$$

By using a dilatation Ward identity one gets from Equ. (2.142)

$$\left\langle \phi_{t_0} \int \mathrm{d}^4x [E(t,x) - \langle E(t,x)\rangle] \right\rangle = \alpha_E^{eff}(t) \left(2\tau \frac{\mathrm{d}}{\mathrm{d}\tau} + d_\phi \right) \langle \phi_\tau \rangle \tag{2.144}$$

with the dimension d_ϕ of the probe observable. To make things more explicit one can choose

$$\tau = w_0^2 \tag{2.145}$$

$$\phi_\tau = E(w_0^2) = \frac{1}{V_4} \int \mathrm{d}^4x E(w_0^2, x). \tag{2.146}$$

With the definition of the scale w_0 in Equ. (2.134) one gets

$$\left(2\tau \frac{\mathrm{d}}{\mathrm{d}\tau} + d_\phi \right) \langle \phi_\tau \rangle = \frac{2}{w_0^4} 0.3 \tag{2.147}$$

and therefore

$$\alpha_E^{eff}(t) = \frac{w_0^4}{0.6} V_4 \left\langle E(w_0^2)(E(t) - \langle E(t)\rangle) \right\rangle. \tag{2.148}$$

This gives a powerful tool for renormalization of the trace of the energy-momentum tensor. In principle, the same is possible for the coefficient α_Y but the expressions become quite unhandy and will not be covered here [31]. Instead, for the renormalization of the traceless part of the energy-momentum tensor the non-perturbative stategy outlined in section 2.2.1 will be used.

2.4 AdS/CFT Correspondence

This section will discuss an approach that is in many ways orthogonal to what is discussed in all other sections of the current chapter 2: It will discuss an aspect of the relation of some 4 dimensional quantum field theories with some 5 dimensional theories of classical gravitation, called holography. It will first introduce the topic along the lines of Maldacenas conjecture on gauge/gravity duality. Then it will introduce a specific model that is tailored to describe the gauge part of QCD, called Improved Holographic QCD.

2.4.1 Maldacenas Conjecture

String theory was originally introduced to describe the spectrum of hadronic states as excitations of fundamental relativistic strings [7]. After initial success in describing the Regge trajectories in the hadronic spectrum, the theory had problems in matching other predictions to experiment. In particular, every string theory contains a massless spin 2 mode which is not found in the hadron spectrum. After that and the successful description of hadrons with QCD, the focus in string theory shifted towards providing a candidate theory for quantum gravity, as the graviton, a massless spin 2 mode, is an important ingredient for a quantum theory of gravity. To use string theory as a fundamental theory of everything poses several problems, e.g. the problem of immensely degenerate string vacua which are a result from different compactifications of 6 of the 10 dimensions of string theory to arrive at an effectively 4 dimensional description of the world [36, 54].

The next application of string theory is by far the most useful one for everyday physics. It was conjectured that a type IIB string theory on $AdS_5 \times S^5$ is dual to $\mathcal{N} = 4$ $U(N_c)$ Super Yang-Mills theory in $3 + 1$ dimensions [65]. In this duality the effective coupling on the QFT side is given by the 't Hooft coupling $\lambda = N_c g_{YM}^2$, while the coupling on the string side is $1/N_c$. In particular this enables derivations of properties of a strongly coupled four dimensional quantum field theory by calculating properties of a weakly coupled string theory instead. If the coupling is very weak on the string side corresponding to $N_c \to \infty$, one can even use classical gravity to describe the theory, because the quantum corrections are suppressed as $1/N_c$. More details can been found e.g. in reference [7].

This is an interesting calculational tool for the conformal maximally supersymmetric $U(N_c \to \infty)$ Yang-Mills theory. Other dualities connecting quantum field theories and string theories have also been found, but none of these theories is realized in nature. It is expected, however, that some string theories have duals which approximate QCD in many properties. Therefore it was tried to construct effective string theory or gravity models that have a dual theory which comes close to QCD. One of them is shortly introduced in the next section 2.4.2.

There have also been results which are quite general and do not depend much on the details of the underlying string theory. For example, the duality was used to show that the shear viscosity over entropy density ratio η/s is very small with a value of $1/4\pi$. This is valid for a large class of strongly interacting quantum field theories, namely those which have a dual gravity description. It was conjectured that this is the universal absolute lower bound for any fluid [56].

2.4.2 Improved Holographic QCD

In contrast to the duality described in the last section 2.4.1, the model introduced here directly aims at producing relevant results for QCD phenomenology, in particular that of heavy ion collisions. This model, Improved Holographic QCD (IHQCD), was introduced to describe the results of $SU(N_c)$ Yang-Mills theory [47, 48] with possible extensions to (massless) quarks. Direct comparisons to published results of lattice QCD for zero and finite temperature were used to fix some of the phenomenologically relevant model parameters [46, 49]. The model is then consistent with a range of additional lattice observations like glueball masses at zero temperature and the equation of state from thermodynamics. But the available and published lattice observables are not enough to completely determine all of the parameters such that additional lattice calculations are necessary.

Improved Holographic QCD is defined as a theory of 5 dimensional classical gravitation. It is given by the bulk action

$$S = M^3 N_c^2 \int \mathrm{d}^5x\sqrt{-g}\left(R - \frac{4}{3}\frac{(\partial\lambda)^2}{\lambda^2} - \frac{Z(\lambda)}{2N_c^2}(\partial a)^2 + V(\lambda)\right), \tag{2.149}$$

where M is the 5D Planck mass, N_c is the number of colors, g is the determinant of the 5D metric, R is the 5D Ricci scalar, $\lambda \sim e^{\phi}$ with a dilaton field ϕ, and a is an axion field. The functions $Z(\lambda)$ and $V(\lambda)$ are functions which have their small and large λ limits fixed by consistency considerations.

The connection to the 4 dimensional Yang-Mills theory, which lives on the boundary of the AdS space at $r = 0$, is given by a holographic dictionary relating 5D bulk quantities with 4D QFT quantities. The axion term in the action is suppressed by $1/N_c^2$ and is not important in the large N_c limit. Therefore the back-reaction of the axions on the metric is not important for determining a background solution for the metric. Fluctuations of the fields on the background can then be related to states of the QFT. In the holographic dictionary the graviton is dual to the Yang-Mills energy momentum tensor $tr(F_{\mu\nu}^2 - 1/4\delta_{\mu\nu}F^2)$, the dilaton ϕ to $tr(F^2)$, the axion field a is dual to the topological charge density $tr(F \wedge F)$, and λ is dual to the running 't Hooft coupling $N_c g_{YM}^2$. It is expected that 4D Yang-Mills theory is dual to a string theory in 5D with all quantum corrections. As IHQCD describes a classical theory of gravity without quantum corrections, it is most reliable in the infrared at low energies and large distances.

The equations of motion arising from the action Equ. (2.149) have for a constant dilaton potential $V(\lambda) = 12/l^2$ with some length scale l an AdS solution

$$\mathrm{d}s^2 = \frac{l^2}{r^2}(\mathrm{d}r^2 - \mathrm{d}t^2 + \mathrm{d}\vec{x}^2), \tag{2.150}$$

with the radial AdS coordinate $0 < r < \infty$ dual to the energy scale of the QFT: $r \to 0$ corresponds to the ultraviolet regime whereas $r \to \infty$ corresponds to the infrared regime. For non-trivial potential the metric is modified by the warp factor $b(r)$

$$\mathrm{d}s^2 = b(r)(\mathrm{d}r^2 - \mathrm{d}t^2 + \mathrm{d}\vec{x}^2), \tag{2.151}$$

and the equations of motion must be solved numerically.

IHQCD introduces parametrizations for the functions $V(\lambda)$ and $Z(\lambda)$ consistent with the mentioned limiting cases

$$V(\lambda) = \frac{12}{l^2}\left(1 + V_0\lambda + V_1\lambda^{4/3}\sqrt{\log(1 + V_2\lambda^{4/3} + V_3\lambda^2)}\right) \tag{2.152}$$

$$Z(\lambda) = Z_0(1 + c_1\lambda^1 + c_2\lambda^2 + c_3\lambda^3 + c_4\lambda^4), \tag{2.153}$$

with the parameters V_i and c_i. V_0 and V_2 can be expressed in terms of V_1 and V_3 by relating the dilaton potential to the QCD β function. The corrections due to c_2 and c_3 are subleading and they can therefore be set to 0. These parameters (and a few others like the length scale l) have to be constrained by lattice data. Up to now lattice thermodynamics data and lattice glueball masses have been used for that. Unfortunately the glueball masses are not very sensitive to some combinations of the parameters, such that there are still degeneracies in the parameter space. For example, the masses of the pseudoscalar glueballs go like the asymptotic $m_n^{0^{+-}} \sim n$ behaviour after the first few states, such that from the axial sector just one combination of c_1 and c_4 can be fixed.

Chapter 3

Methods

The current chapter describes a collection of approaches used to extract physical results from lattice QCD simulations. Thereby it naturally connects chapter 2 on physical concepts with chapter 4, which contains the results of the numerical simulations done within this work. Some of the methods presented here were mostly used in early stages of the work for this thesis to answer questions corresponding to the reconstruction of spectral properties of quarkonia at finite temperature. The focus of the corresponding sections 3.1, 3.2, and 3.3 is to present these methods and some advancements of their applicability, accuracy, and generality which were achieved during the work for this thesis. Additionally, they constitute a presentation of the leading alternatives to the methods of sections 3.4 and 3.5 which were mainly used for the analyses in the chapter on numerical results. This chapter ends with a presentation of the statistical methods applied for the analysis of lattice data in this thesis.

3.1 Effective Mass

All methods in this chapter discuss approaches allowing to extract spectral information from measurements performed on Euclidean space-time lattices. Spectral information in this context means information on the spectral representation

$$C(\tau) = \sum_n A_n K(\tau, E_n) \tag{3.1}$$

or its continuous counterpart equation

$$C(\tau) = \int_0^\infty \mathrm{d}\omega A(\omega) K(\tau, \omega), \tag{3.2}$$

where the kernel K reflects the geometry of the lattice and symmetry of the operators. For zero temperature (i.e. infinite lattice extents) $K(\tau, \omega) = e^{-\omega\tau}$ (like in Equ. (2.4)). For finite temperature and bosonic operators $K(\tau, \omega) =$

$\cosh\left(\left(\frac{\beta}{2}-\tau\right)\omega\right)/\sinh\left(\frac{\beta}{2}\omega\right)$ like in Equ. (2.39) while for fermionic operators $K(\tau,\omega)=\sinh\left(\left(\frac{\beta}{2}-\tau\right)\omega\right)/\sinh\left(\frac{\beta}{2}\omega\right)$.

3.1.1 General

The first method discussed here usually assumes the validity of the discrete spectral sum of Equ. (3.1) in the region of low energies. More specifically, it assumes that the state corresponding to the lowest energy state describes a stable particle and that there is a finite gap to the next more energetic state. In the language of the continuous version Equ. (3.2) this implies the existence of a delta function like contribution in the spectral function at some finite low frequency with the remaining spectral weight distributed at some finite separation from this ground state peak.

If one takes any one of the kernels and only the ground state into account, one can solve the equation connecting the energy of the state and the decay of the correlator in Euclidean time at two different times to get the energy. This can be done in various ways either explicitly analytical or numerical.[1] Repeating this for all pairs of adjacent Euclidean times available on the lattice, one gets a value for the energy of the state for every pair of times. This value is called "effective mass" m_{eff}.

If the correlator contains only contributions of a single state, then the effective mass equals the mass of this ground state for every Euclidean time available. In numerical simulations, however, the statistical error for small Euclidean times is smaller than the one for large Euclidean times. The reason is that the signal decays with the kernel approximately exponentially in Euclidean time while the statistical error is independent of Euclidean time. Therefore it is preferable to use the value of the effective mass at small times to estimate the ground state mass to get a clean signal.

For real measurements this is unfortunately never the case and the correlator has contributions from higher energies. These are fortunately suppressed exponentially relative to the ground state, because the energy determines the strength of the decay in Euclidean time. Therefore it is preferable to take the value of the effective mass at large times for estimation of the ground state mass to get rid of excited state contaminations. In practice one has to find a compromise between statistical signal quality and small excited states contaminations.

[1] A set of solutions for the different kernels is collected e.g. in [64].

3.1.2 Ground State Width

The analysis of the effective mass to get the ground state mass has been in use in lattice QCD for a long time. Here an extension of this method is proposed which – in some limits – could be used to extract a finite ground state width from the effective mass, too. In place of a broadened ground state there can also be a close set of sharp states such that their different energies cannot be resolved by a measurement on the lattice. For such a structure the method would produce an effective width which corresponds to the spread of the sharp states. A third option to give such a signal is a broadened excited state which has a much higher spectral weight than the true ground state. Such a state needs extremely large Euclidean times to make it decay enough to see a signal of the true ground state.

It is most straightforward to examine the effect of a finite ground state width on the effective mass using some generic parametrization of a spectral function: Calculate the corresponding correlator and from that the effective mass. To get some direct insight into the relations, a parametrization is chosen which allows for some analytical treatment and explicit calculations. For the same reason the following paragraphs consider only the Laplace kernel for zero temperature $K(\tau, \omega) = e^{-\omega\tau}$. A generalization to finite temperatures should not pose additional problems apart from a gradual loss of analytical tractability due to the more complicated kernels. Also finite temperature introduces the new scale T which results in additional possibilities of asymptotic behaviour.

The parametrization of the spectral function should contain a broadened peak at small frequencies and some continuum contribution at higher frequencies. Already reference [85] proposed to use some parametrized peak and continuum as a model for the spectral functions. Specifically a Dirac delta peak plus a Heaviside theta contribution was proposed for the dimensionless spectral function $\tilde{A}(\omega) = A(\omega)/\omega^n$. Here a slightly generalized version of this proposition is used. The Dirac delta function is replaced by a Gaussian and the Heaviside continuum is replaced by an offset by ω_0 in the generic power law rising part of the continuum. The offset leads to a $n-1$ times continuously differentiable parametrization. The offset does, however, not change the continuum limit or introduce new parameters into the parametrization. The Gaussian of course comes at the expense of a new parameter σ for the width of the Gaussian. Nevertheless, the Dirac delta function can be always regained by sending σ to zero carefully, as some limits do not commute here.

These considerations result in the parametrization

$$A(\omega) = \frac{\Omega}{\sqrt{2\pi}\sigma} e^{-\frac{(\omega-\mu)^2}{2\sigma^2}} + m_0(\omega - \omega_0)^n \Theta(\omega - \omega_0), \tag{3.3}$$

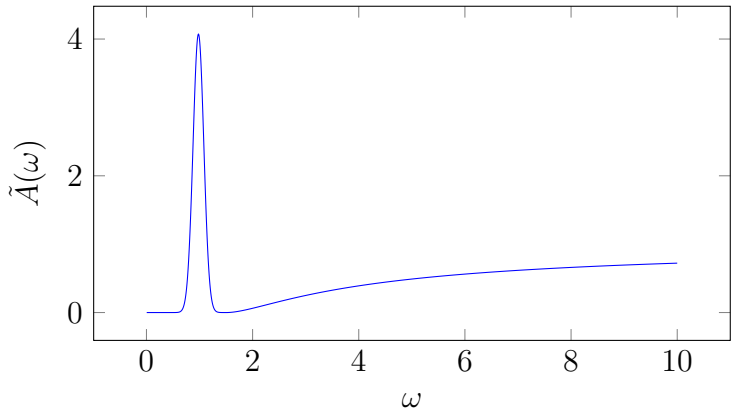

Figure 3.1: Example plot of $\tilde{A}(\omega) = A(\omega)/\omega^2$ with $A(\omega)$ from Equ. (3.3). The parameters are $\Omega = 1$, $\mu = 1$, $\sigma = 0.1$, $m_0 = 1$, $\omega_0 = 1.5$, and $n = 2$.

with the spectral strength Ω of a Gaussian resonance with energy μ and width σ, the beginning of the continuum ω_0, and the Heaviside theta function Θ. The power of the continuum contribution implies the energy dimension of the correlator. An example plot of the corresponding dimensionless spectral function $\tilde{A}(\omega) = A(\omega)/\omega^n$ is shown in Fig. 3.1.

Going from the spectral function to the correlator is in principle always straightforward given the kernel and using Equ. (3.2). As only the Laplace kernel is considered here it is possible to give an analytic expression for the correlator

$$C(\tau) = \frac{\Omega}{2} e^{\frac{1}{2}\tau\left(-2\mu+\sigma^2\tau\right)} \left(1 + \operatorname{erf}\left(\frac{\mu - \sigma^2\tau}{\sqrt{2}\sigma}\right)\right) + m_0 e^{-\tau\omega_0} \frac{n!}{\tau^{n+1}} \tag{3.4}$$

$$=: C_\Omega(\tau) + C_{m_0}(\tau), \tag{3.5}$$

where $\operatorname{erf}(z) = \frac{2}{\sqrt{\pi}} \int_0^z \mathrm{d}t e^{-t^2}$ denotes the error function.

Limit of the correlator for large Euclidean times

The physically interesting behaviour of the correlator in the context of an effective mass analysis is the limit of large Euclidean time.

The continuum contribution C_{m_0} is unchanged by the large τ limit and has (for dimensional reasons) an additional suppression for non-negative energy dimensions n by an inverse power law. This demonstrates the possibility for non-exponential behaviour of a correlator for large Euclidean times.

The ground state contribution C_Ω has a more interesting behaviour. To analyse it properly, one can introduce a dimensionless version $\tilde{C} = C_\Omega/\Omega$ dependent on the dimensionless parameters $\tilde{\tau} = \tau\mu$ and $\tilde{\sigma} = \sigma/\mu$.

To recover the case with an infinitely sharp state one can send first $\tilde{\sigma}$ to zero

$$\tilde{C}(\tilde{\tau}) = e^{-\tilde{\tau}} + \mathcal{O}(\tilde{\sigma}^2). \tag{3.6}$$

This is exactly the expected behaviour for a Dirac delta function like contribution.

Keeping a finite width $\tilde{\sigma}$ one has to expand in large Euclidean time τ first and then examine the resulting expression

$$\tilde{C}(\tilde{\tau}) = \frac{e^{-\frac{1}{2\tilde{\sigma}^2}}}{\sqrt{2\pi}\tilde{\sigma}} \frac{1}{\tilde{\tau}} + \mathcal{O}\left(\frac{1}{\tilde{\tau}^2}\right). \tag{3.7}$$

The decay of the correlator for large Euclidean times is again not exponential but governed by a power law.

Effective masses

To estimate what effect the large τ limits of the last paragraph have on actual lattice data analysis, one can take a look at the resulting effective masses.

In the continuum limit the effective mass m_{eff} of a correlator $C(\tau)$ for the Laplace kernel is given by

$$m_{eff}(\tau) = -\frac{\frac{\mathrm{d}}{\mathrm{d}\tau}C(\tau)}{C(\tau)}. \tag{3.8}$$

With this formula, an explicit expression for the effective mass is quickly derived for the analytic correlator of Equ. (3.4). More interesting are the separate cases where either the spectral weight of the continuum dominates, $m_{eff,m_0} = m_{eff}|_{\Omega=0}$, or the broadened peak, $m_{eff,\Omega} = m_{eff}|_{m_0=0}$.

The contribution of the continuum is given by

$$m_{eff,m_0}(\tau) = \omega_0 + \frac{1+n}{\tau}. \tag{3.9}$$

This is the behaviour of the effective mass due to a state with energy ω_0 for large Euclidean times and a correction from larger frequencies for small Euclidean time. Therefore already the continuum contribution alone displays all the features expected from a correlator consisting of a ground state and excited states contributions. Because of the exponential decay of the high energy contributions this effective mass signal should not be visible in correlators from lattice simulations: Any pronounced resonances in lower energy regimes lead to stronger effect.

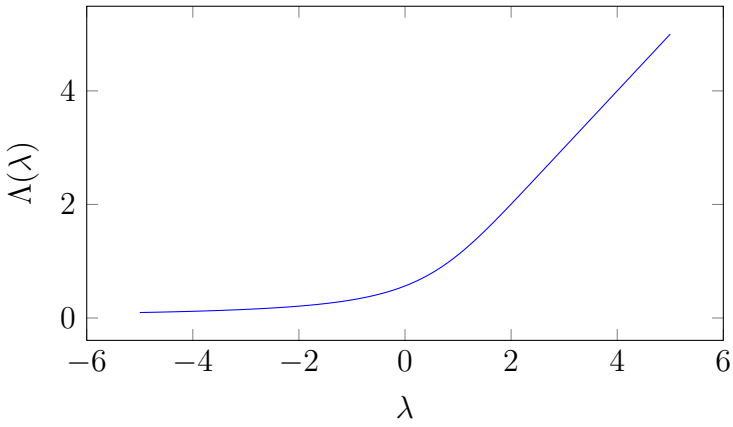

Figure 3.2: Behaviour of the function Λ from Equ. (3.12).

The contribution from a broadened state is given by

$$m_{eff,\Omega}(\tau) = \mu \left(1 - \tilde{\sigma}^2\tilde{\tau} + \sqrt{\frac{2}{\pi}}\tilde{\sigma}\frac{e^{-(1-\tilde{\sigma}^2\tilde{\tau})^2/2\tilde{\sigma}^2}}{1+\operatorname{erf}\left((1-\tilde{\sigma}^2\tilde{\tau})/\sqrt{2}\tilde{\sigma}\right)}\right) \tag{3.10}$$

$$= \mu\sqrt{2}\tilde{\sigma}\Lambda\left(\frac{1-\tilde{\sigma}^2\tilde{\tau}}{\sqrt{2}\tilde{\sigma}}\right) \tag{3.11}$$

with

$$\Lambda(\lambda) := \lambda + \frac{1}{\sqrt{\pi}}\frac{e^{-\lambda^2}}{1+\operatorname{erf}(\lambda)} \tag{3.12}$$

$$\overset{\lambda\to+\infty}{\to} \lambda + \mathcal{O}(e^{-\lambda^2}) \tag{3.13}$$

$$\overset{\lambda\to-\infty}{\to} -\frac{1}{2\lambda} + \mathcal{O}\left(\frac{1}{\lambda^2}\right). \tag{3.14}$$

The function Λ is plotted in Fig. 3.2. Both limiting cases are clearly visible in the plot. These two limits are separated by $0 \approx \lambda = \frac{1-\tilde{\sigma}^2\tilde{\tau}}{\sqrt{2}\tilde{\sigma}}$ or as $\tilde{\sigma} \geq 0$ by $\tilde{\tau} \approx 1/\tilde{\sigma}^2$.

In order for the term "width of state" to have a well defined meaning, $\sigma \ll \mu$ must be satisfied or $\tilde{\sigma} \ll 1$. Therefore for fixed $\tilde{\tau}$ one is always in the regime $\tilde{\tau} \ll 1/\tilde{\sigma}^2$ where $\lambda \gg 1$. In this regime the corrections to $\Lambda(\lambda) \approx \lambda$ are more than exponentially suppressed such that one can safely work in that approximation. Then the effective mass becomes approximately

$$m_{eff,\Omega}(\tau) \approx m_{eff,\Omega,approx}(\tau) = \mu\left(1 - \tilde{\sigma}^2\tilde{\tau}\right). \tag{3.15}$$

As the corrections to this formula are strongly suppressed, this relation gives a robust connection between the behaviour of the effective mass and both the mass and the width of the state. For example, to have a relative error of at most 10^{-3} for the effective mass from this approximation, it is sufficient at $\tilde{\sigma} = 0.1$ to keep $\tilde{\tau} \lesssim 130$. In the physical regime $\tilde{\sigma}^2$ is quite small such that the corrections to the

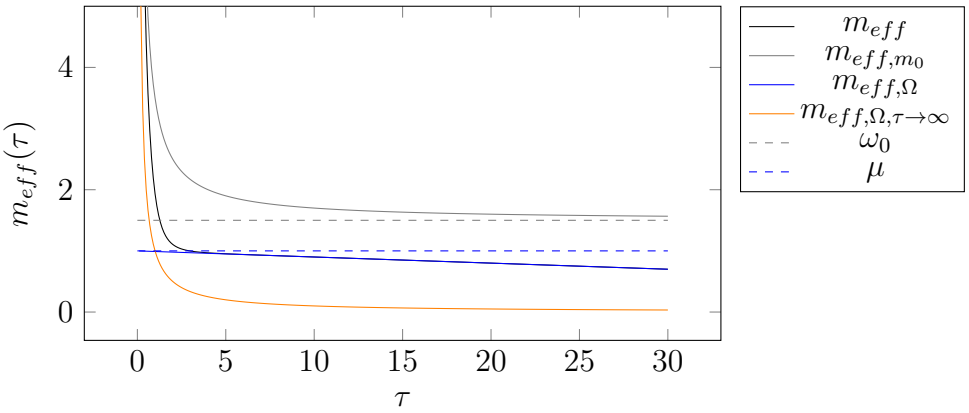

Figure 3.3: Example plot of effective masses for the spectral function given in Fig. 3.1.

expectation for Dirac delta function shaped peaks is also small. But it can well amount to percent level, e.g. at $\tilde{\sigma} = 0.1$, which is a realistic accuracy for current simulations.

The other limit $\lambda \to -\infty$ corresponds to the case where $\tilde{\sigma}$ is kept fixed and $\tilde{\tau}$ is sent to infinity. This is equivalent to calculating the effective mass of the correlator in the large τ limit in Equ. (3.7). Both result in an effective mass $m_{eff,\Omega,\tau\to\infty} = 1/\tau$ which vanishes for large Euclidean times. As explained in the last paragraph, this behaviour is not expected to be relevant in current lattice simulations.

As an example, Fig. 3.3 shows the expected effective masses for the same parameters as those taken in the example of the spectral function in Fig. 3.1.

This section showed that a remaining slope in the analysis of effective masses does not directly mean that some excited state contribution has not decayed enough, but may actually signal an effective width of the state under consideration. To measure this width one has to measure only the slope of the effective mass. This section assumed a Laplace transformation for going from the spectral function to the Euclidean correlator and a special, Gaussian parametrization of the finite spectral width of the state. The stability of the results under changes of both assumptions remains to be investigated but should not pose any problems.

3.2 Correlation Matrix Method

The last section 3.1 discussed how to extract some spectral information from a single correlator in a channel of a given set of quantum numbers. This way one can rather reliably extract information on the lowest energy state in that channel using the effective mass. This section expands that discussion to the case of multiple correlators corresponding all to a single channel.

3.2.1 Defining the Problem

In lattice QCD there are different operators O_i with the same quantum numbers and different overlap with physical states which are the energy eigenstates. From the lattice one can get expectation values of correlators $C_{ij}(\tau)$ of these operators

$$C_{ij}(\tau) = \langle O_i | e^{-\hat{H}\tau} | O_j \rangle \tag{3.16}$$

where $i, j \in \{1, 2, ..., n_C\}$, $\tau \in \{a, 2a, ..., n_t a\}$ is the Euclidean time, $\hat{H}$ is the Hamiltonian, $|O_j\rangle = \hat{O}_j|0\rangle$, and $|0\rangle$ the vacuum state.[2] C is called the correlation matrix, hence the name Correlation Matrix Method (CMM) (also called "Variational Method"). One can write $C_{ij}(\tau)$ also in spectral representation by inserting an orthogonal basis of energy eigenstates $\mathbb{I} = \sum_{n=1}^{n_E} |n\rangle\langle n|$ with $\hat{H}|n\rangle = E_n|n\rangle$

$$C_{ij}(\tau) = \sum_{n=1}^{n_E} {M^\dagger}_{in} M_{nj} e^{-E_n \tau} \tag{3.17}$$

with the matrix elements $M_{ni} = \langle n|O_i\rangle$. One wants to extract the energies and the matrix elements from C as they correspond more directly to physical information than the correlation matrix. In principle one can already extract this information from one correlator $C_{ii}(\tau)$ via multi parameter fits to the correlator or the Maximum Entropy Method (MEM) of section 3.3. However, these methods usually have a good grasp on the ground state, but an increasing error in the analysis of excited states. CMM accesses a matrix of correlator data instead of a scalar, thus uses more information, and tends to give better results in particular for the excited states.

3.2.2 The Generalized Eigenvalue Problem

A particularly elegant way to extract the energies is the solution of the generalized eigenvalue problem (GEP) [59]

$$C(\tau) v_n = C(\tau_0) v_n \lambda_n \tag{3.18}$$

with generalized eigenvectors v_n and generalized eigenvalues λ_n. For the case $n_E = n_O$ with linearly independent $|O_i\rangle$ one can construct an orthogonal basis $|\tilde{O}_i\rangle = \sum_j \omega_{ij} |O_j\rangle$ from the $|O_i\rangle$, e.g. by the Gram-Schmidt process. By inserting the spectral decomposition one can then show that $(v_n)_k = \sum_{ij} {\omega^\dagger}_{kj} \omega_{ji} {M^\dagger}_{in}$ defines a generalized eigenvector with the eigenvalue $\lambda_n = e^{-E_n(\tau - \tau_0)}$. This is a remarkable

[2] This relation is valid for the zero temperature case. For non-zero temperature the exponential has to be replaced by the finite temperature analogon according to section 2.1.4.

result as it delivers the information on all states already using only the information at two arbitrarily chosen times τ and τ_0. In contrast, in the effective mass analysis of the last section 3.1 one has to examine the infinite Euclidean time limit just to access the ground state without any information on excited states.

For $n_E > n_O$ one still gets the same results but this time again only in the limit of infinite Euclidean times with exponentially small corrections. For the case where $n_E < n_O$ the $|O_i\rangle$ are obviously not linearly independent any more and the GEP is in principle not suited any more. One might argue that in practical lattice calculations the number of energies or physical states is much larger than any number of operators which one can measure on the lattice in a limited (or even finite) amount of time. However, due to the Euclidean nature of the correlators, the effect of states with very high energy decays exponentially fast in Euclidean time. Therefore one is left to deal with the information of very few "rather" low energy states after very little Euclidean time. To be able to still use the GEP, one is effectively forced to reduce the set of considered operators up to the point where $n_{E,\text{effective}} = n_O$. Otherwise one has to deal with the effect of "increasing numerical noise" [25, 26, 78]. However, that reduces the information available to the analysis and thus the quality of the reconstructed energies and matrix elements. Therefore it is desirable to modify the method in such a way that additional linearly dependent operators can be included as they increase the information for the analysis and thereby should have a stabilizing effect on the results.

To test the GEP some numerical experiments with mock data have been conducted. The data is produced with Equ. (3.17) and $n_E = 4$, $E_1 = 0.1$, $E_2 = 0.3$, $E_3 = 0.6$, $E_4 = 1.0$, and M filled with uniform random numbers between -1 and 1.[3] Fig. 3.4 gives an example of the resulting effective masses $m_{i,eff}(t) = \log(\lambda_i(t)/\lambda_i(t+1))$ for the cases where $n_E > n_O = 3$, $n_E = n_O$, and $n_E < n_O = 10$. The reconstructed higher energies break off at some τ because of the numerical error introduced by computing in finite numerical precision (machine precision). One can see both the exponentially vanishing correction to the effective masses for $n_E > n_O$ and the "increasing numerical noise" for $n_E < n_O$.

As there is a continuum of physical states in continuum theory one might expect a similar phenomenon on the lattice. To see its effect on the solution of the GEP, an additional continuum term is introduced in the mock data. The spectral function of the continuum contribution, i.e. its inverse Laplace transformation, is for mesonic correlators of the form ω^2 with ω being the energy of the state.

[3] If not stated otherwise, all quantities with non-zero dimension are given in lattice units in this section.

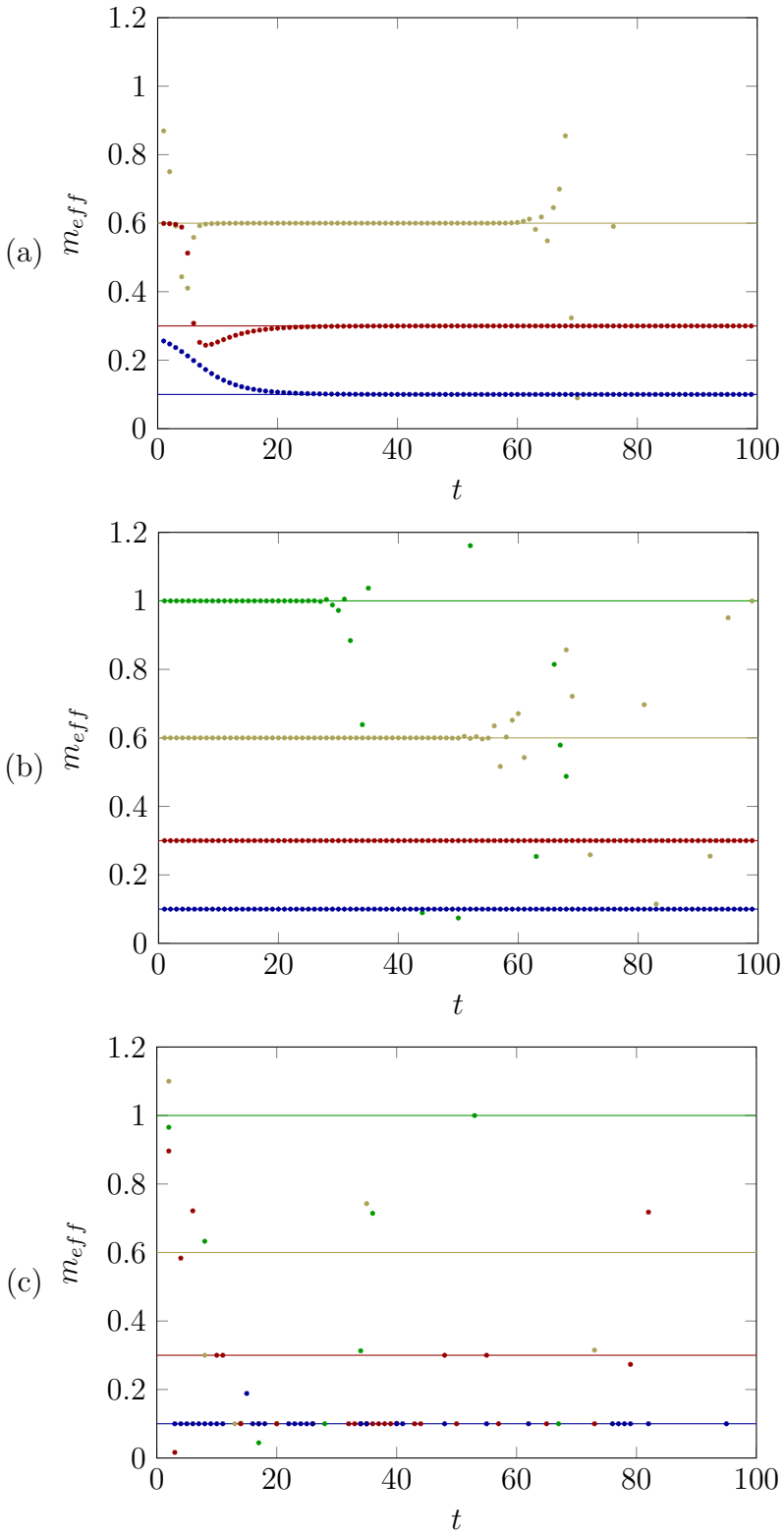

Figure 3.4: Examples of the effective masses for the GEP for $n_E > n_O = 3$ (a), $n_E = n_O$ (b), and $n_E < n_O = 10$ (c).

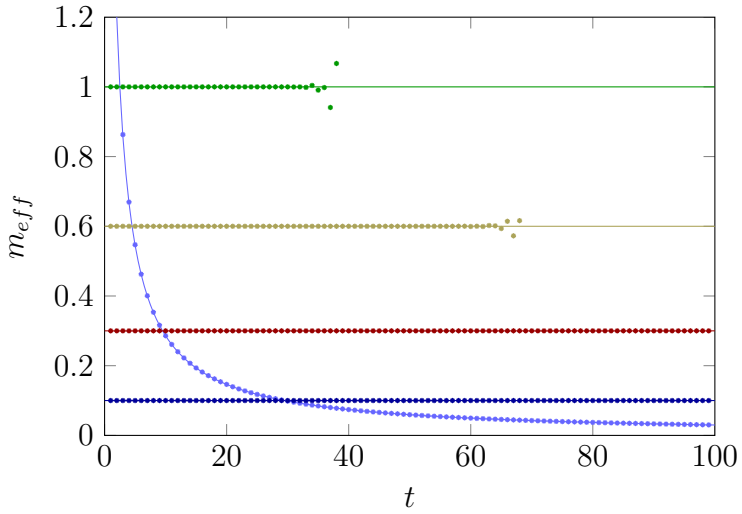

Figure 3.5: Examples of the effective masses for the GEP with continuum contribution.

As the Laplace transformation and the sum in Equ. (3.17) are linear, one can simply add the continuum contribution which is then $\int_0^\infty d\omega e^{-\omega\tau}\omega^2 \propto \tau^{-3}$. In all other respects the continuum is treated like an additional energy eigenstate, i.e. its coupling to the operators is given by another set of random numbers which basically leads to an additional row in M. Of course the continuum contribution has to be normalized with some factor N to adjust its effect to that of a discrete energy eigenstate. The resulting mock data is then defined by

$$C_{ij}^{\text{cont}}(\tau) = C_{ij}(\tau) + M^\dagger{}_{ic} M_{cj} \frac{N}{\tau^3} \tag{3.19}$$

with $N = 0.01$. The effective masses from the GEP with $n_O = n_E + 1 = 5$ are plotted in Fig. 3.5. The continuum contribution indeed adds another state with Euclidean time dependent effective mass. Like in section 3.1 this dependence is given by $(1+n)/\tau$, with n being the exponent of the continuum parametrization, here $n = 2$.

Also in section 3.1, the effect of Gaussian broadened states on the effective mass was investigated. It led to an approximately linear dependence of the effective mass on the Euclidean time. To represent this in the mock data, the spectral representation was changed to an integral representation

$$C_{ij}^{\text{gauss}}(\tau) = \int_0^\infty \mathrm{d}\omega \sum_{n,m=1}^{n_E} M^\dagger{}_{in} \left(\frac{e^{-\frac{(-E_n+\omega)^2}{2\sigma_n^2}}}{\sqrt{2\pi}\sigma_n} \right)^{\frac{1}{2}} e^{-\omega\tau} \left(\frac{e^{-\frac{(-E_m+\omega)^2}{2\sigma_m^2}}}{\sqrt{2\pi}\sigma_m} \right)^{\frac{1}{2}} M_{mj} \tag{3.20}$$

where $\sigma_n = 0.1E_n$ is chosen. To be entirely consistent, one has to remark that the normalization of M is different in C^{gauss} than in C and C^{cont} to account for

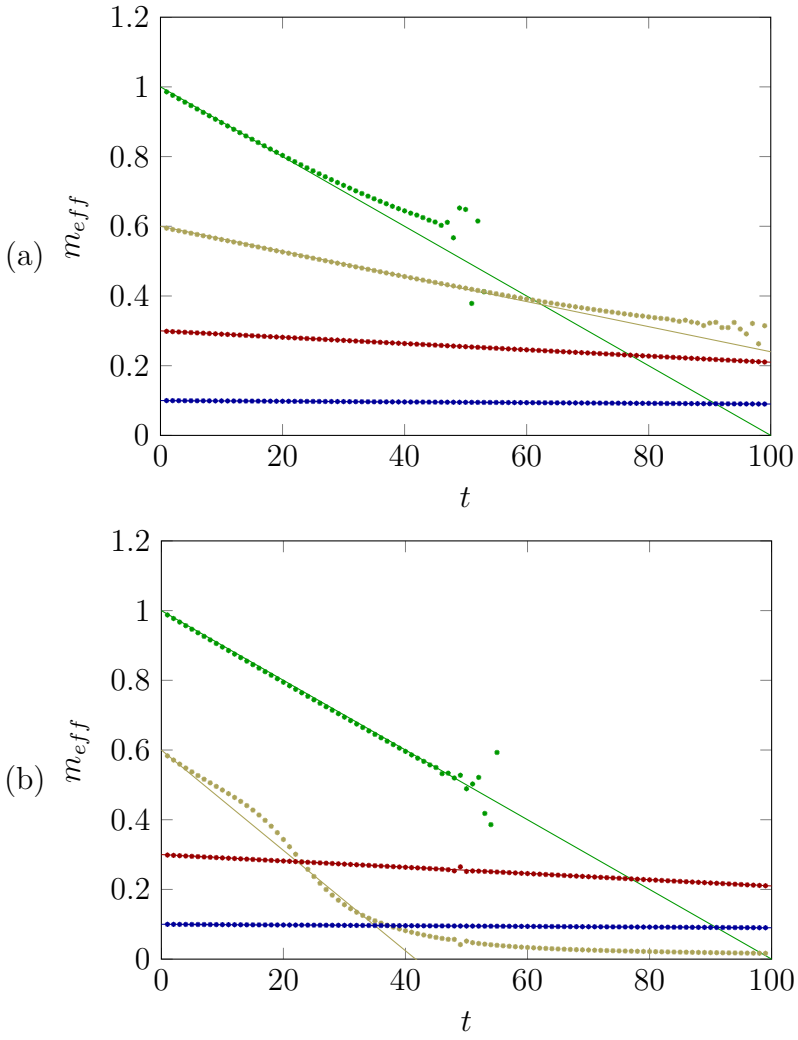

Figure 3.6: Examples of the effective masses for the GEP with Gaussian broadened states (a) with widths of a tenth of the mass of the state and (b) like (a) but with the width of the third state doubled.

the additional integration. For evaluations the integral is approximated by a sum. The result of the GEP is shown in Fig. 3.6. The approximately linear behaviour which was expected from section 3.1 is clearly visible. Also given in Fig. 3.6 is the case where σ_3 is doubled and all the other parameters are unchanged. At Euclidean times, where two effective masses of the broadened states are nearly identical, there is a deviation from the approximate linear behaviour.

In numerical lattice studies the main problem is of course the error of the data points which is much larger than the 10^{-16} resulting from the limited machine precision. Therefore also the stability of the GEP with respect to the addition of Gaussian noise to the data is investigated. Following [9] the variance of the noise is chosen as $\sigma_{ij}(\tau) = bC_{ij}(\tau)\tau$ with the real parameter b controlling the noise level. Fig. 3.7 shows the resulting effective masses for different values of b. One can see that with increasing noise level the length of the plateaus in the effective

energy decreases. As mentioned earlier it would be desirable to find a more stable reconstruction which yields longer plateaus, e.g. by a method which uses more data from linear dependent operators.

3.2.3 Different Approaches

Already [59] states that also the solution of the ordinary eigenvalue problem (EP)

$$C(\tau)v_n = v_n\lambda_n \tag{3.21}$$

gives eigenvalues which are proportional to $e^{-E_n\tau}$ for large Euclidean times with exponentially small corrections. Actually this is a quite general phenomenon for triangular matrix decompositions of $C(\tau)$. The eigenvalue problems can also be rewritten as matrix decompositions of $C(\tau)$. For the LU decomposition

$$C(\tau) = L(\tau)U(\tau) \tag{3.22}$$

with the lower triangular matrix $L(\tau)$ and the upper triangular matrix $U(\tau)$ and L having only the value 1 on its diagonal, the effective masses of the diagonal of $U(\tau)$ give the correct result for large Euclidean times. In the Choleski decomposition

$$C(\tau) = L(\tau)L(\tau)^\dagger \tag{3.23}$$

with the lower triangular matrix $L(\tau)$ the square of the diagonal of $L(\tau)$ gives the correct effective masses for large τ. In case of the QR decomposition

$$C(\tau) = Q(\tau)R(\tau) \tag{3.24}$$

with the unitary matrix $Q(\tau)$ and the upper triangular matrix $R(\tau)$, the diagonal of $R(\tau)$ contains the same information. The same is true for the singular values $\sigma_n(\tau)$ of the Singular Value Decomposition (SVD)

$$C(\tau) = U(\tau)\Sigma(\tau)V^\dagger(\tau) \tag{3.25}$$

with unitary $U(\tau)$ and $V(\tau)$ and the diagonal matrix $\Sigma(\tau)$ of the $\sigma_n(\tau)$.[4]

Examples of the reconstruction of the same mock data ($n_E = n_O = 4$) with these methods are given in Fig. 3.8. All methods can in principle resolve the states and show some (exponential) decay to the correct splitting. The data for the Choleski decomposition is not shown as it is only stable for small times where

[4]"SVD" in this context generally means "Compact SVD", i.e. a decomposition where $\Sigma(\tau)$ is a $k \times k$ diagonal matrix and $U(\tau)$ and $V(\tau)$ are $n_O \times k$ matrices with k the rank of $C(\tau)$.

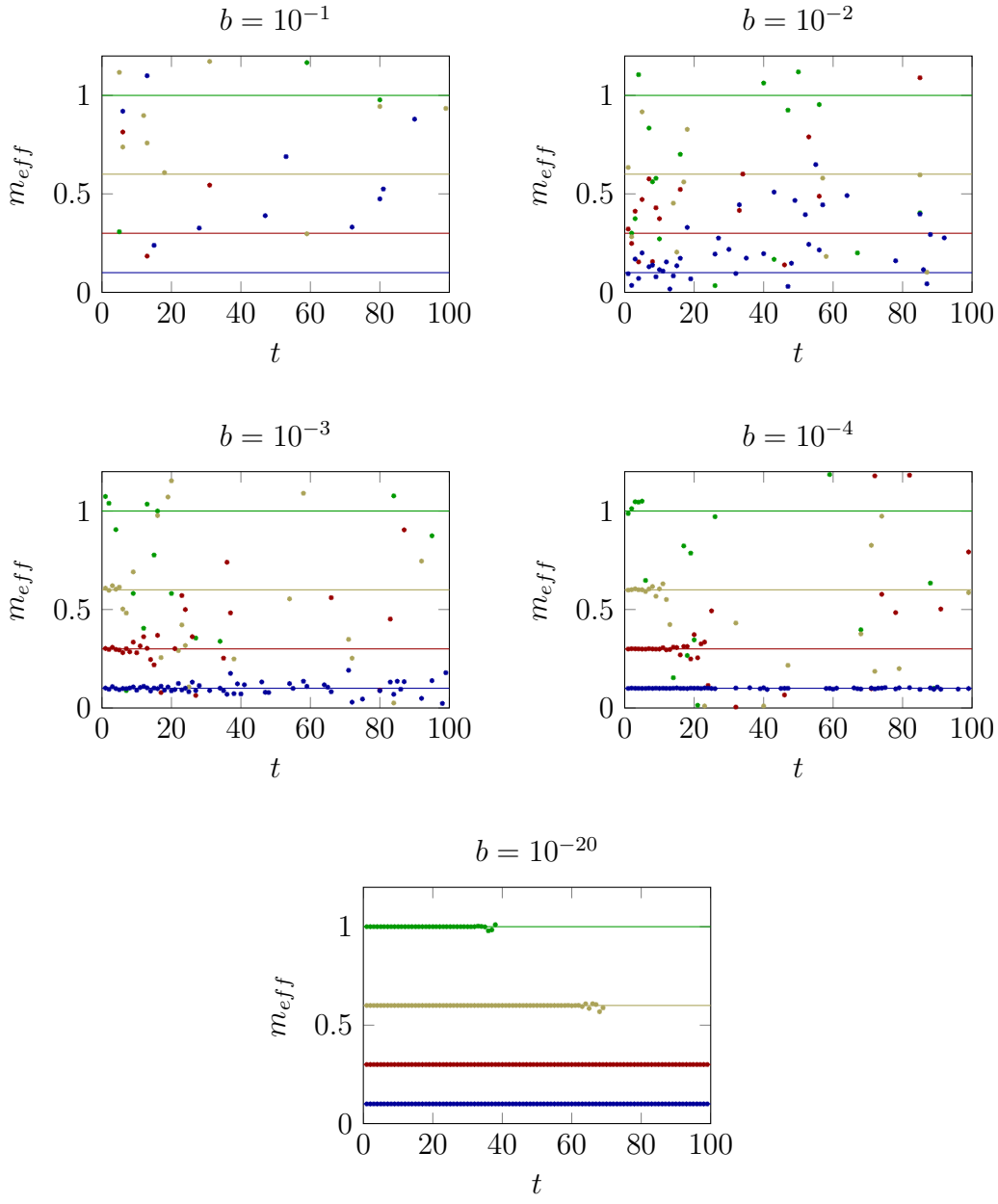

Figure 3.7: Examples of the effective masses for the GEP with Gaussian noise on discrete states for different noise levels b. The last reconstruction with $b = 10^{-20}$ is a reference reconstruction with noise below machine precision.

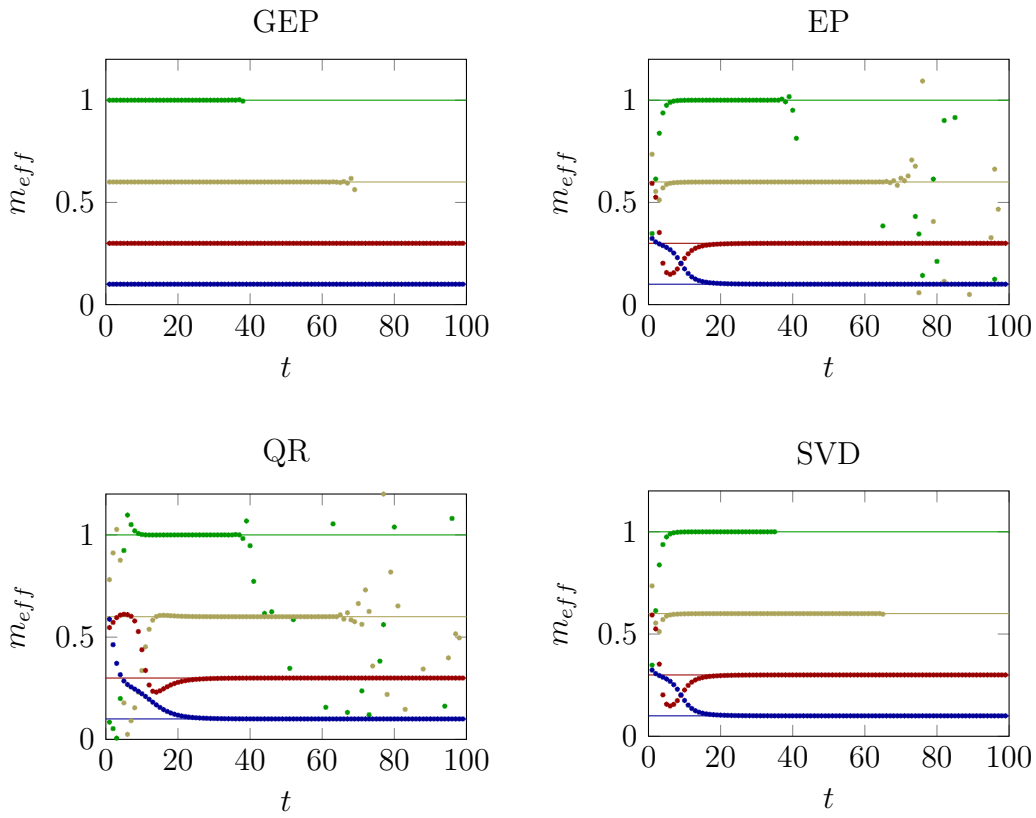

Figure 3.8: Examples of the effective masses for different matrix decompositions.

the correlation matrix is "positive definite enough" for a numeric decomposition in machine precision. The used SVD implementation seems to be able to detect quite well when a singular value is consistent with zero for a given accuracy. Therefore it gives a clear cutoff in the effective masses. But none of the methods seems to give an improvement over the GEP at this point.

To examine the performance of the methods for linear dependent operators, the results of experiments with $4 = n_E < n_O = 10$ are given in Fig. 3.9. The GEP seems to have problems with the linear dependent operators, the others are rather stable.

For normal, positive semi-definite matrices SVD is identical to EP. For matrices without full rank SVD finds an "optimal" subspace with orthogonal basis built from the linear dependent columns. Therefore SVD and its relative, the ordinary EP, are good candidates for a more stable improvement of the GEP. However, they lack the property to reconstruct the effective masses also at small Euclidean times. An optimal solution would combine both characteristics.

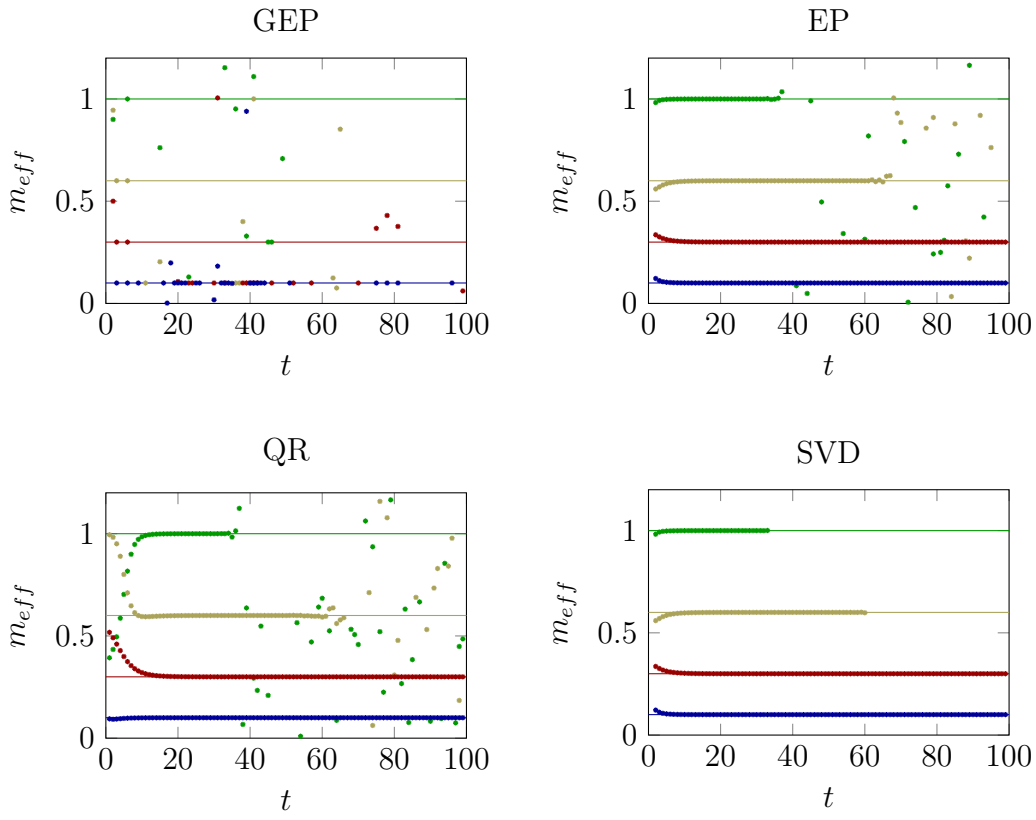

Figure 3.9: Examples of the effective masses for different matrix decompositions and more operators than states.

3.2.4 Modification of the GEP

As mentioned earlier, the GEP in Equ. (3.18) can be rewritten as a matrix decomposition

$$C(\tau) = C(\tau_0) v \Lambda v^\dagger \tag{3.26}$$

with $v = (v_1|...|v_n)$ the orthonormal basis of eigenvectors and Λ the diagonal matrix consisting of generalized eigenvalues. This is of course equivalent to an ordinary eigenvalue problem

$$\tilde{C}(\tau_0, \tau) = v \Lambda v^\dagger \tag{3.27}$$

with $\tilde{C}(\tau_0, \tau) = C(\tau_0)^{-1} C(\tau)$. This is exactly where the problems with linearly dependent operators come in: $C(\tau_0)$ is no longer invertible as it does not have the full rank. The numerical inversion of such a matrix introduces large numerical errors. Therefore an alternative to the ordinary matrix inversion is needed. With the help of the SVD of $C(\tau_0)$

$$C(\tau_0) = U(\tau_0) \Sigma(\tau_0) V^\dagger(\tau_0) \tag{3.28}$$

it is possible to construct such a pseudo inverse

$$PI(\tau_0) = V(\tau_0) \Sigma(\tau_0)^{-1} U^\dagger(\tau_0). \tag{3.29}$$

This pseudo inverse always exists and is equal to the ordinary inverse for invertible matrices. Furthermore, by performing the inversion via the SVD one can cut the singular value spectrum off at some limit to get rid of small singular values which only come from numerical errors or noise in the data ("truncated SVD"). If one chooses the cutoff so large that only one singular value remains, the pseudo inverse is proportional to the identity, because $C(\tau_0)$ is normal and positive definite enough for $U \approx V$ and U, V are unitary. Then the pseudo inverse method is equivalent to solving the ordinary EP. If one chooses a very low cutoff, the pseudo inverse is the actual inverse for linearly independent operators and the method is equivalent to solving the GEP. Given a noisy correlation matrix C, one should be able to find the clearest signal by tuning the cutoff.

Using the pseudo inverse one still has to solve a n_O dimensional EP. But the (truncated) SVD already defines a maximum number of states taken into account for a small τ_0. All Euclidean times $\tau > \tau_0$ provide less information on the excited states and the number of contributing states is at most the number at the time τ_0. The other reconstructed eigenvalues will only correspond to noise. Therefore

one can also reformulate the problem as an eigenvalue problem with a size equal to the number k of considered singular values at time τ_0

$$\bar{C}(\tau_0, \tau) = \bar{v}\bar{\Lambda}\bar{v}^{\dagger} \tag{3.30}$$

with the $k \times k$ matrices $\bar{v}$ and $\bar{C}(\tau_0, \tau) = \Sigma(\tau_0)^{-1} U^{\dagger}(\tau_0) C(\tau) V(\tau_0)$, and the diagonal matrix of eigenvalues $\bar{\Lambda}$.

This modified procedure, call it "Singular Decomposed General Eigenvalue Problem" (SDGEP), should now combine the good properties of all methods:

- good state resolution for small Euclidean times τ (from GEP)
- good stability also for a larger set of linear dependent operators (e.g. EP, QR, SVD)
- possibility to restrict the noise in the analysis by a cutoff in the spectrum of singular values (SVD).

Also, due to the SVD there is the potential for reducing the computational effort for an analysis, because the SVD reduces the size of the eigenvalue problem which has to be solved for all Euclidean times. This is a convenient property, even though computational cost is not the limiting factor for this part of the analysis. The expected tolerance with respect to linear dependent operators should then open a new direction for the application of the "law of large numbers" to reduce the error of lattice results by including more operators with the same quantum numbers without the effect of "increasing numerical noise".

To see the relative performance of the GEP, the EP, and the new SDGEP under quasi real conditions, another two sets of numerical tests were performed. In the first set again $n_E = n_O = 4$ was chosen and in the second set $4 = n_E < n_O = 10$. Both sets have Gaussian noise in the mock data. The cutoff for the singular values in the new method is given relative to the largest singular value. The results of the first set are shown in Fig. 3.10. One can see that the GEP shows the characteristic good behaviour for small Euclidean times whereas the EP is more stable for larger Euclidean times. The new SDGEP method gives somewhat intermediate results for the chosen cutoffs.

The second set is presented in Fig. 3.11. The GEP was not able to cope with the linear dependent operators and is therefore excluded from this presentation. The EP and the new method both show the good behaviour for large times. However, the new method does also show the elimination of the exponential corrections to the effective mass for small Euclidean times like the GEP. Because the second data set is bigger, i.e. the number of operators is larger, the fluctuations of the

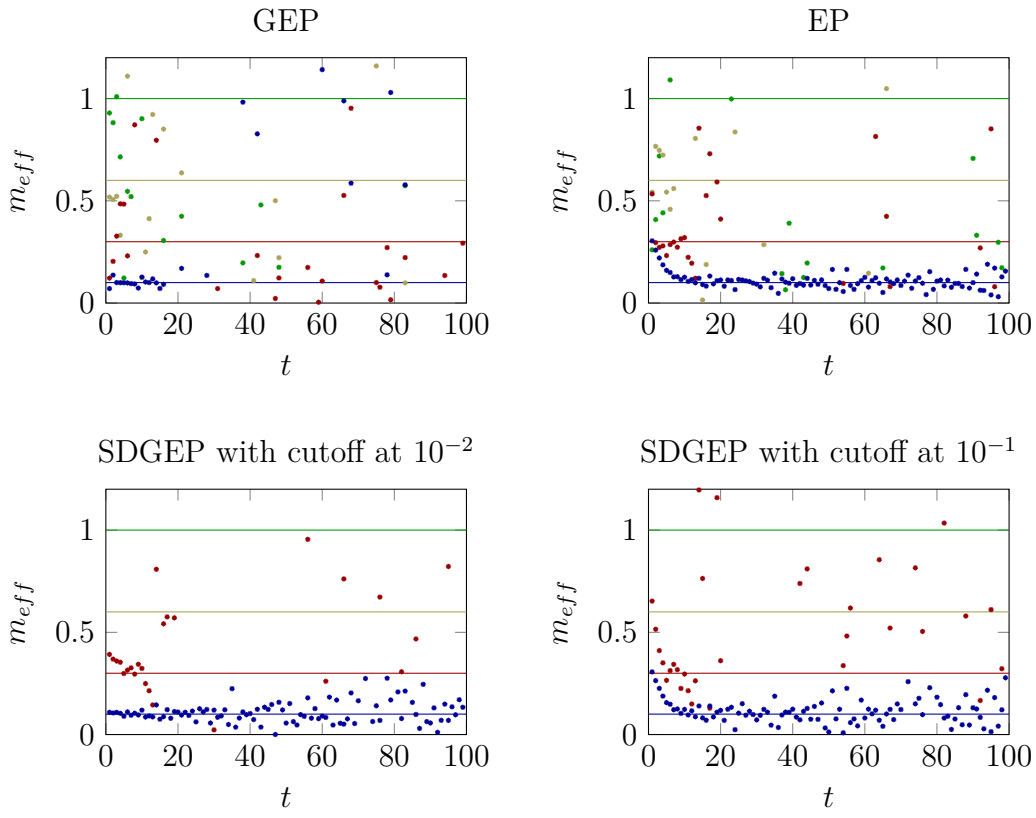

Figure 3.10: Examples of the effective masses for $n_E = n_O = 4$ at a noise level $b = 10^{-3}$.

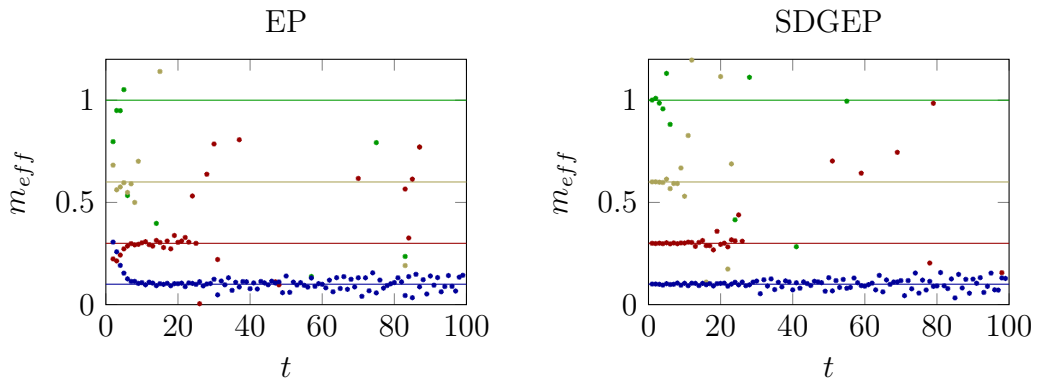

Figure 3.11: Examples of the effective masses for $4 = n_E < n_O = 10$ at a Gaussian noise level $b = 10^{-3}$ for EP and SDGEP. The SDGEP singular value spectrum was cut off at 10^{-2}.

reconstructions are smaller than for the first set. There is no sign of the "increasing numerical noise" by including a larger number of sources. This is valid even for the case of 100 operators which is not shown in the plot.

3.2.5 SDGEP Performance

In order to test the ability to resolve excited states, the lengths of the plateaus in the effective mass in Euclidean time are studied. The length of a plateau L_p is defined as the maximum number of points in Euclidean time for which the value of the effective mass does not differ from the true value of the mass of the state in the mock data by more than 5% for every point in Euclidean time smaller than or equal to L_p. For the tests mock data with four states of the energies $\{0.1, 0.3, 0.6, 1.0\}$ are used. The singular value spectrum is cut at the fourth value.

Fig. 3.12 gives the length of the plateau. The graphs are in essence shifted in direction of higher noise by adding additional linear dependent operators. That is expected since the amount of information is increasing with the number of operators. This indicates that using more linear dependent operators makes the analysis more tolerant against noise. The graph for $n_O = 64$ is added to the plot in order to show that the method is stable for very large numbers of operators. There is no sign of increasing numerical noise, which means that one can – without problems – use more operators than resolvable physical states in the analysis.

Naively, the gain in performance is expected to scale with the square root of the number of operators when their statistical noise is uncorrelated. The computational cost to calculate a cross correlation matrix scales with the square of the number of operators, which would render the additional operators quite expensive. But as the additional operators involve different linear combinations of

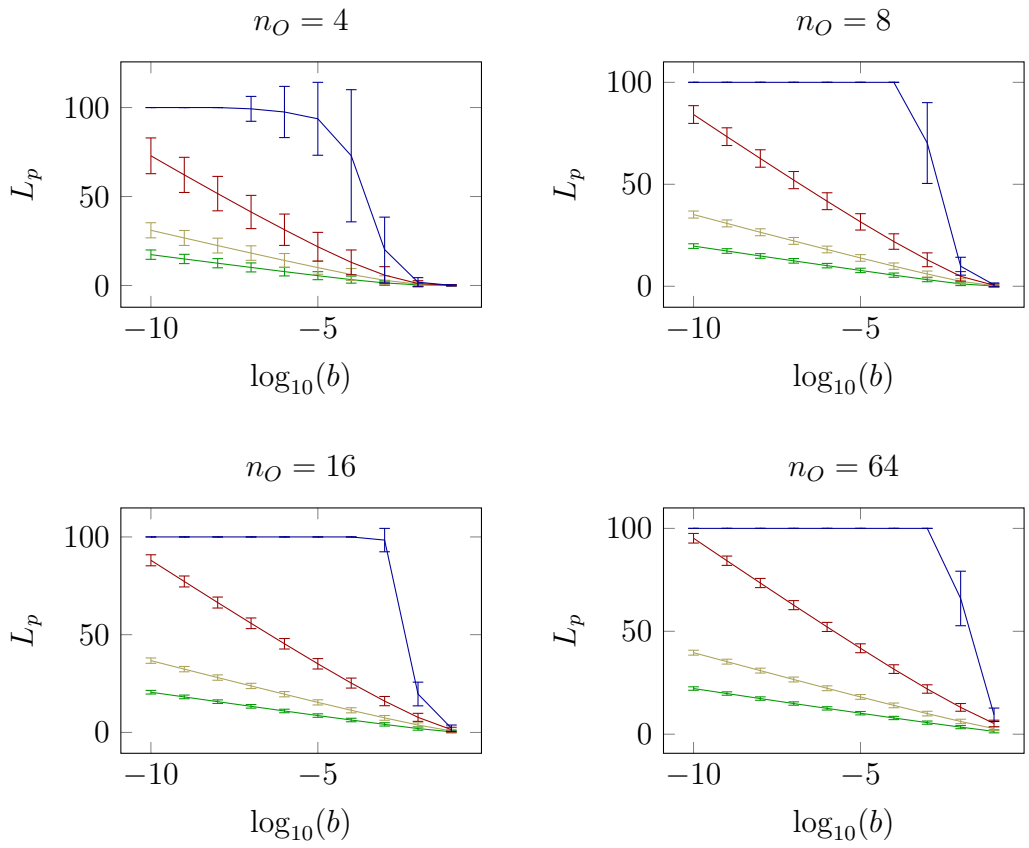

Figure 3.12: Length of the plateau L_p in the effective energy for the four states in dependence of the noise level b for different choices of n_O. For this plot 100 random couplings of the operators to the states have been used and also 100 realizations of the noise on the data for each coupling.

the eigenstates, they are of more use than just reducing the statistical fluctuations: They stabilize the generalized eigenvalue problem by spanning the operator space in a more stable way. This effect is seen to be stronger for smaller numbers of operators, as then the additional operators indeed contribute additional linear combinations which are not yet similarly realized in the previous set of operators. This is especially true for the randomly chosen overlaps in this example. The effect is also stronger for the states with higher energy, as their reconstruction depends heavily on the performance of the generalized eigenvalue problem and a stable spanning of the operator space.

Fig. 3.13 shows the maximum tolerable noise level in dependence of the number of operators n_O for every state separately. The effects described above lead here to an increase in performance, i.e. tolerance to noise in the reconstruction of the highest energy state, of one order of magnitude already with a moderate increase in n_O, e.g. from 4 to 8, where the cost for the calculation of the matrix only increases by a factor of 4.

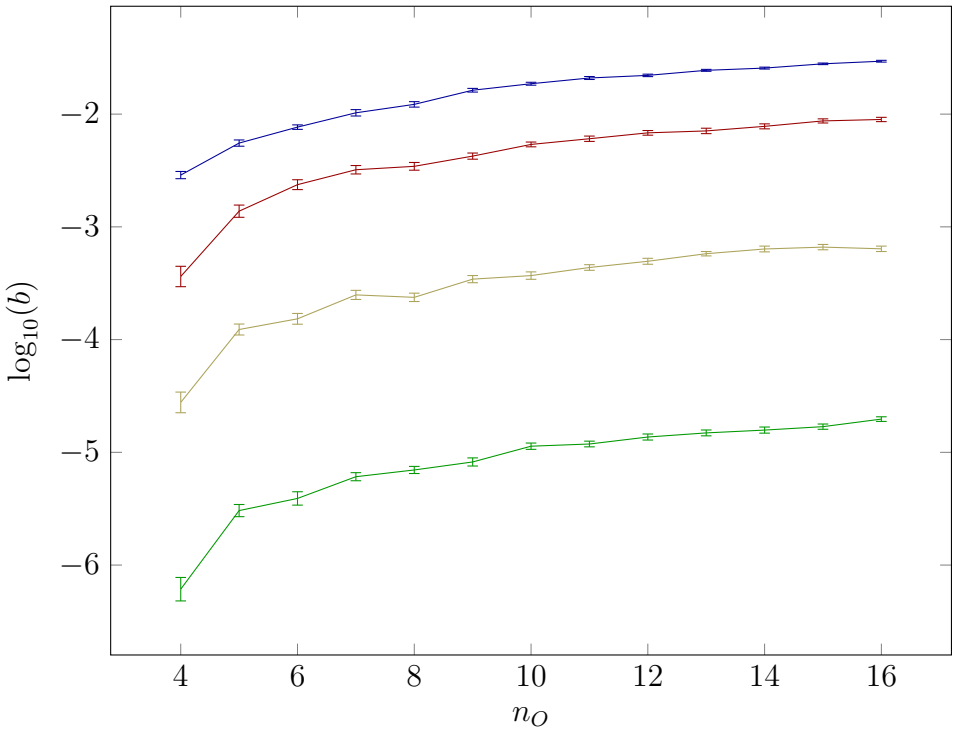

Figure 3.13: Maximum tolerable error level b to get a plateau of length 8. For this plot 100 random couplings of the operators to the states have been used and also 100 realizations of the noise on the data for each coupling.

To check whether the gain in performance is only achieved due to a systematic effect in the choice of the random weights with which the operators couple to the states, the tests have been performed again with the n_O dimensional weight vectors randomly distributed on the $n_O - 1$ unit sphere. The results of this test are given in Figs. 3.14 and 3.15. They are essentially unchanged. This shows the stability of the gain of the method with respect to changes in the random choice of the operators.

3.2.6 Summary

This section presented the Correlation Matrix Method or Variational Method. It showed that the behaviour of the effective masses for the different energy eigenstates is the same as the one given in section 3.1 for Gaussian broadened states and a continuum contribution. Therefore, it should in principle be possible to determine not only the mass but also the width of states from the variational analysis. Additionally a modification of the standard algorithm, the solution of a generalized eigenvalue problem, is proposed which is free of numerical instabilities which show up when the number of correlators becomes too large. This makes it possible to include an arbitrarily large number of operators in the correlation matrix to make the analysis significantly more stable. For the mock data, this

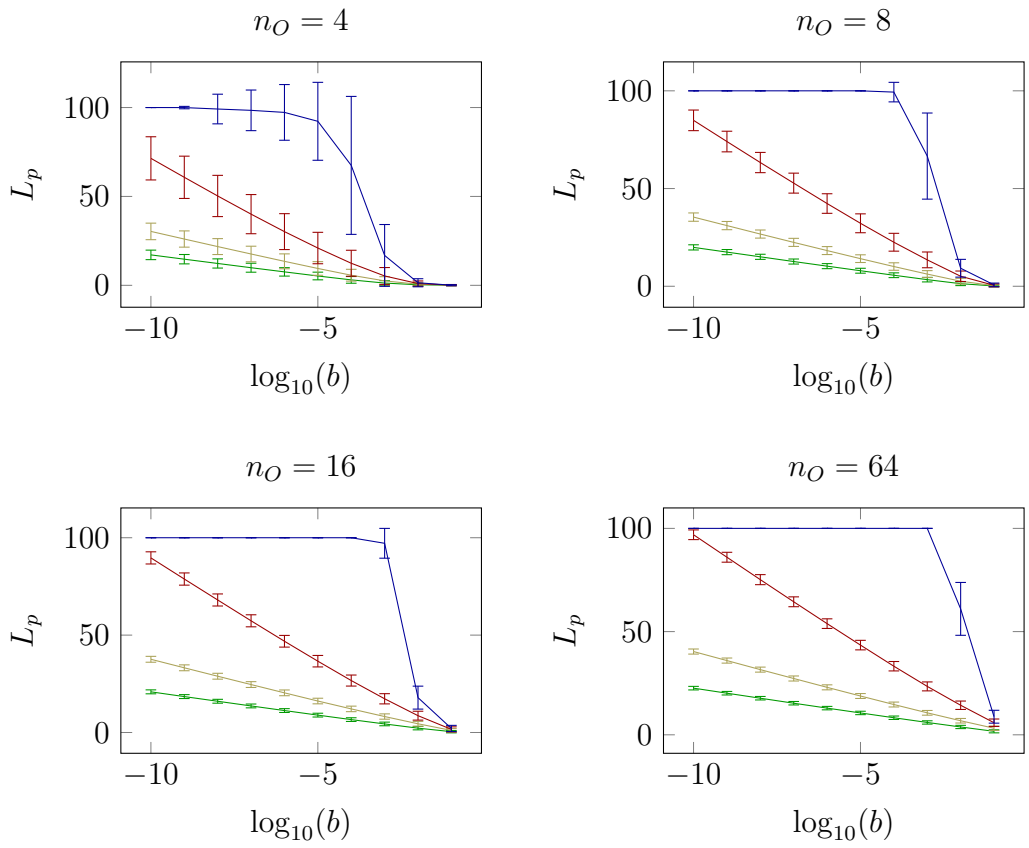

Figure 3.14: Same as Fig. 3.12 but for weight vectors randomly picked from the unit sphere.

leads to an increased tolerance to noise of about an order of magnitude compared to the standard generalized eigenvalue problem.

3.3 Maximum Entropy Method

The last sections introduced methods for reconstructing the spectral information of a discrete set of states. This section will take a different approach to reconstruct a full continuous spectral function[5] which is, in principle, completely unrestricted. This spectral function could directly give a lot of physically interesting quantities like masses and widths of states, transport properties at low energies, and the continuous spectrum of scattering states at high energies.

[5]On the lattice the precise meaning of a continuous spectral function reconstructed from finite volume lattice data is not completely clear as is noted e.g. in [78]. They prefer to reconstruct a discrete spectral function for the lattice using the variational method.

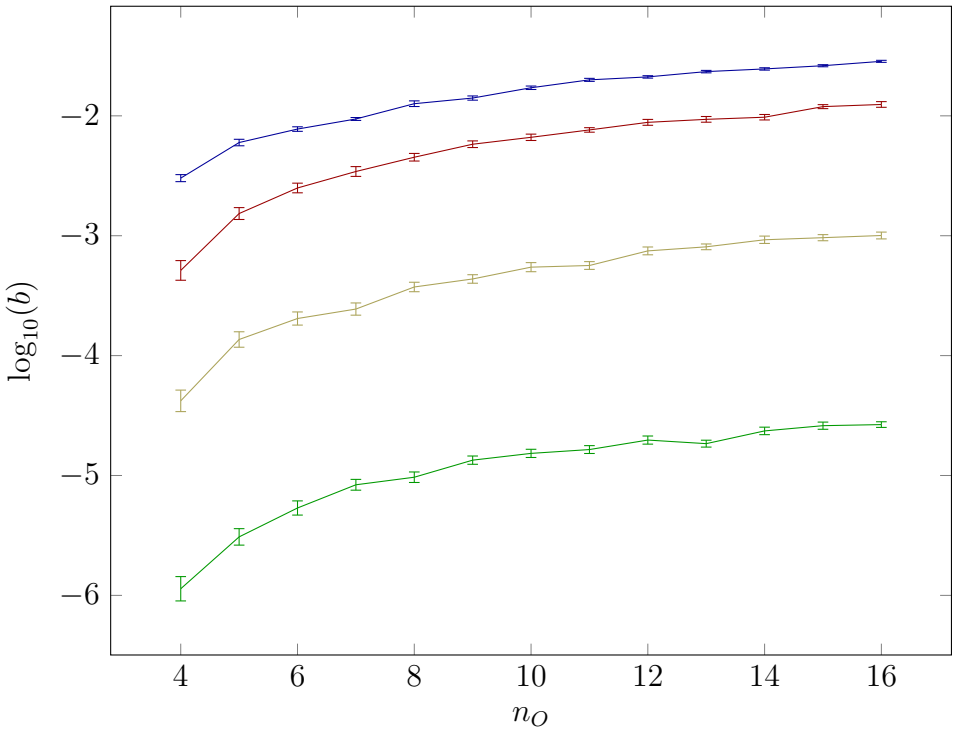

Figure 3.15: Same as Fig. 3.13 but for weight vectors randomly picked from the unit sphere.

3.3.1 General

The task of the Maximum Entropy Method (MEM) is to directly reconstruct the spectral function introduced in section 2.1.4, e.g. Equ. (2.39). This short general introduction is mainly based on [9, 53, 64]. Throughout this section the spectral representation is given in the following notation

$$C(\tau) = \int_0^\infty \mathrm{d}\omega A(\omega) K(\tau, \omega) \tag{3.31}$$

with the Euclidean correlator C, the spectral function A, and the integral kernel K. The covariance matrix of the correlator measurements $C(\tau_i)$ is Σ_{ij}.

The problem in reconstructing an unrestricted continuous spectral function from lattice data is that one does not get an analytic function for the correlators as a result of lattice simulations. Therefore one cannot perform the transformation to the spectral functions exactly, i.e. the inversion of Equ. (3.31). All one gets from the lattice, is a limited set of noisy data for the correlator, usually $N_\tau \sim \mathcal{O}(10)$ points. From this data one wants to reconstruct an approximately continuous spectral function, which might need $N_\omega \sim \mathcal{O}(1000)$ points. If no additional information is available, the minimization of its χ^2 is an ill defined problem. With C_A being defined via Equ. (3.31), for some candidate spectral function A the χ^2

reads

$$\chi^2 = \sum_{i,j}^{N_\tau} (C(\tau_i) - C_A(\tau_i)) \Sigma_{ij}^{-1} (C(\tau_j) - C_A(\tau_j)). \tag{3.32}$$

MEM uses additional information in a form which is quantifiable with Bayesian inference theory, namely prior knowledge about the spectral function, like its positivity, and introduces an additional term in the process of reconstruction: The Shannon-Jaynes Entropy

$$S = \sum_{l=1}^{N_\omega} \left(A(\omega_l) - m(\omega_l) - A(\omega_l) \log \left(\frac{A(\omega_l)}{m(\omega_l)} \right) \right). \tag{3.33}$$

This term tends to fit the reconstruction to a default model m which is also part of the prior knowledge. This default model usually describes the high energy limit of the spectral function which is known from perturbation theory or the dimension of the correlator under consideration. This additional information stabilizes the reconstruction of the spectral function. MEM finds the most likely spectral function and returns it as unique result by minimizing $-Q := \frac{1}{2}\chi^2 - \alpha S$ with a positive relative weight α.

The standard algorithm to solve this minimization problem is called "Bryan's Method". It relies on the singular value decomposition of the kernel

$$K = V \Xi U^t \tag{3.34}$$

to reformulate the N_ω dimensional minimization problem into a N_τ dimensional minimization problem with the new minimization variables

$$b_i = \sum_{l}^{N_\omega} A(\omega_l) U_{li}. \tag{3.35}$$

This results in a huge speed-up of the analysis and also reduces the potential for numerical errors.

An alternative algorithm was introduced in [53], which also restricts the problem to a N_τ dimensional subspace but works without singular value decomposition. Additionally it also eliminates the need to invert the covariance matrix, which is in most cases for real data not well conditioned. This makes the method cheaper and more stable against numerical errors. For this method one defines a new minimization variable

$$s_i = -\frac{1}{\alpha} \sum_{j}^{N_\tau} \Sigma_{ij}^{-1} (C_A(\tau_j) - C(\tau_j)). \tag{3.36}$$

Then the minimization of $-Q$ can be rewritten as a minimization of

$$U = \frac{\alpha}{2} \sum_{i,j}^{N_\tau} s_i \Sigma_{ij} s_j + \sum_{l}^{N_\omega} A(\omega_l) - \sum_{i}^{N_\tau} C(\tau_i) s_i. \tag{3.37}$$

There is some arbitrariness in defining the objective functions for the minimization $-Q$ and U, which is the relative weight α between the two components. This can be eliminated by marginalizing over α. The remaining arbitrariness is then in the choice of the default model m.

3.3.2 Generic Default Model

The most common choice for the default model m is the asymptotic behaviour of the correlator for high energies

$$m(\omega) = m_0 \omega^n, \tag{3.38}$$

where m_0 is dimensionless and n is then fixed by the dimension of the correlator. For mesonic correlators $n = 2$, for baryonic correlators $n = 5$, and for correlators of the energy momentum tensor $n = 4$.

The parameter m_0 can be determined, at least for point-to-point correlators, from perturbative QCD calculations as it describes the limiting behaviour of the theory for large energies where asymptotic freedom reigns and the coupling is small. This calculation has to be redone for every considered channel and every source and sink type as they change the high energy contributions of the correlator. This is clearly not a situation which is favourable for fast, stable, and, if possible, automatic analyses. Here a method is proposed how to estimate this parameter for a given lattice measurement of a correlator. As the features of the reconstructed spectral function should, for a sufficiently precise measurement of the correlator, not depend on the precise value of m_0, an estimate of the order of magnitude is sufficient.

High energy contributions of the spectral function correspond to small Euclidean time distances of the Euclidean correlator. In this regime all finite temperature kernels reduce to the zero temperature Laplace kernel $e^{-\omega\tau}$. The Laplace transformation of the standard default model of Equ. (3.38) gives

$$C_m(\tau) \overset{\tau \to 0}{\approx} m_0 \frac{n!}{\tau^{n+1}}. \tag{3.39}$$

Depending on the expected size of lattice spacing errors, one can then evaluate this relation for small τ, e.g. $\tau = 2$ and one can use $m_0 \approx C(2)2^{n+1}/n!$ to determine the default model parameter m_0 for MEM.

3.3.3 Modified MEM Kernels

Small Frequency Modifications

The standard finite temperature integral kernel is given in Equs. (2.39) and (2.96) and reproduced here for convenience

$$K_T(\tau,\omega) = \frac{\cosh(\omega(\tau - 1/(2T)))}{\sinh(\omega/(2T))}. \tag{3.40}$$

It is a very important integral kernel, as it is the one used e.g. in the reconstruction of transport properties from correlators of the energy momentum tensor. It is also used in the reconstruction of spectral functions of finite temperature mesonic correlators to study the melting of quarkonia in heavy ion collisions.

As [4] pointed out, the divergence of $K_T(\tau,\omega) \approx 2T/\omega$ for small ω leads to numerical problems in the MEM reconstruction for small ω. Their solution was to use a freedom of the defining Equ. (3.31) to redefine the kernel and the spectral function by an arbitrary function $q(\omega)$. This results in the relations

$$C(\tau) = \int_0^\infty \mathrm{d}\omega \bar{K}_T(\tau,\omega)\bar{A}(\omega), \tag{3.41}$$

$$\bar{K}_T(\tau,\omega) = q(\omega)K_T(\tau,\omega), \tag{3.42}$$

$$\bar{A}(\omega) = q(\omega)^{-1}A(\omega). \tag{3.43}$$

[4] chooses

$$q(\omega) = \frac{\omega}{2T} \tag{3.44}$$

to cancel the divergence of the kernel at $\omega = 0$. But every q with that limit for small ω can do that, so that there still remains some freedom. It was noted in [37] that one can use this remaining freedom to normalize the kernel in τ, i.e. to make $\sum_{\tau=0}^{n_t-1} \bar{K}(\tau,\omega) = 1$, by choosing

$$q(\omega) = \tanh\left(\frac{1}{2}\omega\right). \tag{3.45}$$

This choice does not change the kernel for large ω and leads to commuting limits of $n_t \to \infty$ and $\omega \to 0$. This modification allows to reconstruct spectral functions for small frequencies more reliable.

Partial Integration

As stated above, there is always some uncertainty in choosing parameters of MEM like the default model. It is usually taken to represent the dimensionality of the

operator under consideration and is therefore a power law. But in lattice QCD there always is a cutoff at some energy above which there are no states left and the spectral function therefore is zero. It would be desirable to be able to implement this in the reconstruction scheme and in the choice of the default model. On the other hand, to reconstruct transport properties, it would be desirable to have a scheme, where the derivative of the spectral function with respect to frequency is directly reconstructed. This would have the advantage that one could get rid of some systematic uncertainties and background in the reconstruction without the intermediate step of the spectral function itself. In the following, schemes are proposed to achieve all that by partial integration of the defining Equ. (3.40).

Let $f^{(i)}$ denote the i-th derivative of f with respect to ω and correspondingly $f^{(-i)}$ the i-th indefinite integral of f. Then from Equ. (3.40) one gets by partial integration

$$\begin{aligned} C(\tau) =& \int_0^\infty \mathrm{d}\omega K(\tau,\omega)A(\omega) \\ =& K^{(-1)}(\tau,\omega)A(\omega)|_{\omega=0}^{\infty} - \int_0^\infty \mathrm{d}\omega K^{(-1)}(\tau,\omega)A^{(1)}(\omega) \\ =& -\int_0^\infty \mathrm{d}\omega K^{(-1)}(\tau,\omega)A^{(1)}(\omega). \end{aligned} \tag{3.46}$$

In the last step the boundary term vanishes, because $A(\infty) = 0$ due to the lattice cutoff and one can define $K^{(-1)}(\tau,\omega) = \int_0^\omega d\omega' K(\tau,\omega')$ which leads to $K^{(-1)}(\tau,0) = 0$. Now Equ. (3.46) is of the same form as Equ. (3.40) except that one can reconstruct the slope of A directly.

Even though Equ. (3.46) looks just like the original integral equation with different kernel, one important feature is missing: While the spectral function A is positive semi-definite, its derivative $A^{(1)}$ is not. That makes it impossible to use the same definition of the entropy term with A replaced by $A^{(1)}$. Therefore one has to modify the standard MEM and use different techniques to solve this problem. A possible modification could be to integrate $A^{(1)}$ up numerically and then to use the standard entropy term. It might also be sufficient to use the absolute value of $A^{(1)}$ in the entropy term to make it well defined. Alternatively one can shift $A^{(1)}$ before reconstruction by some finite positive value, perform the standard reconstruction and shift it back afterwards.

Analogously one gets

$$\begin{aligned} C(\tau) =& \int_0^\infty \mathrm{d}\omega K(\tau,\omega)A(\omega) \\ =& K(\tau,\omega)A^{(-1)}(\omega)|_{\omega=0}^{\infty} - \int_0^\infty \mathrm{d}\omega K^{(1)}(\tau,\omega)A^{(-1)}(\omega) \\ =& -\int_0^\infty \mathrm{d}\omega K^{(1)}(\tau,\omega)A^{(-1)}(\omega) \end{aligned} \tag{3.47}$$

using $A^{(-1)}(\omega) = \int_0^\omega d\omega' A(\omega')$ and therefore $A^{(-1)}(0) = 0$ and that most kernels and their derivatives fall off exponentially for large ω and $\tau \neq 0$. If A is positive semi-definite, then $A^{(-1)}$ has the same property for $\omega > 0$ and one can use the standard techniques for MEM. Given a measurement of the lattice correlator, the default model for this reconstruction can be reliably determined as it is the constant defined by the total integrated spectral weight of the correlator.

As the reformulated problems reconstruct a completely different function, using these modified kernels could also help to estimate systematic errors in the standard MEM.

3.3.4 Extensions using Multiple Operators

Apart from modifying the integral kernel to improve the sensitivity to specific aspects of the spectral function, it was also proposed to include different operators in the MEM analysis to improve the total sensitivity. If one uses n_O different correlators or operators, in principle on has to solve n_O independent MEM problems, one for each index j of the operator

$$C_j(\tau_i) = \int_0^\infty \mathrm{d}\omega A_j(\omega) K(\tau_i, \omega). \tag{3.48}$$

This is just the result of correlators C_j corresponding to different operators having different spectral representations A_j. This means that the amount of data per degree of freedom in the reconstruction is independent of the number of correlators included.

Extended MEM

A workaround for this problem was proposed recently in reference [51]. In this proposal the fact is used that the correlators not only give additional points in the data vector, but also in the (extended) covariance matrix. For the same lattice gauge configurations different correlators (e.g. for different momenta) are correlated much like the different Euclidean time points in the same correlator. Therefore a correlator of an operator carries information on the error of the correlator of a different operator and its spectral function. Additionally by including these measurements for the correlated error, the error on quantities like the difference of two spectral functions is greatly reduced.

This extension is implemented by considering $C_j(\tau_i)$ as a single vector of the joint index (ij) in the calculation of the χ^2. For the example of two operators this results in the objective function $\frac{1}{2}\chi^2(A_1, A_2) - \alpha_1 S(A_1) - \alpha_2 S(A_2)$ to be minimized with respect to the spectral functions of both correlators A_1 and A_2. α_1 and α_2

n_s	n_t	β	N_{stout}	ρ_{stout}	ξ_g	N_{config}
20	90	5.05	6	0.125	2.7	159

Table 3.1: Parameters of the quenched ensemble used for tests of MEM.

can in principle differ and should be marginalized over separately. In current analyses [51] the coefficients are set to be equal. This can be justified because the considered correlators have been chosen to be the same apart from the projection on different momenta.

Combination with Correlation Matrix Method

The "Extended MEM" of the last section used the correlation of the error of correlators of different operators to get rid of parts of the correlated errors. It is also possible to use the cross-correlation of different operators directly to also reduce the non-correlated parts of the errors and to gain information in addition to the spectral function.

In section 3.2 a method was described, which uses the information of a cross-correlation matrix of different operators to disentangle the contributions of different states from the correlator. This can be used to get the overlap of the operators with the physical states using the generalized eigenvectors and to construct a set of "optimal" operators, which have mainly overlap with one physical state.

The corresponding weights can also be used to construct the correlator corresponding mainly to one of the states. These correlators are proportional to the generalized eigenvalues and they can then be used in separate standard MEM analyses. Afterwards the generalized eigenvectors may be used to reconstruct a single properly normalized spectral function.

This procedure was tested on a small ensemble of quenched anisotropic configurations. The parameters of the data set are given in Tab. 3.1. An example of the potential benefit of the method, some reconstructions are given in Fig. 3.16. The different correlators used for the cross correlation matrix are pseudoscalar correlators with differently smeared sources and sinks. One can clearly see that in this special case the combined CMM and MEM could identify the four contributions at the correct energies which are all seen in CMM alone. This is in clear contrast to the pure MEM case where the reconstructed spectral function wrongly suggests three contributions.

Unfortunately this enhancement of the state resolution of the combined CMM and MEM is strongly dependent on the choice of parameters in the MEM part, e.g. the choice of the default model. This makes it necessary to tune the MEM reconstruction to the point where it is consistent with CMM. But then the re-

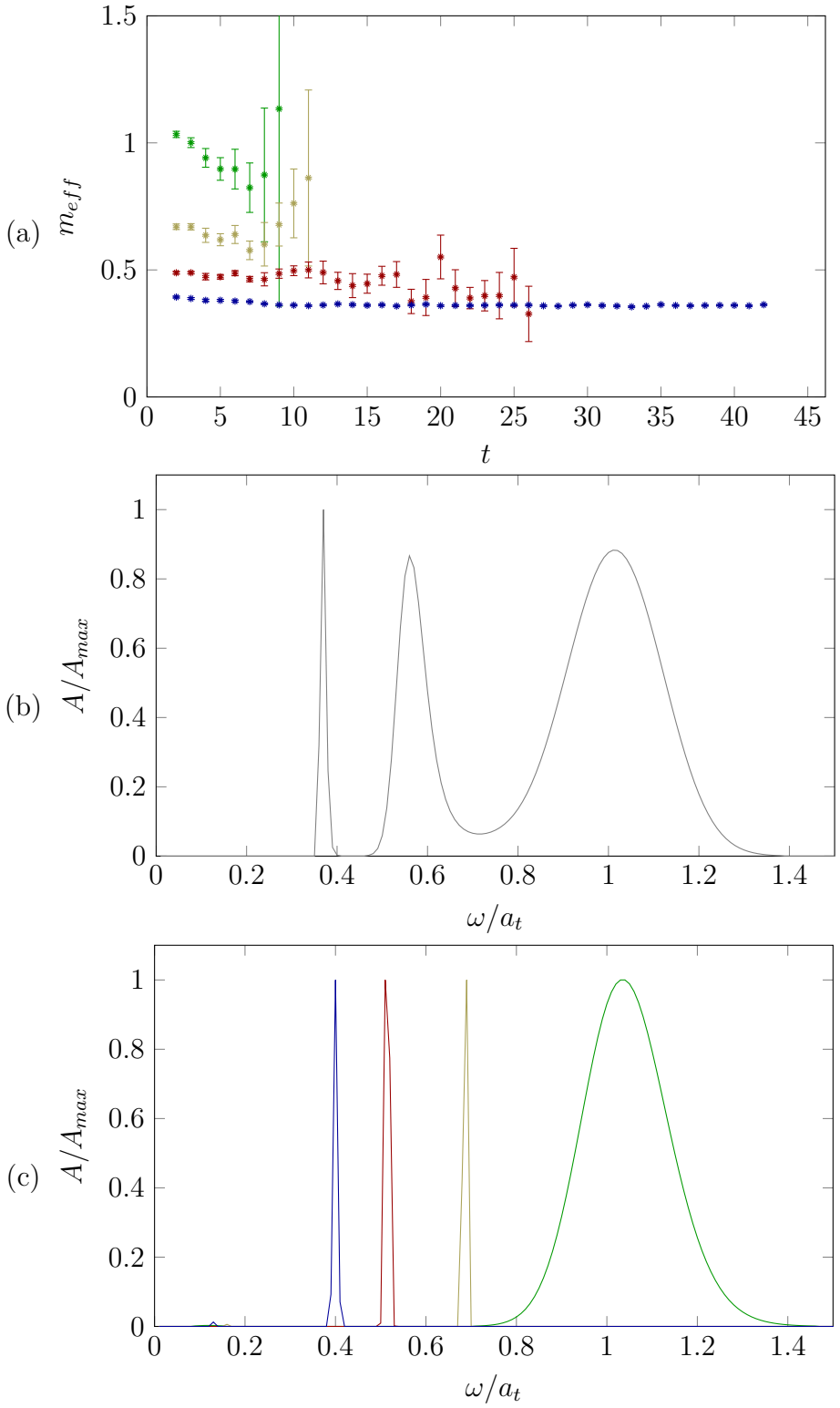

Figure 3.16: Analysis of the pseudoscalar channel of quenched test data (a) with the standard CMM, (b) with the standard MEM, (c) with CMM and MEM combined. The MEM reconstructions are performed at fixed $\alpha = 0.001$ and $m_0 = 1$.

constructed spectral function does not contain much more information than the single CMM analysis.

3.3.5 Summary

This section presented the Maximum Entropy Method, some extensions and proposed a few modifications, which can improve the stability and usability of MEM. Given good data with small errors, MEM can reconstruct some features of the spectral function quite reliably, like the position and area of the ground state peak. It seems also possible to extend MEM to excited states analysis by combining it with the variational method. However, MEM is seen to be strongly dependent on input parameters like the choice of the default model especially when the errors on the correlators are sizeable. Therefore MEM is not used in the remainder of the thesis.

3.4 Spectral Fit

In the sections 3.3 and 3.2 two methods were introduced which can be used to access information on the spectral function which is encoded in Euclidean correlators. Among these methods MEM has a strong link to standard χ^2 fits. There are cases when MEM is not the optimal way to get the spectral function and a plain fit performs better. These cases include the setting where systematic errors in MEM make it difficult to access the specific piece of information, which one is interested in. MEM is also not the best option for the case when one has a strong prior knowledge of the shape of the spectral function. This section will introduce general and specialized χ^2 fits for estimating parameters of the spectral function.

The basis for the discussion is again the spectral representation of an Euclidean correlator in the form of Equ. (2.39), reproduced here for convenience

$$C(\tau) = \int_0^\infty \mathrm{d}\omega K(\tau, \omega) A(\omega), \tag{3.49}$$

with some (finite temperature) integral kernel K.

3.4.1 Least Squares Fit

General

The method of least squares is a prescription to find good estimates for parameters θ of a model given data [71]. The model is generally a parametrization of the spectral function A in Equ. (3.49). The method then consists in minimizing the

sum of squares

$$\chi^2(\theta) = \sum_i \frac{(C_i - C_\theta(\tau_i))^2}{\sigma_i^2}, \tag{3.50}$$

where C_i and σ_i are the measured value and standard error of the correlator at Euclidean time τ_i, and $C_\theta(\tau_i)$ is the prediction of the model for Euclidean time τ_i and the parameters θ.[6] The parameters at the minimum of χ^2 then give the least squares estimates for the model parameters.

For Gaussian distributed data this minimization of the χ^2 is equivalent to the Maximum Likelihood method. Likelihood is defined via the conditional probability $P(D|\theta)$ for measuring the data D if the model with the parameters θ is realized. The data D contains the measured value C_i and standard error σ_i. The likelihood is the conditional probability $P(D|\theta)$ regarded as a function of the model θ

$$L(\theta) := P(D|\theta). \tag{3.51}$$

Under the assumption of a realization of θ, Gaussian distributed data are defined by the conditional probability

$$P(D|\theta) \propto \exp\left(-\frac{1}{2}\sum_i \frac{(C_i - C_\theta(\tau_i))^2}{\sigma_i^2}\right) \tag{3.52}$$

$$= \exp\left(-\frac{1}{2}\chi^2(\theta)\right). \tag{3.53}$$

Then

$$\chi^2(\theta) \propto -2\log(L(\theta)) \tag{3.54}$$

and the minimization of the sum of squares $\chi^2(\theta)$ is equivalent to the maximization of the likelihood $L(\theta)$.

If the number of measurements is sufficiently large, one can always assume a Gaussian distribution of the data due to the central limit theorem. Then the χ^2 for the "correct" model follows a χ^2 distribution with the number of degrees of freedom DOF equal the number of measurements minus the number of fitted parameters. This χ^2 distribution has the number of degrees of freedom as expectation value. Therefore one can use the value at the minimum of χ^2 divided by DOF as a measure of the goodness-of-fit.

[6]Least square fits are of course not restricted to Euclidean correlators. Therefore, what is labelled here as "Euclidean time" τ_i can also be a spatial lattice momentum like in sections 4.2.3 and 4.2.2, some combined data point index construction like in section 4.2.1, or some other completely general data label.

Correlated Fit

As correlators in lattice QCD are usually strongly correlated between different points in Euclidean time, the measured values C_i and their standard error σ_i are not a complete description of the data. One has to incorporate additionally the information in the covariance matrix Σ_{ij} in the fit. This results in one single change: The introduction of the inverse covariance matrix Σ^{-1} in the fit Equ. (3.50)

$$\chi^2(\theta) = \sum_{i,j}(C_i - C_\theta(\tau_i))\Sigma^{-1}_{ij}(C_j - C_\theta(\tau_j)). \tag{3.55}$$

If the covariance matrix is known exactly, this is not a problem at all. But usually this matrix has to be estimated from the data. In some cases the resulting matrix is singular and one cannot invert it, in particular for small data sets. Even if it is non-singular but numerically close to singular, one often cannot invert the matrix to sufficient precision, such that the inversion introduces artefacts. In order not to fall back to uncorrelated fits, several methods have been proposed to circumvent this problem, e.g. modelling of the covariance and smearing of the eigenvalues of the covariance matrix [71, 94]. A new general method to deal with numerically singular covariance matrices is presented in section 3.6.2.

3.4.2 Differentially Smeared Fit

The preceding section contained a quite general presentation of the least squares fitting procedure. This section specializes on the specific problem of the reconstruction of spectral functions from finite temperature lattice data. The picture in this context is the following: One wishes to measure a physical spectral function, which is encoded somehow in the lattice configurations. The only currently known technique to do so, is the indirect measurement via an Euclidean correlator, which is a convolution of the spectral function with the finite temperature kernel, given in Equ. (3.49).

The finite temperature kernel makes it easy to extract some information about the spectral function, like a sharp low energy peak from the ground state. Other features like excited states, continuum contributions, or transport properties are much more difficult to extract. Excited state contributions for example decay much faster than the ground state and are thus hidden under the ground state contribution for large Euclidean times. The transport properties are also difficult to extract, as they are partially "projected away" by the kernel in leading order, as explained in section 2.2.4, and usually have a lower spectral weight than all the possible bound states and continuum contributions.

All these problems come from the fact that there is only one kernel with which one can fold the spectral function for measurement. If there were more kernels with different properties, one could perform several measurements which were sensitive to different parts of the spectral function. Combining the measurements with the different kernels would then yield a more complete and more accurate picture of the properties of the spectral function. The task is now to implement a set of measurements, which behave (approximately) like convoluting the spectral function in the configurations with a set of different kernels. In the following the use of smearing techniques will be motivated as a solution to this problem.

Instead of measuring the same spectral function $A(\omega)$ with different kernels $K_n(\tau,\omega)$, one can also measure a set of spectral functions $A_n(\omega)$ with the same kernel $K(\tau,\omega)$ which are related in some known way and depend on the spectral function of interest $A(\omega)$. A possible way to implement this is to consider spectral functions which are spectrally filtered versions by the action of some weighting functions $A_n(\omega) = w_n(\omega)A(\omega)$. This is of course equivalent to measuring the same spectral function convoluted with different kernels

$$\begin{aligned}\int_0^\infty \mathrm{d}\omega K(\tau,\omega)A_n(\omega) &= \int_0^\infty \mathrm{d}\omega K(\tau,\omega)w_n(\omega)A(\omega)\\ &=: \int_0^\infty \mathrm{d}\omega K_n(\tau,\omega)A(\omega) \end{aligned} \tag{3.56}$$

with the set of kernels $K_n(\tau,\omega) = K(\tau,\omega)w_n(\omega)$. The task is now to find an implementation of the spectral filter for the correlator measurements and the functional form of the weights $w_n(\omega)$. To gain something in the analysis these weights and in particular their dependence on n should be known. Otherwise one brings more degrees of freedom into the analysis than additional data points.

Such filters can be lattice smearing procedures, which act as UV filters: They suppress fluctuations below a certain length scale in position space or equivalently above a certain energy in momentum space. The Wilson flow as a prominent smearing prescription has a special advantage as its regulating properties are in principle accessible analytically. The parameter n then translates to the Wilson flow time or the number of smearing steps performed before measuring a correlator.

As can be seen below, the exact form is not important for some low energy applications at the current level of accuracy of the data; the position of the cutoff is more important and that is known. As an ansatz for the cutoff one can then use any parametrization, as long as one checks the dependence of the result on the functional form of the cutoff in the end. The variation of the result can then be included in the systematic error estimate. Possible choices for the form of the

cutoff include

$$w_\Omega^{\text{step}}(\omega) = \Theta(\Omega - \omega), \tag{3.57}$$

$$w_\Omega^{\tanh,\sigma}(\omega) = \frac{1}{2}\left(1 + \tanh\left(\frac{\Omega - \omega}{\sigma}\right)\right), \tag{3.58}$$

$$w_\Omega^{\text{erf},\sigma}(\omega) = \frac{1}{2}\left(1 + \text{erf}\left(\frac{\Omega - \omega}{\sigma}\right)\right), \tag{3.59}$$

with the Heaviside step function Θ, the error function erf, and the cutoff scale Ω. The parameter σ defines the width of the cutoff.

The introduction of the weighting function and different smearings in the same fit generalizes Equ. (3.49) to

$$C_\Omega(\tau) = \int_0^\infty \mathrm{d}\omega K(\tau,\omega) w_\Omega^{f,\sigma}(\omega) A(\omega), \tag{3.60}$$

where the superscript ^{f} denotes the choice of the functional form of the weight function.

The general concept of using differently smeared correlators together in the same analysis to gain spectral information has been used in the CMM analysis aka Variational Method before. In the way formulated here, one can use it also in a standard χ^2 fit, or in a modified MEM. Both analyses can profit a lot of the additional data points. Anisotropic lattices are also often used to generate more data points for Euclidean correlator measurements. But combining different smearings has some advantages, as it does not require the often expensive tuning of the anisotropy and yields independent information. It can also be combined with anisotropic lattices to get even more data points.

3.5 Reconstructed Correlator

The two preceding sections 3.3 and 3.4 presented methods to reconstruct complete spectral functions from measurements of Euclidean correlators. While both methods are in principle capable of performing such a reconstruction, both also have their drawbacks: MEM is strongly dependent on the choice of parameters like the default model and the fits of spectral functions of course depend on the choice of the ansatz. This section will briefly introduce a method which does not rely on any choices or assumptions to gain information about the change of the spectral function with temperature. But the price for that is that the amount of information gained this way is very limited.

3.5.1 Concept

The concept of a reconstructed correlator was introduced in references [30, 80]. It is based on an analysis of the temperature dependence of the finite temperature spectral representation of Equ. (2.39)

$$C_T(\tau) = \int_0^\infty \mathrm{d}\omega K_T(\tau,\omega) A_T(\omega), \tag{3.61}$$

$$K_T(\tau,\omega) = \frac{\cosh(\omega(\tau-\beta/2))}{\sinh(\omega\beta/2)}. \tag{3.62}$$

With varying temperature, three things change in this equation:

- It is valid in the temperature dependent domain $0 \leq \tau < \beta = 1/T$.
- The integral kernel $K_T(\tau,\omega)$ is dependent on the temperature T.
- The spectral function $A_T(\omega)$ is dependent on the temperature T.

From these three points, only the change of the spectral function contains physical information on the relevant degrees of freedom of the theory in the channel under consideration. The other two points are due to properties of the kernel and mere manifestations of the periodicity of the Euclidean time direction at finite temperature and not physically relevant for Minkovski time physics. These two changes have to be disentangled from the physical change in the spectral function.

This can be done by measuring the Euclidean correlator C_T at two different temperatures T and T'. The correlators cannot be compared directly, as their domains of definition are different, and they contain convolutions of the physical spectral functions with different kernels. By reconstructing the spectral function $A_{T'}$ at the reference temperature and folding it with the kernel K_T at the other temperature, one can define the reconstructed correlator

$$C^{rec}_{T;T'}(\tau) := \int_0^\infty \mathrm{d}\omega K_T(\tau,\omega) A_{T'}(\omega). \tag{3.63}$$

This is directly the correlator at T, as it would look like when the spectral function at T' would be the same as the one at T. All other changes with temperature are absorbed in the reconstruction with the other kernel. Any statistically significant deviation from $C^{rec}_{T;T'}(\tau)$ to $C_T(\tau)$ therefore has to correspond directly to a change in the spectral function, i.e. to a difference in the physics at the two temperatures T and T'.

A convenient observable to look at is for example the difference or the ratio of $C^{rec}_{T;T'}(\tau)$ and $C_T(\tau)$. Deviations from 0 or 1 can then directly be identified with changes in the physics. From the value of the Euclidean time τ at which this

change takes place, one can additionally estimate the energy scale at which the spectral function changes.

It is also possible to disentangle changes in the spectrum at finite frequency from zero mode contributions. As zero modes contribute a constant value in Euclidean time to the correlators, they can be eliminated from the analysis by considering the difference of adjacent points in time or the mid-point subtracted correlators [29, 92].

3.5.2 Sum Rules

Conceptually, the analysis using reconstructed correlators is very clean. But before the correlators can be compared directly, the construction uses a reconstructed spectral function $A_{T'}(\omega)$ at the reference temperature. This can only be done using MEM or fits and reintroduces again the systematic errors known from these methods. Fortunately, the kernel has a property which allows constructing the reconstructed correlator at selected temperatures using Matsubara sums without reference to any method for analytical continuation [32, 35, 70].

Using the identity

$$\frac{\cosh(\omega(\tau - \beta/2)))}{\sinh(\omega\beta/2)} = \sum_{m\in\mathbb{Z}} e^{-\omega|\tau+\beta m|} \tag{3.64}$$

one can derive a useful kernel property by reordering the sum

$$\begin{aligned} K_T(\tau,\omega) &= \sum_{m\in\mathbb{Z}} e^{-\omega|\beta m+\tau|} \\ &= \sum_{n\in\mathbb{Z}}\sum_{j=0}^{r-1} e^{-\omega|\beta(rn+j)+\tau|} \\ &= \sum_{j=0}^{r-1}\sum_{n\in\mathbb{Z}} e^{-\omega|\beta rn+(\tau+j\beta)|} \\ &= \sum_{j=0}^{r-1} K_{T/r}(\tau+j\beta,\omega). \end{aligned} \tag{3.65}$$

This property is valid for $r \in \mathbb{N}$ and useful for the lattice. For example, for two simulations with the same lattice spacing and at the temperatures $T = rT'$, this translates directly into equations for the reconstructed correlator

$$C^{rec}_{T;T/r}(\tau) = \sum_{j=0}^{r-1} C_{T/r}(\tau + j\beta). \tag{3.66}$$

Using this equation one can evaluate reconstructed correlators and all derived observables directly without the detour over analytical continuation, which would

bring in additional systematic uncertainties.

3.5.3 Thermal Moments

The last sections on the reconstructed correlator contained a discussion of a method which gives some information on the spectral content of finite temperature correlation functions. This method, however, did not try to reconstruct a full spectral function like MEM and the fits of the preceding sections. This section follows this line of thought and shortly introduces a method to extract moments of thermal moments of spectral functions [33, 35, 68].

When one expands the Euclidean time dependence of the spectral representation of Equ. (3.61) at the mid-point of the lattice in a Taylor series, one is naturally confronted with some weighted moments of the spectral function

$$C_T^{(n)} = \left.\frac{\mathrm{d}^n C_T}{\mathrm{d}^n(\tau T)}\right|_{\tau T=1/2} \tag{3.67}$$

$$= \int_0^\infty \mathrm{d}\omega \left(\frac{\omega}{T}\right)^n \frac{A_T(\omega)}{\sinh(\omega\beta/2)}. \tag{3.68}$$

By construction, these moments are in principle directly accessible in an Euclidean lattice calculation without reference to any method of analytical continuation of the Euclidean correlator to a spectral function. The derivatives of the correlator can be evaluated numerically, as long as the data at the largest Euclidean time separation is precise enough.

The weights $\omega^n/\sinh(\omega\beta/2)$ have maxima at about $\omega = 2nT$. Therefore one can expect the main sensitivity of the n-th moment at a frequency of about $2nT$. However, for large frequencies the spectral functions are dominated by a continuum contribution which also contributes a power law term $\sim \omega^c$. This shifts the region of main sensitivity in this regime to about $2(n+c)T$. In any case, the lower the moment the more sensitive it is to the infrared properties of the spectral function.

These moments contain again a non-trivial reference to the temperature in the remaining sinh term of the kernel. To be able to compare two spectral functions at different temperatures, one can again construct the reconstructed correlator at temperature T and calculate the thermal moments $C_{T;T'}^{(n)}$ at the temperature T of the spectral function at T'.

As the low moments are determined mainly by the infrared properties of the spectral functions, they are good candidates for a comparison of lattice QCD results with other approaches like holography. In cases where a full continuum limit on the lattice side is not available, the effect of the different regularization of the results at high energies is very prominent for the correlators at large energies,

but not int the infrared. In addition, in cases where the relative normalization of the correlator is different, one can still get normalization invariant numbers which can be compared between different approaches by using ratios of these moments.

3.6 Statistics

This chapter on methods ends with a quite independent general section on aspects of statistics for lattice data analysis. In contrast to the other sections of this chapter, this section will not rely on any direct connection to reconstruction of spectral properties of Euclidean correlators. But of course that is the background of most parts of the thesis as it is of this section.

3.6.1 Resampling Methods

The Jackknife and Bootstrap methods are very powerful tools to estimate the statistical error of observables of any complexity. They belong to the larger class of resampling methods which in essence work in an efficient way on the whole distribution of the data instead of only some moments, like the mean and variance. They map the sample of the distribution of the data on a sample of the distribution of the observable of interest. In principle, any statistically interesting quantities can be estimated from that distribution. The most interesting quantities are of course mean and variance, but the resampling methods are not restricted to these. For the practitioner the most interesting feature is that these methods automatically keep track of the statistical error propagation. This even works without the often necessary assumption of Gaussian distributed data.

Bootstrap

The Bootstrap is a general procedure to estimate the distribution of data and dependent quantities. Let N_C be the number of configurations,

$$D = \{C_c\}_{1 \leq c \leq N_C} \tag{3.69}$$

the set of configurations and O the observable to be measured on the data. In the Bootstrap procedure[7], first a set of N_R replicas

$$D_r = \{C_i\}_{i \in I_r} \tag{3.70}$$

[7]The Bootstrap presented here is the standard "Case Bootstrap".

of the data set is generated by random sampling N_C configurations from the data D with replacement. Every index set in $\{I_r\}_{1\leq r\leq N_R}$ is a set of uniformly distributed integer random numbers between 1 and N_C.

On these replicas the observable O can be measured just like on the original data set, which results in a set $\{O_r = O(D_r)\}_{1\leq r\leq N_R}$ of the measurements of the observable, which constitute a sample of the distribution of the observable. On this sample one can measure the mean, variance, and other statistical quantities in the standard way

$$\langle O\rangle = \frac{1}{N_R}\sum_{r=1}^{N_R} O_r \tag{3.71}$$

$$\sigma^2_{\langle O\rangle} = \frac{1}{N_R-1}\sum_{r=1}^{N_R}(O_r - \langle O\rangle)^2. \tag{3.72}$$

For the two observables "mean" and "variance" and data, which are just plain real numbers, this looks like

$$\langle C\rangle = \frac{1}{N_R}\sum_{r=1}^{N_R}\langle C\rangle_r = \frac{1}{N_R N_C}\sum_{r=1}^{N_R}\sum_{i\in I_r} C_i \tag{3.73}$$

$$\sigma^2_{\langle C\rangle} = \frac{1}{N_R-1}\sum_{r=1}^{N_R}\left(\langle C\rangle_r - \langle C\rangle\right)^2 \tag{3.74}$$

$$\langle\sigma^2_C\rangle = \frac{1}{N_R}\sum_{r=1}^{N_R}(\sigma^2_C)_r = \frac{1}{N_R}\sum_{r=1}^{N_R}\frac{1}{N_C-1}\sum_{i\in I_r}\left(C_i - \langle C\rangle_r\right)^2 \tag{3.75}$$

$$\sigma^2_{\sigma^2_C} = \frac{1}{N_R-1}\sum_{r=1}^{N_R}\left((\sigma^2_C)_r - \langle\sigma^2_C\rangle\right)^2. \tag{3.76}$$

Note that the observable O can be any complicated function of the data, e.g. complex fitting algorithms. But the method to determine the statistically interesting quantities is completely independent of that.

The Bootstrap implemented as above assumes independent i.e. uncorrelated configurations. But an adaptation for correlated configurations is readily achieved by blocking the data into N_B contiguous blocks

$$B_b = \{C_c\}_{c_b\leq c<c_{b+1}} \tag{3.77}$$

with the block index $1 \leq b \leq N_B$, the block boundary indices c_b, and the number of configurations $N_{B,b}$ in a block b. To ensure that the correlation between the configurations is taken into account, the blocks have to be larger than the correlation length λ. For blocking to effectively get rid of correlations, the data blocks in principle do not need to be equally sized. However, usually equally sized data

blocks are used, up to rounding errors when the number of configurations N_C is not an integer multiple of the number of blocks N_B. This changes the generation of replicas of the data (Equ. (3.70)) such that complete blocks of data are chosen randomly instead of single configurations.

While this procedure is very general and comfortable, it still has some drawbacks. Due to the random generation of replicas of the data, the resulting estimates are different for every analysis (within the error), even for the same data. This effect can be minimized by increasing the number of replicas N_R. But the computing time necessary for the data analysis also scales with N_R, which makes the method expensive especially for complex observables O.

Jackknife

The Jackknife does not have this problem of varying analysis results and is otherwise similar to the Bootstrap method. A difference is the generation of replicas. In the Jackknife this is done by defining the replicas as the data without one of the configurations

$$D_r = \{C_c\}_{1\leq c\leq N_C, c\neq r} = \{C_c\}_{i\in I_r}, \tag{3.78}$$

which defines new index sets I_r of $N_I = N_C - 1$ elements each. This procedure is deterministic and fixes the number of replicas to be equal to the number of configurations $N_R = N_C$. This also limits the computational cost, as the observable has to be evaluated only N_C times (and no random numbers have to be drawn). This procedure yields equivalent statistics to drawing $N_C - 1$ times without replacement instead of drawing N_C times with replacement in the Bootstrap method. This leads to a strong correlation between the replicas and changes the resulting distributions of the observables such that the calculations of most interesting quantities (apart from the mean) have to be modified

$$\langle O\rangle = \frac{1}{N_R}\sum_{r=1}^{N_R} O_r \tag{3.79}$$

$$\sigma^2_{\langle O\rangle} = \frac{N_R - 1}{N_R}\sum_{r=1}^{N_R}(O_r - \langle O\rangle)^2. \tag{3.80}$$

Again, for the two observables "mean" and "variance" and configurations which

are just plain real numbers this looks like

$$\langle C\rangle = \frac{1}{N_R}\sum_{r=1}^{N_R}\langle C\rangle_r = \frac{1}{N_R N_I}\sum_{r=1}^{N_R}\sum_{i\in I_r} C_i = \frac{1}{N_C}\sum_{i=1}^{N_C} C_i \tag{3.81}$$

$$\sigma^2_{\langle C\rangle} = \frac{N_R-1}{N_R}\sum_{r=1}^{N_R}\left(\langle C\rangle_r - \langle C\rangle\right)^2 \tag{3.82}$$

$$\langle\sigma^2_C\rangle = \frac{1}{N_R}\sum_{r=1}^{N_R}(\sigma^2_C)_r = \frac{1}{N_R}\sum_{r=1}^{N_R}\frac{1}{N_I-1}\sum_{i\in I_r}\left(C_i - \langle C\rangle_r\right)^2 \tag{3.83}$$

$$\sigma^2_{\sigma^2_C} = \frac{N_R-1}{N_R}\sum_{r=1}^{N_R}\left((\sigma^2_C)_r - \langle\sigma^2_C\rangle\right)^2. \tag{3.84}$$

To further limit the computational cost and to account for correlations, one can again apply the same data blocking technique as the one introduced for the Bootstrap. Then Equ. (3.78) for the generation of replicas is adjusted such that only the number of blocks $N_B = N_R$ replicas are generated with each omitting a complete block of data.

3.6.2 Decorrelated Data Analysis

In section 3.4 the problem of ill-conditioned covariance matrices in data fitting was mentioned. Here a new method is proposed, which can eliminate the correlations from the data by a combination of data blocking and resampling.

To be able to make statements about correlations, one has to introduce a set of observables $\{O_i\}_{1\le i\le N_O}$ instead of a single one like in the last sections. In the lattice QCD case, the different observables can be an Euclidean correlator measured at different points in Euclidean time. N_B blocks of data are defined by their index sets I_b with $N_{B,b}$ elements each.

There are different types of correlations. In general, the C_c are not independent from each other, e.g. if they originate from a Markov chain. These correlations can be taken into account straightforwardly by blocking the data as described above. In general, also the $\{O_i(C_c)\}_{1\le i\le N_O}$ for a single configuration C_c are not independent, e.g. if they contain Euclidean correlators evaluated at neighbouring values of Euclidean time. Usually this correlation is accounted for by considering the covariance matrix of the data

$$\Sigma_{ij} = \frac{1}{N_C-1}\sum_{c=1}^{N_C}(O_i(C_c) - \langle O_i\rangle)(O_j(C_c) - \langle O_j\rangle). \tag{3.85}$$

The diagonal elements of the covariance matrix are the variances $\Sigma_{ii} = \sigma_i^2$. The covariance matrix often has to be inverted, e.g. to perform a correlated χ^2 fit. For a lot of data sets this is a problem, as the covariance matrix can be close to

singular and only be inverted numerically for virtually unachievable amounts of statistics.

One can, however, define again a method of data blocking to get rid of the correlations between the operators. This is done by modifying the procedure in which the inverted covariance is usually used. The problem with the covariance matrix arises for the set of averages

$$\{\langle O_i(C_c)\rangle_{I_n}\}_{1\leq i\leq N_O} \tag{3.86}$$

for a single block n, which are correlated. The x_I denote x evaluated on the configurations specified with the index set I. Instead, one may also choose the number of blocks to equal the number of operators $N_B = N_O$ and consider

$$\{\langle O_i(C_c)\rangle_{I_i}\}_{1\leq i\leq N_O}, \tag{3.87}$$

which are uncorrelated, as they are calculated from different sets of data. The covariance matrix for this alternative data set is therefore diagonal by construction and its inverse is straightforward. The diagonal has entries given by the variances

$$\Sigma^A_{ij} = \delta_{ij}\frac{1}{N_{B_i}-1}\sum_{c\in I_i}(O_i(C_c) - \langle O_i\rangle_{I_i})^2 \tag{3.88}$$

$$=: \delta_{ij}\sigma^2_{i,I_i}. \tag{3.89}$$

For quantities evaluated on all configurations the index set is omitted.

Additionally, for large N_C it is possible to choose the block sizes in such a way that all the relative errors are equal[8]

$$N_{B,i} = N_C\frac{\sigma_i^2/\langle O_i\rangle^2}{\sum_{j=1}^{N_O}\sigma_j^2/\langle O_j\rangle^2}. \tag{3.90}$$

This can be seen by using the scaling of the error with the square root of the size of the statistic

$$\frac{\sigma^2_{i,I_i}}{\langle O_i\rangle^2} = \frac{N_C}{N_{B,i}}\frac{\sigma_i^2}{\langle O_i\rangle^2} = \frac{N_C\sum_{j=1}^{N_O}\sigma_j^2/\langle O_j\rangle^2}{N_C\sigma_i^2/\langle O_i\rangle^2}\frac{\sigma_i^2}{\langle O_i\rangle^2} = \sum_{j=1}^{N_O}\frac{\sigma_j^2}{\langle O_i\rangle^2}. \tag{3.91}$$

This also makes it explicit that the price for having a trivial covariance matrix is to have less data in a single decorrelated analysis, e.g. a single fit. The choice to make all errors equal, maximizes the amount of data used in the "hard" observables

[8]It is also possible to make the absolute errors equal. This might be of limited use, however, as the observables can be measured in different units and a sum over their variances is necessary.

with large error.

To use all data in the analysis, one has to repeat the proposed procedure for different distributions of the data on the observables or data blocks. In the spirit of the Jackknife analysis one can do that by selecting a number of starting points for the definition of the data blocks (i.e. the configuration $c = 1$ in the cyclic ordered set $\{C_c\}$). The number of repetitions may be taken on the order of the number of blocks. The results of the different repetitions have to be averaged to give the final result. To get the statistical error of this result, the complete prescription can be done inside a Bootstrap or Jackknife analysis.

Chapter 4

Numerical Results

4.1 Data

This section gives an overview of the simulation data used for most of the analyses in this chapter. It will present an assessment of discretization errors and finite volume errors, tests of the anisotropic renormalization prescription of the energy momentum tensor given in 2.2.1, and some implementation details on the correlator measurement.

4.1.1 Setup

This work assesses the possibility of studying transport coefficients with techniques available in dynamical simulations. For that it is better to work with pure $SU(3)$ gauge theory, i.e. in the quenched setup, as more configurations can be generated to see what size of statistics is sufficient for the more expensive dynamical case. More precisely, a Symanzik improved gauge action with $\mathcal{O}(a^2)$ discretization errors is used [60, 88]. The traceless energy momentum tensor $\Theta_{\mu\nu}$ is built directly from the clover lattice field strength tensor $F_{\mu\nu}$ and has also $\mathcal{O}(a^2)$ discretization errors. In this effort, configurations at temperatures ranging from 0.75 T_c to 4.0 T_c were generated for $8 \leq n_t \leq 32$ and aspect ratios from 1 to 8. An update sweep consists of one heatbath and four overrelaxation steps.

In the beginning of this work, anisotropic lattices of anisotropy up to $\xi = 4$ were also used. It turned out, however, that they do not give much additional information on the low frequency part of the spectral functions compared to isotropic ones, but are considerably more costly to work with, due to the need to tune the anisotropy and due to the complications related to renormalization which arise in the analysis. Therefore, the simulation time was spent on simulating with different aspect ratios to get additional points in momentum rather than in Euclidean time. Nevertheless, to test the anisotropic renormalization procedure of section 2.2.1, quenched anisotropic data is used.

The simulations were performed on the QPACE machine [11] on the Wuppertal site with a modified cellsu3 code[1].

4.1.2 Momentum Space Correlators from the Lattice

Usually in full dynamic lattice QCD simulations, the generated gauge configurations are directly written to disk. Then every observable can be measured on the configurations offline, including those which were not implemented or even known at the time of the simulation. This maximizes the flexibility in analyzing the data and is very reasonable for dynamical simulations, where the generation of independent configurations is very expensive. The offline measurement then has to deal with the whole configurations. Streaming them through memory for evaluation of some possibly simple observables is time consuming and of course occupies a large amount of disk space.

In quenched simulations the generation of configurations is quite inexpensive. Therefore the configurations are not saved to disk. Instead, only the observables of interest like some scalars or two point functions are saved. However, this makes it impossible to measure any observable other than those thought of while starting the simulation.

During the work on this thesis, it happened a few times that after running simulations the range of interesting observables was increased and the simulations had to be re-run. Therefore a compromise between saving whole configurations and saving only the final observables was found. This section motivates the data layout used for most of the simulations in this thesis.

Data Layout

This thesis mostly deals with gluonic observables, like scalars and two point correlators in Euclidean time at non-vanishing but small spatial momentum. Mostly, they can be constructed from gauge invariant combinations of the field strength tensor $F_{\mu\nu}$, like e.g. the energy momentum tensor. For all considered scalars to be measured offline, it is sufficient to save all the $\mathrm{tr}(F_{\mu\nu}F_{\rho\sigma})$ summed over all space-time points of the lattice for all $6 \cdot (6+1)/2 = 21$ non-trivial combinations of (μ, ν, σ, ρ). For two point correlators to be generated offline, one also needs these sums carried out over one time slice only. This is sufficient for n-point correlators in Euclidean time with $n > 2$ as well.

To also get different momenta, the 21 traces projected on definite spatial momentum have to be saved separately. Here the 2 smallest non-zero momenta along

[1]The author thanks Szabolcs Borsányi for the efficient pure $SU(3)$ implementation, which was the starting point for this work.

the three spatial lattice axes were chosen, because infrared properties of the theory (i.e. transport coefficients) were targeted. Storing complex numbers gives an additional factor of 2. This gives altogether $2 \cdot 21 \cdot (3 \cdot 2 + 1) \cdot n_t$ floating point numbers to be stored per configuration, instead of $12 \cdot n_s^3 n_t$ for a full configuration (factor 12 for storing two complex columns of a SU(3) matrix). This trades the volume scaling of the amount of data for a constant. For the lattice sizes considered, this saves 3-4 orders of magnitude in storage requirements and time in analysis. An additional speedup comes from the fact that a part of the analysis work (taking the SU(3) traces and reduction over the time slices) is already done during the simulation. This retains a lot of the flexibility in the analysis as 21^n different n-point correlators in time and also correlators in momentum space for small momenta can still be constructed from this data.

In the main part of the simulations, a rather coarse implementation of the Wilson flow is used: A sequence of finite stout smearing steps. To be able to investigate the effect of smearing as an approximation of the Wilson flow on the results, the amount of data increases by an order of magnitude by having to save the data set for each value of the smearing. But this factor is independent of the data layout. Still the reduction in memory consumption is enough to make the analysis possible on a desktop PC.

Euclidean Correlator of Two Operators

The simplest correlators are

$$C_{O_1,O_2}(x,y) = \langle O_1(x) O_2(y) \rangle \,, \tag{4.1}$$

where $\langle . \rangle$ denotes the average over configurations.

Due to translational invariance

$$\begin{aligned} C_{O_1,O_2}(x,y) &= C_{O_1,O_2}(0, y-x) && (4.2)\\ &=: C_{O_1,O_2}(y-x) && (4.3)\\ C_{O_1,O_2}(y) &= \langle O_1(0) O_2(y) \rangle && (4.4)\\ &= \frac{1}{V_4} \sum_x \langle O_1(x) O_2(y+x) \rangle && (4.5) \end{aligned}$$

with the 4-volume V_4.

One can project the correlator on an Euclidean 4-momentum p by

$$\tilde{C}_{O_1,O_2}(p) = \frac{1}{V_4}\sum_y e^{ipy} C_{O_1,O_2}(y) \tag{4.6}$$

$$= \frac{1}{V_4}\sum_y e^{ipy}\frac{1}{V_4}\sum_x \langle O_1(x)O_2(y+x)\rangle \tag{4.7}$$

$$= \frac{1}{V_4}\sum_x \frac{1}{V_4}\sum_y e^{ip(y+x)}e^{-ipx}\langle O_1(x)O_2(y+x)\rangle \tag{4.8}$$

$$= \left\langle \frac{1}{V_4}\sum_x e^{-ipx}O_1(x)\frac{1}{V_4}\sum_y e^{ip(y+x)}O_2(y+x)\right\rangle \tag{4.9}$$

$$= \left\langle \tilde{O}_1(-p)\tilde{O}_2(p)\right\rangle \tag{4.10}$$

with

$$\tilde{O}(p) := \frac{1}{V_4}\sum_x e^{ipx}O(x). \tag{4.11}$$

For zero Euclidean frequency $p_0 = 0$

$$\tilde{O}(0,\vec{p}) = \frac{1}{n_t}\sum_{x_0}\frac{1}{V_3}\sum_{\vec{x}} e^{i\vec{p}\vec{x}}O(x) \tag{4.12}$$

$$= \frac{1}{n_t}\sum_{x_0}\hat{O}(x_0,\vec{p}) \tag{4.13}$$

with the number of time slices in temporal direction n_t, the 3-volume V_3 and

$$\hat{O}(x_0,\vec{p}) := \frac{1}{V_3}\sum_{\vec{x}} e^{i\vec{p}\vec{x}}O(x). \tag{4.14}$$

For the correlator this gives

$$\tilde{C}_{O_1,O_2}(0,\vec{p}) = \left\langle \tilde{O}_1(-p)\tilde{O}_2(p)\right\rangle \tag{4.15}$$

$$= \left\langle \frac{1}{n_t}\sum_{x_0}\hat{O}_1(x_0,-\vec{p})\sum_{y_0}\frac{1}{n_t}\hat{O}_2(y_0,\vec{p})\right\rangle. \tag{4.16}$$

As written in the beginning of this section, the real and the imaginary part of the $\hat{O}(x_0,\vec{p})$ are computed and saved for every combination (μ,ν,ρ,σ) in $O(x) = \mathrm{tr}(F_{\mu\nu}(x)F_{\rho\sigma}(x))$ and $|\vec{p}| = n\frac{2\pi}{an_s}$ with $n \in \{0,1,2\}$.

Euclidean Correlator of Three Operators

The second simplest correlators are

$$C_{O_1,O_2,O_3}(x,y,z) = \langle O_1(x)O_2(y)O_3(z)\rangle\,. \tag{4.17}$$

Again due to translational invariance

$$C_{O_1,O_2,O_3}(x,y,z) = C_{O_1,O_2,O_3}(0,y-x,z-x) \tag{4.18}$$
$$:= C_{O_1,O_2,O_3}(y-x,z-x) \tag{4.19}$$
$$C_{O_1,O_2,O_3}(y,z) = \langle O_1(0)O_2(y)O_3(z)\rangle \tag{4.20}$$
$$= \frac{1}{V_4}\sum_x \langle O_1(x)O_2(y+x)O_3(z+x)\rangle\,. \tag{4.21}$$

Now one can project the correlator on two Euclidean 4-momenta p and q by

$$\tilde{C}_{O_1,O_2,O_3}(p,q) = \frac{1}{V_4}\sum_y e^{ipy}\frac{1}{V_4}\sum_z e^{iqz} C_{O_1,O_2,O_3}(y,z) \tag{4.22}$$
$$= \frac{1}{V_4}\sum_y e^{ipy}\frac{1}{V_4}\sum_z e^{iqz}\frac{1}{V_4}\sum_x \langle O_1(x)O_2(y+x)O_3(z+x)\rangle \tag{4.23}$$
$$= \frac{1}{V_4}\sum_x \frac{1}{V_4}\sum_y e^{-ipx}e^{ip(y+x)}\frac{1}{V_4}\sum_z e^{-iqx}e^{iq(z+x)}\,\langle O_1(x)O_2(y+x)O_3(z+x)\rangle \tag{4.24}$$
$$= \left\langle \frac{1}{V_4}\sum_x e^{-i(p+q)x} O_1(x)\frac{1}{V_4}\sum_y e^{ip(y+x)}O_2(y+x)\frac{1}{V_4}\sum_z e^{iq(z+x)}O_3(z+x)\right\rangle \tag{4.25}$$
$$= \left\langle \tilde{O}_1(-(p+q))\tilde{O}_2(p)\tilde{O}_3(q)\right\rangle. \tag{4.26}$$

For the correlator at zero Euclidean frequency this gives

$$\tilde{C}_{O_1,O_2,O_3}(0,\vec{p},0,\vec{q}) = \left\langle \tilde{O}_1(-(p+q))\tilde{O}_2(p)\tilde{O}_3(q)\right\rangle \tag{4.27}$$
$$= \left\langle \frac{1}{n_t}\sum_{x_0}\hat{O}_1(x_0,-(\vec{p}+\vec{q}))\sum_{y_0}\frac{1}{n_t}\hat{O}_2(y_0,\vec{p})\sum_{z_0}\frac{1}{n_t}\hat{O}_3(z_0,\vec{q})\right\rangle. \tag{4.28}$$

The maximum $|\vec{p}+\vec{q}|\frac{an_s}{2\pi}$ in the data set is 2. Therefore the calculable $\vec{p}$,$\vec{q}$ combinations are limited and their full list is given in Tab. 4.1. This gives a total of 7 independent combinations when all momenta are parallel.

4.1.3 Anisotropic Renormalization

In the first part of this section, the applicability of the anisotropic renormalization procedure described in section 2.2.1 is demonstrated. For this, two simulations were done with setups corresponding to anisotropies of 1.0 and 4.0. The parameters of the simulation are given in Tab. 4.2. They correspond to a fixed physical lattice extent in temporal direction of $T = 1.5\ T_c$ and a physical aspect ratio of 2. N_{sep} is the number of update sweeps, which separate the configurations, and was

$p\frac{an_s}{2\pi}$	$q\frac{an_s}{2\pi}$	$\lvert\vec{p}+\vec{q}\rvert\frac{an_s}{2\pi}$
0	0	0
0	1	1
0	2	2
1	1	2
1	-1	0
1	-2	1
2	-2	0

Table 4.1: Full list of currently calculable $\vec{p}$,$\vec{q}$ combinations.

equal to 1 for these runs. The applied smearing is equivalent in physical units, implying that the number of smearing steps has to be much larger in the anisotropic case, to satisfy the condition for proper stout smearing $\xi^2\rho_{Stout} \leq 0.125$. For larger smearings or Wilson flow times this makes working with anisotropic lattices much more expensive.

n_t	n_s	β	ξ_0	N_{Stout}	ρ_{Stout}	ξ_{Stout}	N_{conf}	N_{sep}	$N_{streams}$
8	16	4.81166	1.0	1	0.0791572	1.0	$8.7 \cdot 10^5$	1	5
32	16	5.06027	3.59877	11	0.00719611	4.0	$2.9 \cdot 10^6$	1	23

Table 4.2: Parameters of the simulation to demonstrate the anisotropic renormalization strategy.

Fig. 4.1 shows as an example a renormalized anisotropic correlator of the shear channel in comparison to the isotropic correlator. The "renormalization scale" is at an Euclidean time $T\tau = 0.25$. The renormalization condition is that at that point the different multiplicatively renormalizing parts of the correlators agree between the isotropic and the anisotropic lattice. The three resulting equations for the two relevant renormalization factors were solved by minimization of the quadratic error. The resulting factors are $Z^{BB_1} = 0.937(2)$ and $Z^{EE_1} = 13.19(6)$, their tree-level expectations are $Z^{BB_1}_{t.l.} = 1$ and $Z^{EE_1}_{t.l.} = \xi^2 = 16$.

One can see a good overall agreement between the anisotropic and the isotropic correlator. The agreement is worse for Euclidean time separations which are not close to the renormalization scale. This difference is expected to vanish in the continuum limit. For finite lattice spacings, one should have this effect in mind and choose the renormalization scale as the scale of the observable one is interested in and account for the variation of the renormalization scale when giving the systematic error of the final result.

For the reasons discussed above and due to the additional systematic error introduced by the choice of renormalization scale, the remainder of this work will only deal with isotropic pure $SU(3)$ simulations.

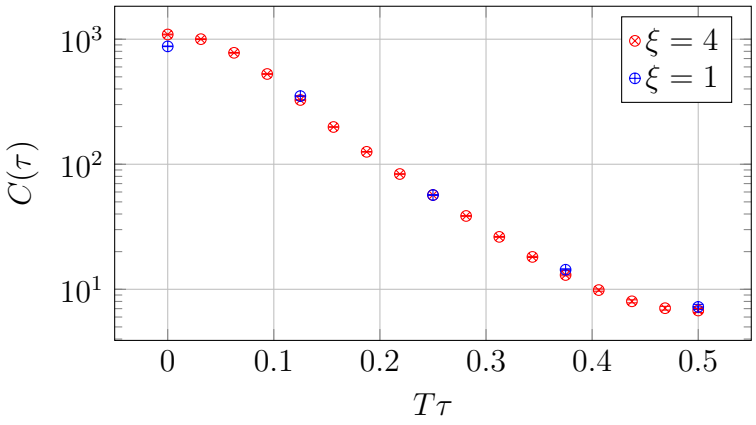

Figure 4.1: $C(\tau) = \frac{1}{T^5} \int \mathrm{d}\vec{x} \langle \Theta_{12}(0,0)\Theta_{12}(\tau,\vec{x})\rangle$, renormalized and built from diagonal components (compare Equ. (2.78)). Errors are statistical Jackknife errors.

4.1.4 Discretization Errors and Scaling

The purpose of this section is to estimate the effect of the lattice spacing on the relevant correlators. Additionally, its purpose is to estimate what lattice spacing is sufficient to describe the infrared physics of the transport coefficients. This largest allowed lattice spacing determines primarily the computational resources required, which are the main limiting factor for dynamical studies.

For our simulations at different lattice spacings, the smearing radius r_{smear} or equivalently the flow time t are held constant to see the effect of discretization errors on a specific scale of the theory. The parameters of the simulation are given in section 4.3. The value of N_{Stout} cited there is the maximum value used and corresponds to a smearing radius of $Tr_{smear} = 0.5$. The smallest radius corresponds to one smearing step on the coarsest lattice and is $Tr_{smear} = 0.11$.

Fig. 4.2 gives the dependence of a shear channel correlator on lattice spacing for some selected values of the flow time, e.g. for $T = 1.5\ T_c$. The plots for different correlators and for different temperatures exhibit the same features: For small smearing radii the discretization errors are sizeable and the statistical errors are large for large separations in Euclidean time. For medium radii the values for all the different smearing radii lie essentially on the same curve and the discretization errors are negligible. The statistical error has been strongly reduced. For the largest considered smearing radius, the errors still decrease substantially for large Euclidean time separations below T_c. Above T_c the data for the different lattice spacings disagree more, probably because the smearing radius has reached the temporal extent of the lattice. The magnitude of the correlator at small Euclidean distances decreased by orders of magnitude with increasing smearing, just as expected from an increasing loss of the high energy parts of the spectrum in the spectral function.

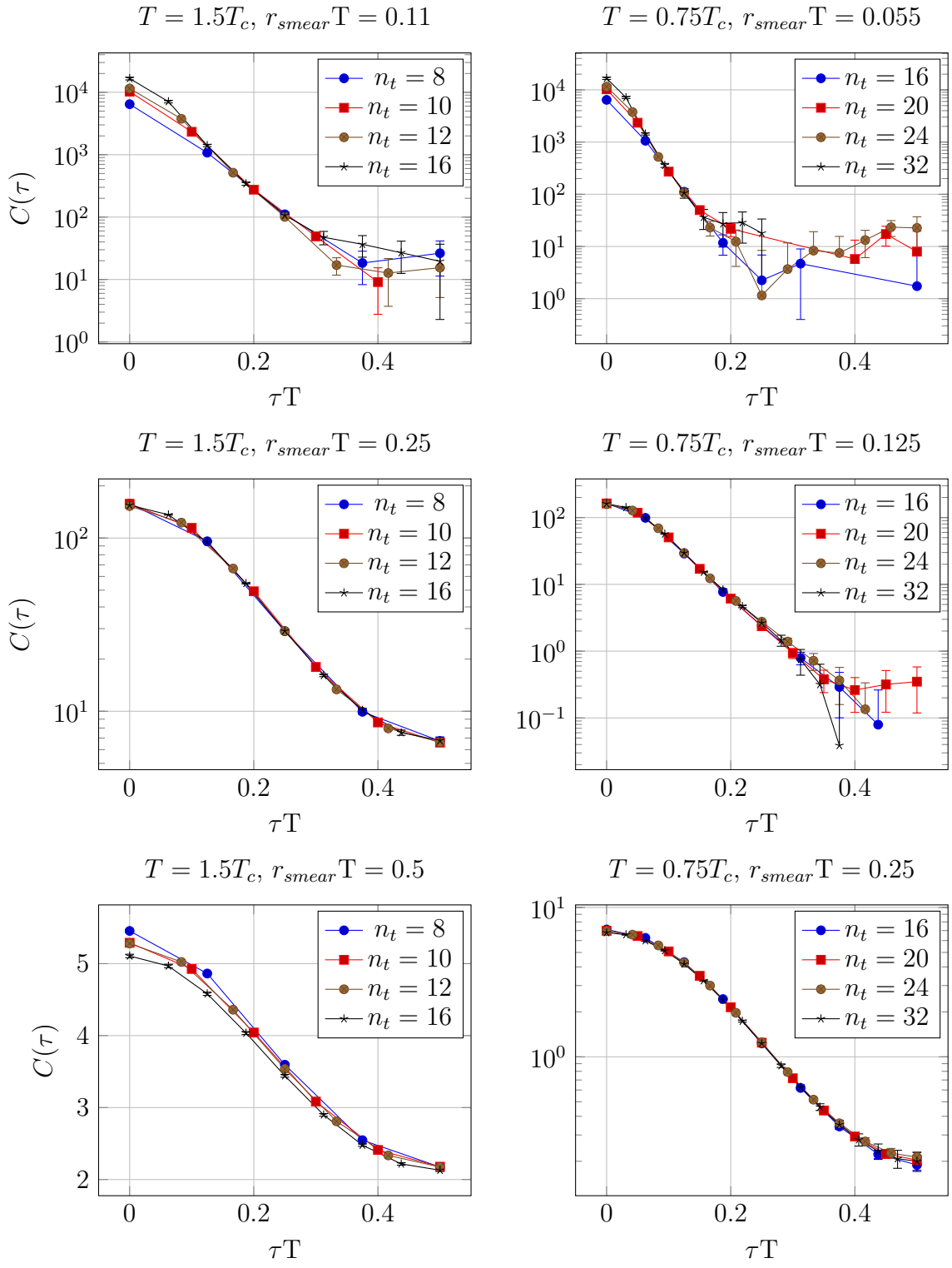

Figure 4.2: $C(\tau) = \frac{1}{T^5} \int \mathrm{d}\vec{x} \langle \Theta_{12}(0,0)\Theta_{12}(\tau,\vec{x})\rangle$ scaling behaviour. Renormalized and built from diagonal components (compare Equ. (2.78)). The left column corresponds to $T = 1.5T_c$, the right one to $T = 0.75T_c$ with the same smearing in physical units. Errors are statistical Jackknife errors.

T/T_c	n_t	n_s	β	N_{Stout}	ρ_{Stout}	N_{conf}	N_{sep}	$N_{streams}$
0.75	16	16	4.81166	25	0.0837365	$5.4 \cdot 10^4$	16	2
0.75	20	20	4.98659	36	0.0872255	$4.8 \cdot 10^4$	24	4
0.75	24	24	5.13241	49	0.0942036	$3.7 \cdot 10^4$	32	8
0.75	32	32	5.36624	72	0.111649	$1.6 \cdot 10^4$	48	22
1.5	8	16	4.81166	25	0.0837365	$4.8 \cdot 10^4$	8	6
1.5	10	20	4.98659	36	0.0872255	$1.1 \cdot 10^5$	12	3
1.5	12	24	5.13241	49	0.0942036	$1.4 \cdot 10^5$	16	6
1.5	16	32	5.36624	72	0.111649	$6.2 \cdot 10^4$	24	18
3.0	8	16	5.36624	25	0.0837365	$5.9 \cdot 10^4$	8	1
3.0	10	20	5.54986	36	0.0872255	$4.3 \cdot 10^4$	12	2
3.0	12	24	5.70092	49	0.0942036	$5.4 \cdot 10^4$	16	4
3.0	16	32	5.94063	72	0.111649	$4.0 \cdot 10^4$	24	25
4.5	8	16	5.70092	25	0.0837365	$7.6 \cdot 10^4$	8	1
4.5	10	20	5.88676	36	0.0872255	$4.5 \cdot 10^4$	12	3
4.5	12	24	6.03933	49	0.0942036	$3.7 \cdot 10^4$	16	2
4.5	16	32	6.29871	72	0.111649	$3.8 \cdot 10^4$	24	19

Table 4.3: Parameters of the simulations used to estimate discretization errors.

As these simulations indeed pointed to a rather complete elimination of the discretization errors by the use of a discretized Wilson flow, the following sections will concentrate on the coarsest lattice spacing.

4.1.5 Assessing Finite Volume Errors

This section is devoted to the study of finite volume errors in the correlators, which might be quite substantial for the aspect ratios of 2 considered in section 4.1.4. To get small momenta, much larger volumes are needed, anyway. These small momenta are necessary to make the ansatz for the spectral function valid, which is motivated by hydrodynamics.

The parameters of this simulation run are given in Tab. 4.4. The resulting three aspect ratios are $2, 6, 8$ corresponding to an increase in the volume by a factor of 27 and 64 compared to the smallest volume.

T/T_c	n_t	n_s	β	N_{Stout}	ρ_{Stout}	N_{conf}	N_{sep}	$N_{streams}$
1.5	8	16	4.81166	25	0.0837365	$4.8 \cdot 10^4$	8	6
1.5	8	48	4.81166	25	0.0837365	$1.8 \cdot 10^4$	32	9
1.5	8	64	4.81166	25	0.0837365	$7.7 \cdot 10^3$	32	9

Table 4.4: Parameters of the simulations used to estimate finite volume effects.

Fig. 4.3 again shows exemplarily a shear channel correlator for a value of the smearing radius, for which no discretization errors were observe in section 4.1.4. The results for the larger three volumes show no clear trend: For the smallest and

the largest volume the results are consistent, while those for the medium large volume are slightly off. However, as the behaviour is not monotonic and as even for large Euclidean distances one observes only a two sigma effect, it is probably caused by the limited statistics. Another possible source for this slight discrepancy is that there is a large subtraction due to the finite part of the expectation value of the correlator from the finite value for $\langle\Theta_{11}\rangle$. This problem does not exist for the finite momentum data.

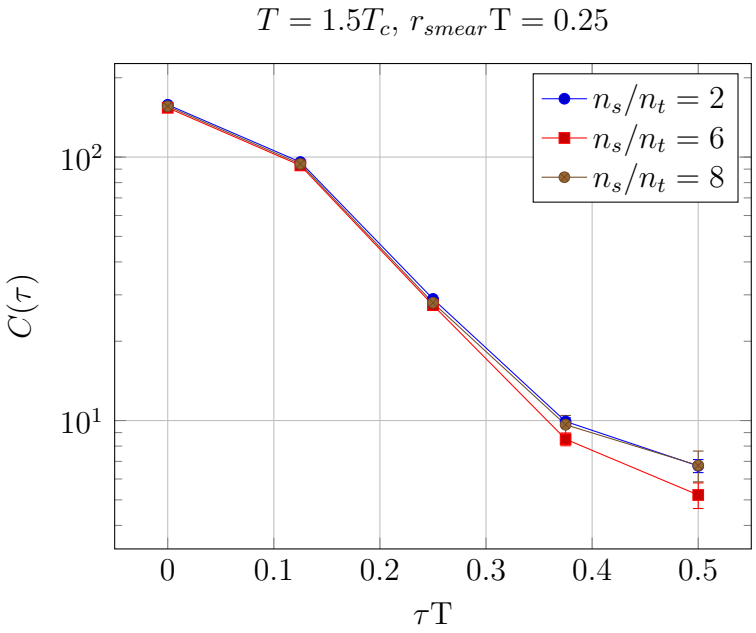

Figure 4.3: $C(\tau) = \frac{1}{T^5}\int \mathrm{d}\vec{x}\langle\Theta_{12}(0,0)\Theta_{12}(\tau,\vec{x})\rangle$ finite volume effects. Renormalized and built from diagonal components (compare Equ. (2.78)). Errors are statistical Jackknife errors.

4.2 Transport Coefficients

This section of the thesis covers the analysis of the data set described in section 4.1. The focus in this chapter lies on the reconstruction of transport coefficients as described in section 2.2. One of the coefficients considered here is of first order and two are of second order.

4.2.1 First Order: Shear Viscosity

The first coefficient is the shear viscosity η which is a first order transport coefficient. As this transport coefficient is dynamical in nature, analytic continuation is necessary, i.e. the reconstruction of a spectral function from an Euclidean correlator. This reconstruction is done here by a direct fit of the correlator to an ansatz containing a suitably parametrized spectral function.

Choice of the Ansatz for the Spectral Function

Early attempts to get the viscosity from Euclidean correlator measurements on the lattice used a Breit-Wigner ansatz to fit the correlator, e.g. [55, 76, 83, 84]. Although the ansatz can describe the data well, it consistently produced a peak of the spectral density at roughly π/a. As this is basically the maximum resolvable energy on the lattice, i.e. the lattice cutoff, the result of fits like that is not so much a signal for transport from the low frequency tail of the peak, but rather a signal for some spectral weight distributed mostly close to the lattice cutoff. This can be expected as the spectral function should scale like ω^4 as in the continuum until it is cut off by the lattice regularization. A later study [67] also got a value for the position of the peak in a comparable energy range, but described such an ansatz as an "unsatisfactory attempt to extract the viscosity" for another reason: It does not show the expected ω^4 behaviour for large energies due to asymptotic freedom.

As pointed out in section 2.2.4 the current work uses finite momentum data. This has to be reflected in the ansatz. Following [69], a generic ansatz for the spectral function may be divided in parts relevant for different energy ranges $\rho = \rho_{low} + \rho_{high}$.[2] For the low energy range the predictions from hydrodynamics [89] can be used as long as $\omega, q < \pi T$. For the relevant channels these predictions imply for Equs. (2.97) and (2.98)

$$\frac{\rho_{13,13}(\omega,q)}{\omega} \xrightarrow{\omega,q\to 0} \frac{\eta}{\pi}\frac{\omega^2}{\omega^2 + (\eta q^2/(\epsilon+p))^2} \tag{4.29}$$

$$\frac{\rho_{33,33}(\omega,q)}{\omega} \xrightarrow{\omega,q\to 0} \frac{\Gamma_s}{\pi}\frac{(\epsilon+p)\omega^4}{(\omega^2 - v_s(q)^2q^2)^2 + (\Gamma_s\omega q^2)^2}, \tag{4.30}$$

with the sound attenuation length $\Gamma_s = (\frac{4}{3}\eta + \zeta)/(\epsilon + p)$ and the speed of sound $v_s(q)$. The speed of sound was calculated in a conformal theory [12]

$$v_s(q) = v_s\left(1 + \frac{\Gamma_s}{2}q^2\left(\tau_\Pi - \frac{\Gamma_s}{4v_s^2}\right) + \mathcal{O}(q^4)\right), \tag{4.31}$$

with the relaxation time for shear stress τ_Π.

This expectation from hydrodynamics strongly influences the ansatz for $\rho_{33,33}$ at low energies

$$\frac{\rho_{low}(\omega,q)}{\tanh(\omega/2T)} = \frac{2\Gamma_s}{\pi}\frac{(\epsilon+p)\omega^4}{(\omega^2 - v_s(q)^2q^2)^2 + (\Gamma_s\omega q^2)^2}\frac{1+\sigma_1\omega^2}{1+\sigma_2\omega^2}, \tag{4.32}$$

[2] In contrast to [69] the ansatz here discards the parametrization of the medium frequency part, as its inclusion did not lead to a better fit of mock data, it seems to be primarily sensitive to noise.

with the first term of a systematic parametrization of the behaviour for larger energies by the parameters σ_1 and σ_2. These two parameters also allow for an effective finite width of the spectral function. The ansatz at high energies

$$\frac{\rho_{high}(\omega, q)}{\tanh(\omega/2T)} = \omega^4 \tanh^2\left(\frac{\omega}{2T}\right) \frac{2d_A}{15(4\pi)^2} \tag{4.33}$$

merely fixes the perturbative high energy behaviour. Previous studies have shown that there are no measurable modifications of the high energy limit. As explained above, the cutoff tends to have a strong effect on the correlator, the fit will incorporate a parametrization of its effect explicitly as described below.

Usage of the Wilson Flow

In this work the Wilson flow is used for three reasons:

1. It strongly suppresses the statistical errors on the observables of interest, which are infrared quantities.

2. As the fluctuations below a physical distance can be damped, it provides a method to alleviate cutoff effects, as long as the effective smearing radius is larger than the lattice spacing $r_{smear} > a$. Keeping that distance fixed in physical units for different lattice spacings, virtually renders observables independent of the lattice spacing. Nevertheless, the observables remain still physical and meaningful, as they describe physics at the scale $r_{smear} = \sqrt{8t}$.

3. It leads to a suppression of the high energy parts of the spectrum down to the scale π/r_{smear}. The observables at a finite flow time are therefore much more sensitive to the low frequency behaviour of the theory, i.e. its transport properties.

As hinted to above, the effect of this suppression of the high energy contributions in the spectrum is modelled directly in the fit as explained in section 3.4.2. The two parametrizations of the cutoff, which are used here, are

$$W_\Omega^{\tanh,\Sigma}(\omega) = \frac{1}{2}\left(1 + \tanh\left(\frac{\Omega - \omega}{\Sigma\sqrt{6}/\pi}\right)\right), \tag{4.34}$$

$$W_\Omega^{\mathrm{erf},\Sigma}(\omega) = \frac{1}{2}\left(1 + \mathrm{erf}\left(\frac{\Omega - \omega}{\Sigma}\right)\right) \tag{4.35}$$

with the error function erf and the cutoff scale $\Omega = \pi/r_{smear} = \pi/\sqrt{8t}$. The parameter Σ defines the width of the cutoff. The factor $\sqrt{6}/\pi$ scaling the width in $W_\Omega^{\tanh,\Sigma}(\omega)$ is introduced such that the associated distribution has the same variance as for $W_\Omega^{\mathrm{erf},\Sigma}(\omega)$, i.e. for a Gaussian.

This gives all ingredients for the fit ansatz:

$$C_{33,33;\Omega}(\tau, q) = \int_0^\infty \mathrm{d}\omega K(\tau, \omega) W_\Omega^{f,\Sigma}(\omega) \rho_{33,33}(\omega, q). \tag{4.36}$$

The Wilson flow has effectively introduced another (continuous) direction in the data set, the cutoff scale Ω. As a by-product of the usage of the Wilson flow this enlarges the number of data points in the fit. The renormalization, following section 2.2.1, has to be done for every smearing separately.

A remark on the behaviour of the correlator at short Euclidean times is also in order to correctly interpret the correlator for large flow times. Following Equ. (2.125), the smearing evolves local operators to non-local ones with approximately Gaussian support in position space for large energies or weak coupling. Considering then the Euclidean correlator of such smeared operators, yields a correlator which is also smeared in the Euclidean time distance, because the Gaussians in the operators factorize. This is quantified for leading order perturbation theory in section 2.3.2 and leads to the negative curvature of the correlator for Euclidean time separations which are smaller than the smearing radius. This feature does not arise for the infrared behaviour at length scales much larger than the smearing radius, which is the relevant one for studying the transport properties of the theory.

Determination of the Viscosity

The simulations at the two larger volumes of section 4.1.5 are also used in this section to determinate the shear viscosity η. Together with the finite momentum lattices at different temperatures they are listed in Tab. 4.5. The two different spatial lattice sizes have aspect ratios $r_a = n_s/n_t$ of 6 and 8, which should both be close to the infinite volume limit, albeit yielding small but different finite momenta. The momenta accessible on a lattice are determined by the condition that the spatial lattice size is a multiple of the wavelength:

$$n_s = n\frac{2\pi}{q_n} \tag{4.37}$$

$$\Leftrightarrow q_n = 2\pi T \frac{n}{r_a}. \tag{4.38}$$

Note that in Equ. (4.38) r_a is the physical aspect ratio, which coincides with n_s/n_t only in the isotropic case. Using standard anisotropic lattices with $a_s = \xi a_t > a_t$ while keeping n_s fixed, will therefore not make smaller or additional momenta accessible. According to [69], only momenta below $|\vec{q}| \leq \pi T$ can be taken for the hydrodynamic fit ansatz of Equ. (4.32). The momenta measured in

T/T_c	n_t	n_s	β	N_{Stout}	ρ_{Stout}	N_{conf}	N_{sep}	$N_{streams}$
1.5	8	48	4.81166	25	0.0837365	$5.6 \cdot 10^4$	32	27
1.5	8	64	4.81166	25	0.0837365	$2.4 \cdot 10^4$	32	27
3.0	8	48	5.36624	25	0.0837365	$2.2 \cdot 10^4$	32	9
3.0	8	64	5.36624	25	0.0837365	$9.4 \cdot 10^3$	32	9
4.5	8	48	5.70092	25	0.0837365	$2.7 \cdot 10^4$	32	18
4.5	8	64	5.70092	25	0.0837365	$1.1 \cdot 10^4$	32	18

Table 4.5: Parameters of the finite momentum runs.

this work correspond to $n = 0, 1, 2$. For the two lattice sizes this corresponds to at total of 4 different finite momenta $\pi T\{\frac{1}{3}, \frac{2}{3}, \frac{1}{4}, \frac{1}{2}\}$, all well below πT.

Fig. 4.4 shows the dependence of the measurement of the correlator $C_{33,33}(\tau, q)$ on the momentum q. The difference between the two volumes is also visible in this correlator. For the combined fit the two zero momentum correlators contribute for the same values for τ and q, so they will average and describe a monotonous dependence of the correlator on the momentum.

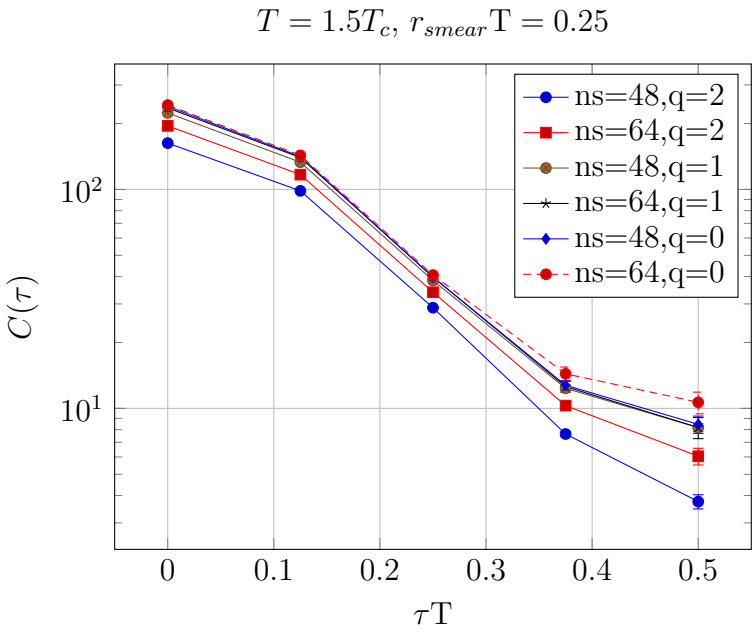

Figure 4.4: $C(\tau, q) = \frac{1}{T^5} \int \mathrm{d}\vec{x} e^{i2\pi\vec{q}\vec{x}/n_s} \langle \Theta_{33}(0,0)\Theta_{33}(\tau, \vec{x})\rangle$. The 3 direction is the direction proportional to the momentum. Errors are statistical Jackknife errors.

The data points for the fit are selected according to the following criteria:

- All momenta are used in the fit as they are small enough for hydrodynamics to be applicable.
- The smearing radius has to be larger than a certain scale to suppress discretization errors: $r_{smear}T > \lambda$.

- The low end of the fit range in Euclidean time is dynamically cut depending on the smearing radius to ensure that the effects from the parametrization of the cutoff are small: $\tau > r_{smear}x$.

The choices for λ are 0.14, 0.20, and 0.25, for x they are 1.0, 1.2, and 1.4. These selection criteria leave between 24 and 84 data points for the 5 parameters of the fit. The cutoff width Σ is kept fixed during the fit to avoid that it grows too large and modifies the low frequency behaviour. The choices for Σ are $0.5T$, $1T$, and $2T$. Both functional forms $W^{\tanh}$ and W^{erf} are used. To account for dependence on initial conditions in the fit, the three choices of the initial value of $\Gamma = 0.2T^3, 0.35T^3, 0.6T^3$ are used, keeping all other initial conditions fixed at $\sigma_1 = \sigma_2 = 0$ and $T\tau = v = 1$. This is a rather unbiased choice, as it reflects only the expected order of magnitude and no fine tuning. All these choices result in a total of 162 separate analyses for every temperature. The scattering of their results yields the systematic errors cited for the final results.

The fit is performed correlated in Euclidean time, flow time, and momentum and the quoted errors are Jackknife errors.[34] The fit results are listed in Tab. 4.6. The values given in this table are the mean over all analyses of the median of the Jackknife values. The first given error is a statistical error. It is the median analogue of the 1σ standard deviation of the mean: The mean over all analyses of half the difference of the 84% and 16% quantile of the distribution of the Jackknife values. The second error is a systematic error. It is the standard deviation over all analyses of the median of the Jackknife values. The median and quantiles are used here, because the fit tends to produce a lot of outliers.

The large uncertainty of the parameter τ reflects the instability of the fit. It has been tried to get a more stable result by applying cuts on the distributions of the fit parameters, especially τ, but apart from changing the constrained parameter itself this had no stabilizing effect on the result. In particular the value for the transport coefficient Γ_s was virtually invariant under such cuts.

The results for η/s have quite large statistical and systematical errors. As can be seen in Fig. 4.5, this makes it impossible to make a reliable statement on the dependence of the viscosity on temperature. It is at the current error level consistent both with a constant and with the dependence given in [50]. The figure also gives the results of previous studies. This work is compatible with these

[3]The first $\mathcal{O}(10)$ iterations of the minimization of χ^2 are performed with the uncorrelated χ^2. This procedure improved the convergence of the minimization of the correlated χ^2 and led to fit results with smaller correlated χ^2.

[4]The fit parameter used in the actual fitting routine is not τ, but $a\,\text{asinh}(\tau/a)$. This has no significant effect on the value of the transport coefficient, but partly avoids an instability leading to arbitrarily large values of τ.

T/T_c	1.5	3.0	4.5
χ^2/DOF	1.2(2)(6)	2.2(3)(5)	2.1(3)(8)
η/s	0.24(7)(6)	0.32(5)(5)	0.43(9)(7)
σ_1	-0.07(3)(4)	-0.14(2)(3)	-0.12(4)(4)
σ_2	0.03(2)(3)	0.09(4)(4)	0.1(2)(2)
τ	3(11)(5)	7(22)(26)	20(70)(40)
v	4(2)(2)	2(1)(2)	2(2)(1)
Ω_r	0.97(2)(1)	0.93(2)(3)	0.94(2)(3)

Table 4.6: Results of the fits to a hydrodynamics ansatz of the spectral function. DOF is the number of degrees of freedom. The first error is statistical, the second systematical.

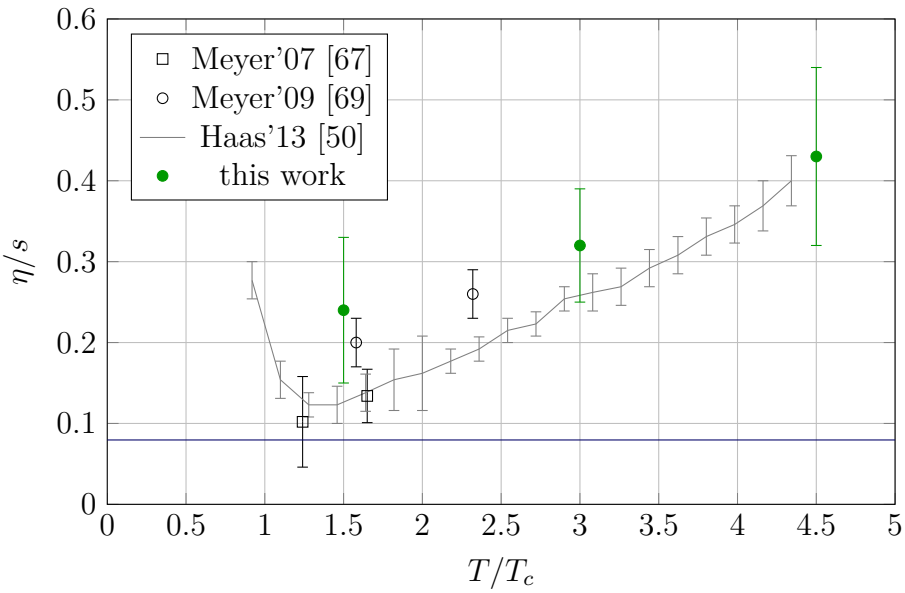

Figure 4.5: The results of the determination of the viscosity from this work compared to previously reported values in the literature.

results within the error.

4.2.2 Second Order: λ_3

The second coefficient considered here is the second order transport coefficient λ_3. As stated in section 2.2.4, the coefficient λ_3 is of thermodynamical nature and therefore accessible without having to reconstruct a spectral function, which makes it in principle easier to access for lattice QCD simulations. The defining Equs. (2.103) and (2.105) from section 2.2.4 are reproduced here for convenience

$$\lambda_3 = -4 \lim_{p_3,q_3\to 0} \frac{\partial^2}{\partial p_3 \partial q_3} C_{\lambda_3}(p_3, q_3)$$
$$C_{\lambda_3}(p_3, q_3) = C_{\lambda_3,2}(p_3 + q_3) + C_{\lambda_3,3}(p_3, q_3)$$

with a two point correlation function $C_{\lambda_3,2}$ and a three point correlation function $C_{\lambda_3,3}$.

Strategy

On the lattice only the correlators are measured, not their derivatives. The derivatives could be implemented as a finite difference, which would give a very large systematic error, because only the lowest momentum point is used. An alternative is to fit a range of low momentum points to a generic functional form, e.g. a power series. The most general power series obeying the symmetries $p \leftrightarrow q$ and $(p, q) \to -(p, q)$, is to quadratic order in the momenta

$$C_{\lambda_3}(p_3, q_3) = f_0 + f_1 p_3 q_3 + f_2(p_3^2 + q_3^2), \tag{4.39}$$

from which the transport coefficient can be simply read off as $\lambda_3 = -4f_1$. This functional form should work for small momenta and, as one is interested in the zero momentum limit anyway, this is the interesting region. Systematic errors from the choice of the functional form can be checked by including higher orders.

Fig. 4.6 shows the momentum combinations from Tab. 4.1, which are available for the three point correlator. The ansatz parametrizes a paraboloid on these points with major and minor axes on the diagonals of the plot. These points are shifted by using different volumes, such that independent data are added. In the data set of this thesis up to 4 volumes are available. For the analysis of this section only the $T = 1.5\ T_c$ data set with $n_t = 8$ and the four volumes $n_s = 40, 48, 56, 64$ are used.

An important consequence of not performing a spectral decomposition is that one has to get rid of the divergent part of the correlator before extracting physical

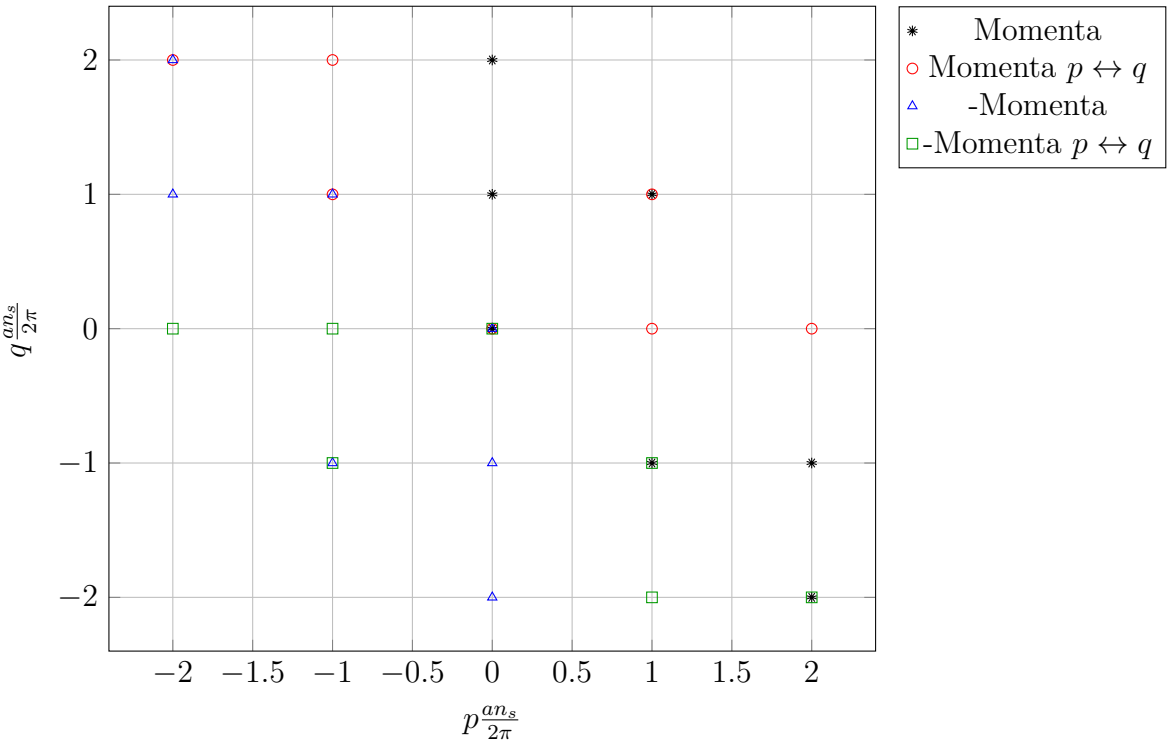

Figure 4.6: Available momenta with $|p+q|\frac{an_s}{2\pi} \leq 2$. Independent points in black, other points are covered by symmetry transformations.

observables, i.e before trying to fit transport coefficients. In order to do that, one can consider the difference of the correlator at finite temperature and subtract the correlator at effectively zero temperature (like e.g. [81]). For that to work, both correlators need to be renormalized properly before subtraction or need to have the same renormalization properties. Here the difference is always taken at the same value of the inverse coupling β, but larger temporal lattice extent. As the correlators are projected to zero Euclidean frequency, i.e. summed over Euclidean time, that can be done directly. The reference temperature in this analysis is $T_0 = 0.75T_c$ with $n_t = 16$. This can be used as effectively zero temperature, because it is below the phase transition and the biggest changes in transport properties are expected only in the temperature regime above T_c where there is a thermal medium.

As already mentioned in the discussion of the shear viscosity, two point correlators of the energy momentum tensor all need very high statistics and noise reduction techniques to be measured to sufficient precision, especially for infrared physics. The three point correlator is even noisier and that has been pointed out already in the context of reconstructing λ_3 from lattice QCD simulation in [74].

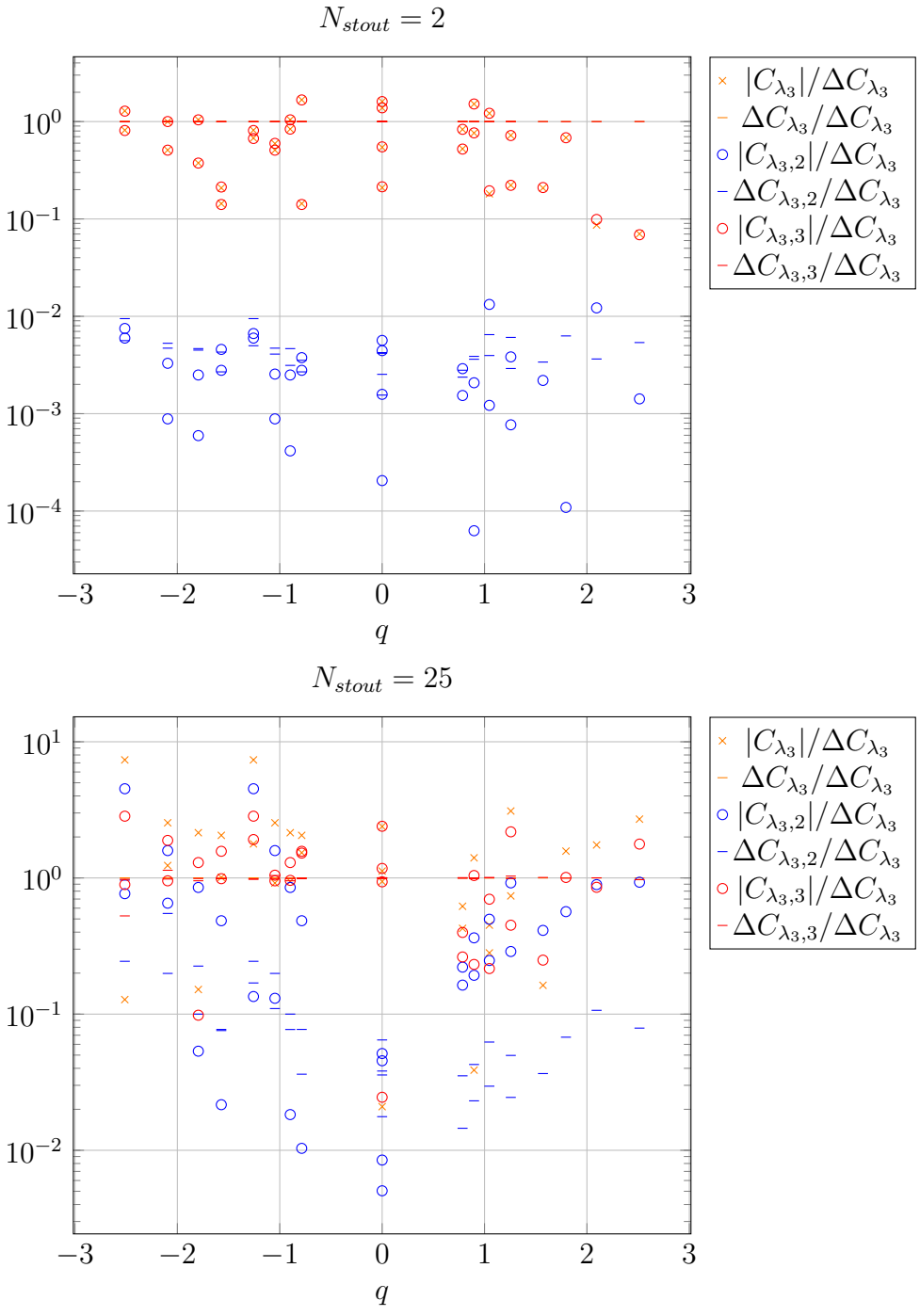

Figure 4.7: Renormalized correlator measurements relative to the error level of the combined correlator ΔC_{λ_3}. All (p, q) combinations from Tab. 4.1 are shown in dependence of q only. Data is shown for $T = 1.5T_c$, $n_t = 8$, $T_0 = 0.75\ T_c$, $n_s = 40, 48, 56, 64$.

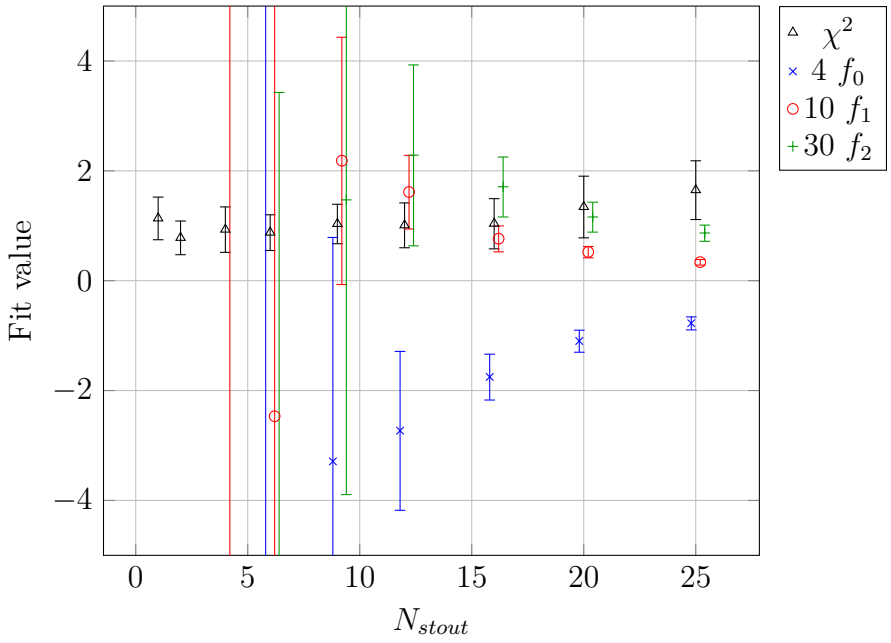

Figure 4.8: Parameters of fits of the data for the combined correlator C_{λ_3} to the series expansion ansatz of Equ. (4.39). λ_3 is proportional to f_1. Points for the fit parameters are a bit shifted for better visibility.

Combined Correlator

Fig. 4.7 shows the significance of the measured correlators for the determination of λ_3. For low smearing, the combined correlator C_{λ_3} hardly exceeds the statistical error level of the measurement, it is consistent with noise. One also sees that the total error on the combined correlator is dominated by the error of the three point function: It is more than two orders of magnitude larger than the error on the two point function.

For strong smearing and some momenta, the combined correlator seems to start leaving the region of statistical insignificance. But still only three points are above the two sigma level and the total error is dominated by the error on the three point function – but it is only about one order of magnitude larger than the error on the two point function. The values of the two point function alone are very significant at the strong smearing.

Ignoring the large error on the combined correlator and performing a fit to the ansatz of Equ. (4.39), yields the fit results shown in Fig. 4.8 in dependence of the smearing. The χ^2/DOF is compatible with 1 for all fits, but that is expected, given that the error of the individual data points is large. To get the physical value of λ_3, an extrapolation to vanishing smearing has to be performed. For this, one is looking for a plateau or at least a linear dependence on the number of smearing steps as is expected from a leading order behaviour in the flow time. This is clearly not possible with these fits.

Taken together, the large error on the three point function makes it impossible to state a value with reliable error estimate for λ_3.

Two Point Correlator

As already seen in Fig. 4.7, the contribution from the two point correlator $C_{\lambda_3,2}$ alone has a statistically significant deviation from noise for large smearings. This becomes apparent in the analogous plot for the two point correlator in Fig. 4.9. This plot shows only points with independent information, i.e. only one (p, q) combination with a given $p+q$ is plotted. The plot for the larger smearing shows that the data falls into two categories: The points with $q = 0$ are within one σ consistent with noise, whereas the points for $q \neq 0$ are more than six σ away from noise and give a clear signal for a temperature dependent contribution to this finite momentum correlator.

The task is now to reconstruct the contribution to λ_3 from this signal which is solely due to the two point correlator. By constructing this contribution one can determine the order of magnitude of λ_3 – assuming that the three point contribution is of the same order of magnitude. Fig. 4.10 shows $C_{\lambda_3,2}$ for a range of smearings. General features are that the statistical uncertainty decreases drastically with the smearing and also that the magnitude of the correlator decreases. For all values of the smearing, the correlator at vanishing momentum is consistent with zero and for large momenta the correlator tends to zero as well (for smearing which lead to a statistical accuracy to allow for such a statement). This functional form is clearly not consistent with a power series ansatz up to second order in momentum in analogy to the ansatz of Equ. (4.39).

A suitable ansatz has to model the decay of the correlator for large momenta. This decay should also be stronger for strong smearings than for small ones. Section 2.3.2 contains a derivation of exactly such a feature for local product operators like the energy momentum tensor in leading order in the coupling and the Wilson flow time, c.f. Equ. (2.130). One may assume that the correlators can be described by a power series in the momentum, regulated by a Gaussian cutoff like the one from section 2.3.2, for the temperature T and the reference temperature T_0 individually. Then one can write down a natural ansatz which incorporates all necessary features

$$C_{\lambda_3,2}(q_3) = (g_0 + g_2 q_3^2) e^{-s q_3^2}, \tag{4.40}$$

where s is the parameter for the quadratic inverse width of the Gaussian.[5] As

[5]The width of the Gaussian is given as a free parameter and is not constrained to the value

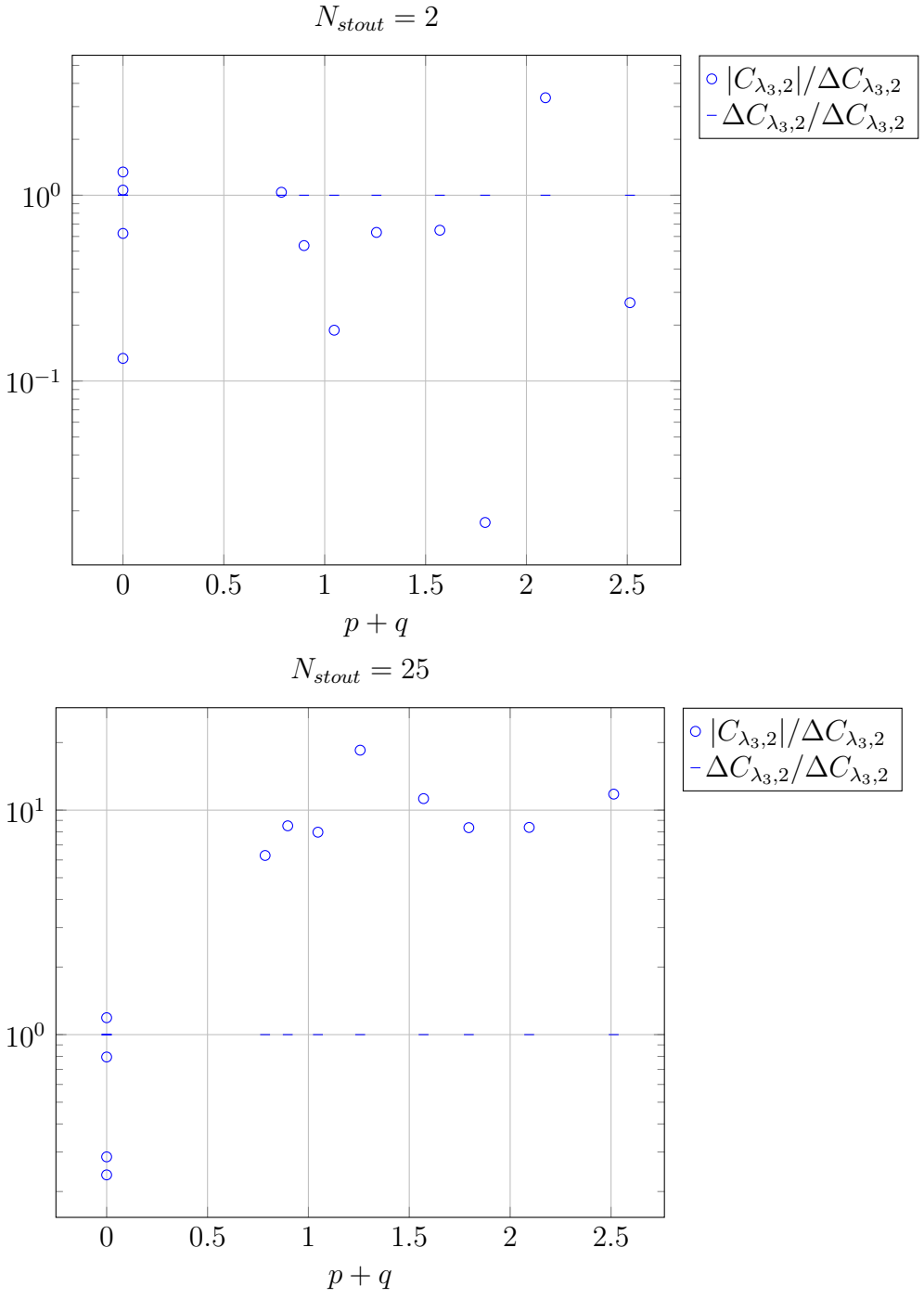

Figure 4.9: Renormalized two point correlator measurements relative to the error level of the two point correlator $\Delta C_{\lambda_3,2}$. Data is shown for $T = 1.5\ T_c$, $n_t = 8$, $T_0 = 0.75\ T_c$, $n_s = 40, 48, 56, 64$.

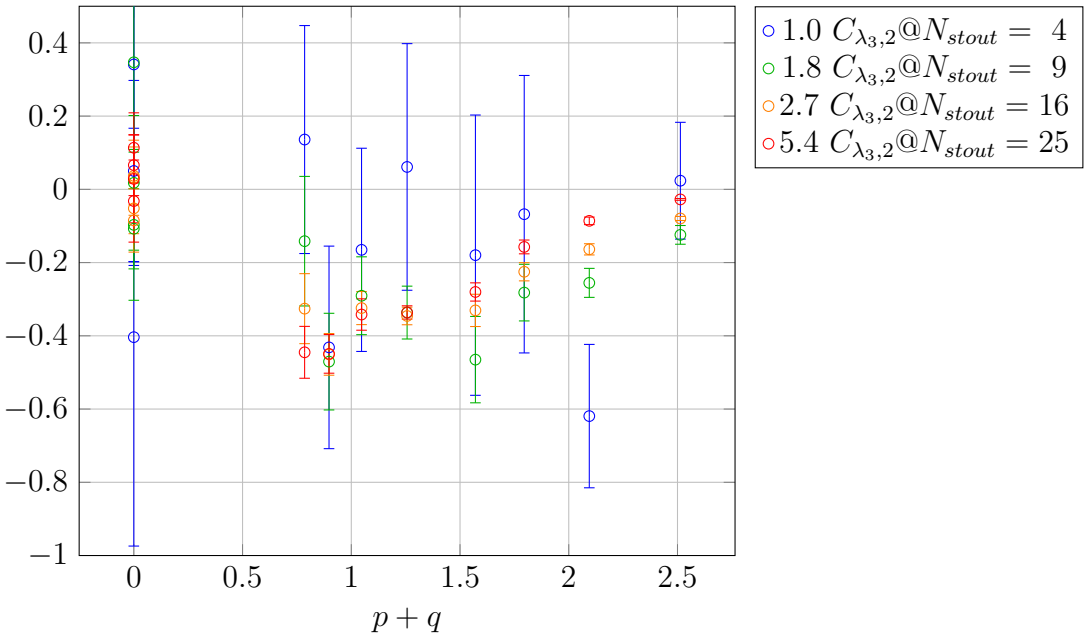

Figure 4.10: Renormalized two point correlator measurements $C_{\lambda_3,2}$. Data is scaled such that the different smearings coincide at one momentum. Data is shown for $T = 1.5T_c$, $n_t = 8$, $T_0 = 0.75T_c$, $n_s = 40, 48, 56, 64$.

within the precision of the data, the correlator at vanishing momentum is consistent with zero, one can remove the parameter g_0 from the fit and fit the data with the two parameters g_2 and s. The two point correlator contribution to λ_3 is $-8g_2$, because the quadratic term, which is contained in the Gaussian, is regarded as a pure artefact from the smearing or Wilson flow.

The result of this fit is given in Fig. 4.11. The reduced χ^2 is again consistent with one. But in contrast to the fit of the combined correlator C_{λ_3}, this fit had a statistically significant signal to fit for the larger smearings. This is also the range, in which the parameters resulting from the fit are linear in the number of stout smearing steps, i.e. the Wilson flow time and one can extrapolate their values easily to vanishing smearing. The linear extrapolated value of g_2 for vanishing smearing is $-0.377(7)(10)T^{-2}$ and the value for s is $0.351(7)(38)T^{-2}$. The extrapolation uses the points at $N_{stout} \in \{9, 12, 16\}$. The first error is a statistical Jackknife error and the second a systematical error, defined as the difference to the result of the fit, using also the point with $N_{stout} = 25$. This gives a contribution to λ_3 from the two point function of $3.02(6)(8)T^{-2}$ compared to the analytic leading order result $\frac{1}{3}T^{-2}$ in reference [74][6]. This could indicate a strong non-perturbative

derived in Equ. (2.130), because the value in that formula is derived for leading order in the gauge coupling.

[6]The different power of temperature compared to reference [74] is due to a different normalization of the correlator.

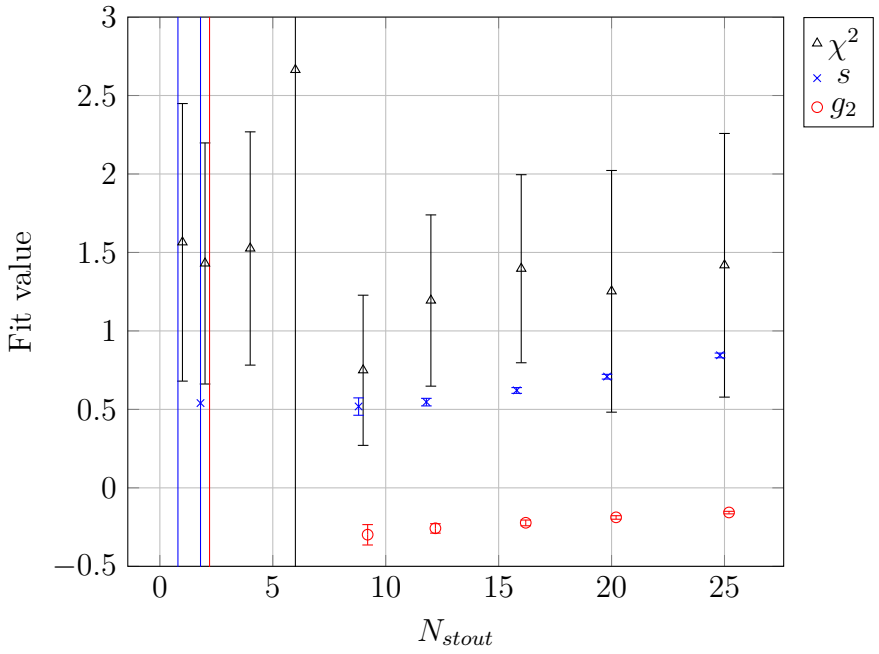

Figure 4.11: Parameters of fits of the data for the two point correlator $C_{\lambda_3,2}$ to the Gaussian cut off series expansion ansatz of Equ. (4.40). The two point correlator contribution to λ_3 is proportional to g_2. Points for the fit parameters are a bit shifted for better visibility.

contribution to λ_3. Note that the inverse Gaussian width is not zero but has a finite positive value. For vanishing smearing the smearing radius is expected to diverge.[7]

It is desirable to have an independent crosscheck to determine whether the result is based on an artefact from the method. Unfortunately, the value of λ_3 in (quenched) QCD has not been determined so far. Therefore it is attempted to check the method with a different transport coefficient κ.

4.2.3 Second Order: κ

The third and last coefficient treated in this thesis is the second order transport coefficient κ. Like for λ_3 of the last section it is possible to reconstruct this coefficient without having to reconstruct a spectral function. The defining Equ. (2.102) from section 2.2.4 is also reproduced here:

$$\kappa = \lim_{q_3 \to 0} \frac{\partial^2}{\partial q_3^2} C_{12,12}(\vec{q}).$$

[7]Physically, this finite width at zero smearing could be interpreted as the effective smearing width of the finite lattice spacing. Extrapolating this further to the point at which the inverse width becomes zero and the width becomes infinite, might correspond to taking the continuum limit while simulating only at one fixed lattice spacing. The extrapolated value for g_2 at this point is $-0.58(3)(7)T^{-2}$.

In contrast to the λ_3 case, the determination of this coefficient only requires a two point function. Therefore this coefficient could be accessible in current lattice QCD calculations.

The strategy to extract κ from the lattice data is mainly identical to the two point correlator strategy of the last section. The only difference is that the two point correlator $C_{12,12}$ relevant for κ can be constructed not only from the off-diagonal components of the energy momentum tensor, but also from differences of the diagonal entries (analogous to the relevant two point correlator for η of section 4.2.1). The correlator built from the off-diagonal elements will be referred to as $C_{12,12,\Theta}$ and the one built from the differences as $C_{12,12,\Delta}$. The diagonal version $C_{12,12,\Delta}$ has the advantage that there is no inherent systematic error from the choice of the renormalization scale.

The significance of the correlator measurement is shown in Fig. 4.12. As for the two point correlator in the λ_3 case, the measurement for small smearing levels is indistinguishable from noise, whereas for large smearing the measurement is clearly different from zero with a significance of over 10 σ. The measurements of $C_{12,12,\Theta}$ and $C_{12,12,\Delta}$ have comparable statistical errors and agree within one σ. This shows again that the renormalization technique for off-diagonal elements of the energy momentum tensor introduced in section 2.2.1 works. The additional systematic error on $C_{12,12,\Theta}$ from the choice of the renormalization scale is subleading compared to the statistical error. As both correlator choices are consistent, in the remainder of this section only the correlator $C_{12,12,\Delta}$ is considered.

Unlike the situation for λ_3, the point at vanishing momentum has also a significantly finite value. This indicates that in the case of $C_{12,12}$ the constant contribution in the power series expansion also carries temperature dependence. In the fit to the ansatz of Equ. (4.40) (reproduced here for convenience)

$$C_{12,12}(q_3) = (g_0 + g_2 q_3^2) e^{-s q_3^2}, \tag{4.41}$$

the parameter g_0 has to be kept in the fit.

Fig. 4.13 shows the correlator for some choices of the smearing level. Again, the absolute magnitude of the correlator decreases with smearing as well as the statistical error. One can also see a suppression of large momenta, but the width of of the functional form of this suppression remains constant with increasing smearing. This is in contrast to the expectation from the interpretation of last section of the suppression as a smearing cutoff scale in momentum.

Nevertheless, one can fit the correlator with the ansatz and the result is displayed in Fig. 4.14. The fits for weak and medium strong smearings give a good χ^2, while those for strong smearing have a large χ^2. This means that for large enough

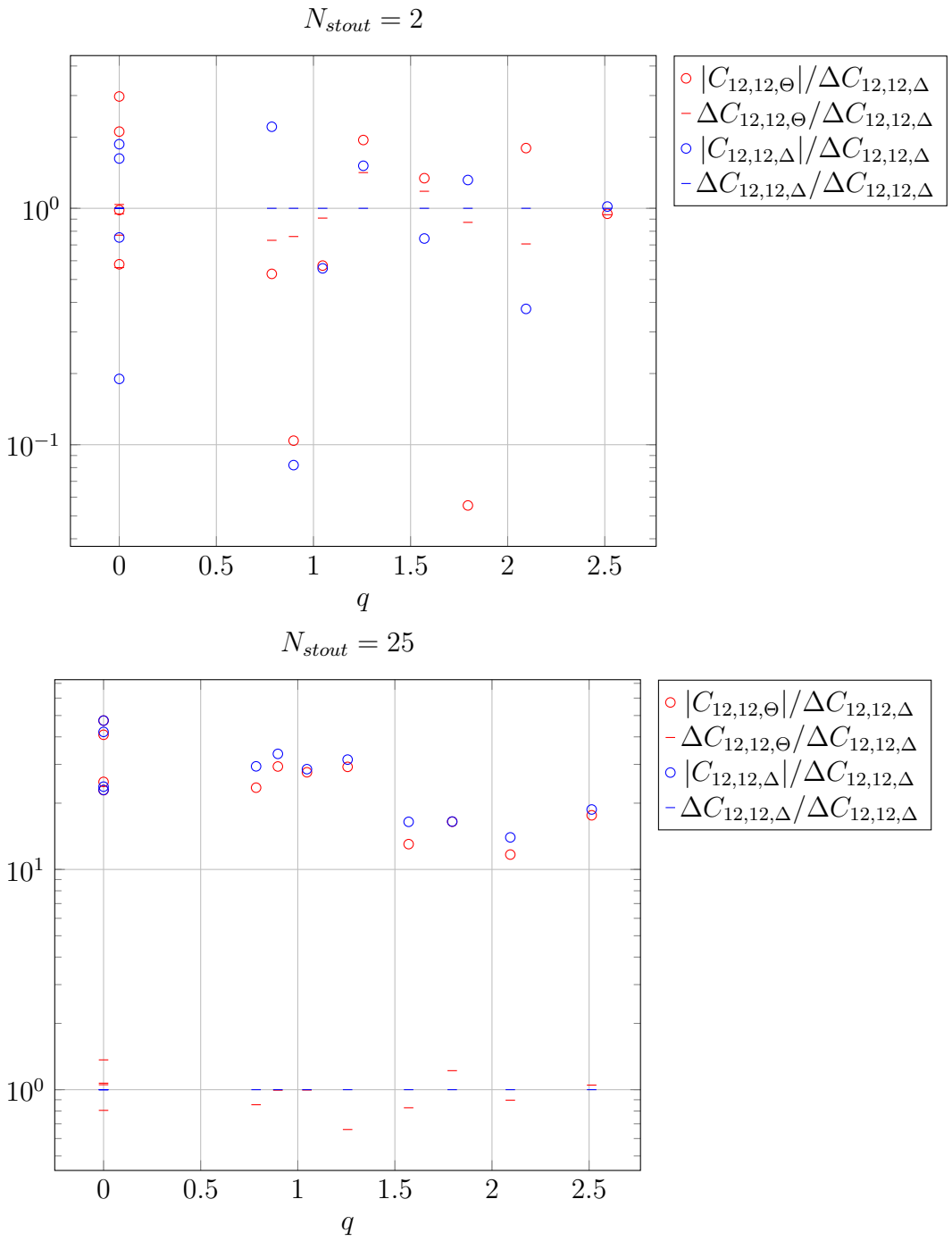

Figure 4.12: Measurements of the renormalized correlators $C_{12,12,\Theta}$ and $C_{12,12,\Delta}$ relative to the error level $\Delta C_{12,12,\Delta}$. Data is shown for $T = 1.5\ T_c$, $n_t = 8$, $T_0 = 0.75\ T_c$, $n_s = 40, 48, 56, 64$.

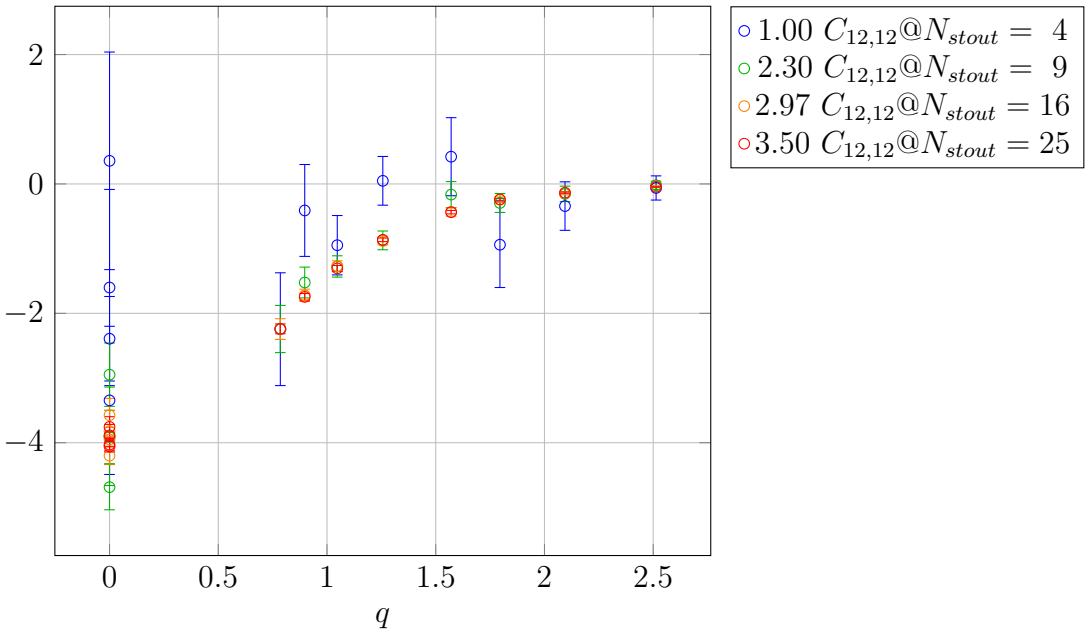

Figure 4.13: Renormalized correlator measurements $C_{12,12,\Delta}$. Data is scaled such that the different smearings coincide at one momentum. Data is shown for $T = 1.5\ T_c$, $n_t = 8$, $T_0 = 0.75\ T_c$, $n_s = 40, 48, 56, 64$.

smearing the fit ansatz is insufficient and it cannot describe the data. As one sees from Fig. 4.13 that the functional form of the data is the same independent of smearing, one can interpret the good fits for weak smearing as artefact caused by the large statistical error. The coefficient g_2 in the fit, which should be proportional to κ, is consistent with zero for all choices of the smearing. The corresponding functional contribution in the fit seems to be somehow orthogonal to the functional form of the data. The fit does reflect, however, that the width is approximately constant.

Of course, one can also find ansätze which fit this data quite well. For example, the ansatz

$$C_{12,12}(q_3) = ce^{a-a\sqrt{(q_3/b)^2+1}} \tag{4.42}$$

fits the data well for all smearings, as seen in Fig. 4.15. In this ansatz $\kappa = -ac/2b^2$. With this fit result it is clearer that the functional form of the data does not depend on the smearing, as the fitted values of the parameters are nearly constant within errors. However, this ansatz has no clear physical interpretation in the Wilson flow picture, so it is at best difficult to extract a reliable value for the transport coefficient from it. For large smearing, this ansatz tends to yield a value for κ of about $\mathcal{O}(1)T^{-2}$, compared to the analytic leading order lattice perturbation

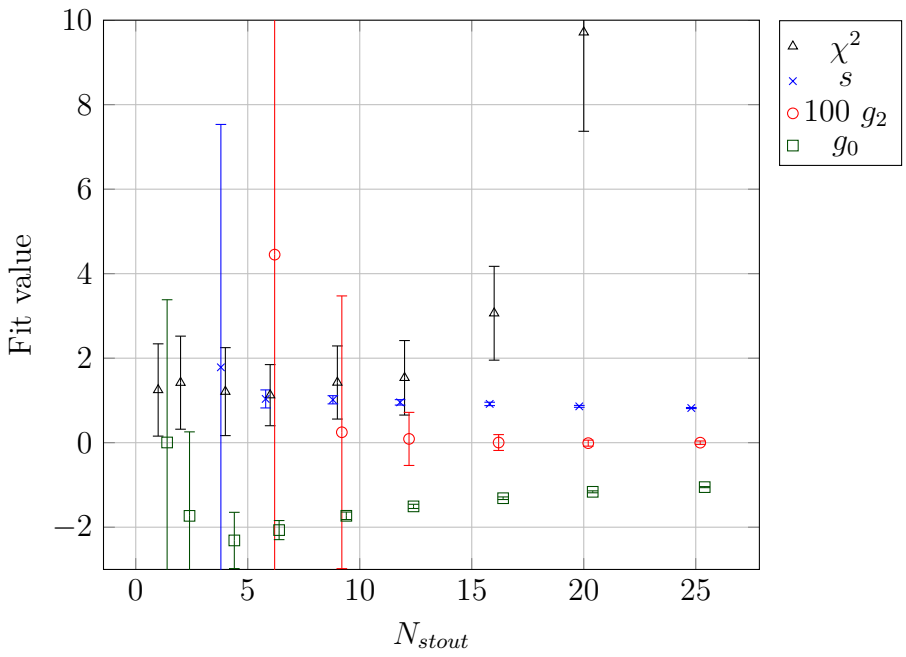

Figure 4.14: Parameters of fits of the data for the correlator $C_{12,12,\Delta}$ to the Gaussian cut off series expansion ansatz of Equ. (4.41). The transport coefficient κ is proportional to g_2. Points for the fit parameters are a bit shifted for better visibility.

theory result $0.47T^{-2}$, to a previous lattice determination $0.36(15)T^{-2}$ [81][8], and to the value from AdS/CFT $1.125T^{-2}$ [12].[9]

For the data at hand, the value of the transport coefficient depends much on the choice of the ansatz, because there is a relatively large gap between the vanishing momentum and the first finite momentum data point. This makes it virtually impossible to reliably extract the second derivative of the function, when at a comparable scale features set in like the fall off for large momenta, which are not represented in a power series to second order.

Like in the case of λ_3, the difference of the two point correlation function relevant for κ at finite and zero temperature shows a significant temperature dependence for small momenta again. This can be seen as a signal for a change in low energy features of the theory which implies a change in the transport coefficient. Unfortunately, the change in the coefficient cannot be reliably quantified.

[8] [81] had twice the spatial lattice extent, thus smaller spatial momenta, simulated at (much) higher temperatures, and generated an order of magnitude more quenched statistics, which is currently not realistic for dynamic studies.

[9] The different power of temperature in the references is due to a different normalization of the correlator.

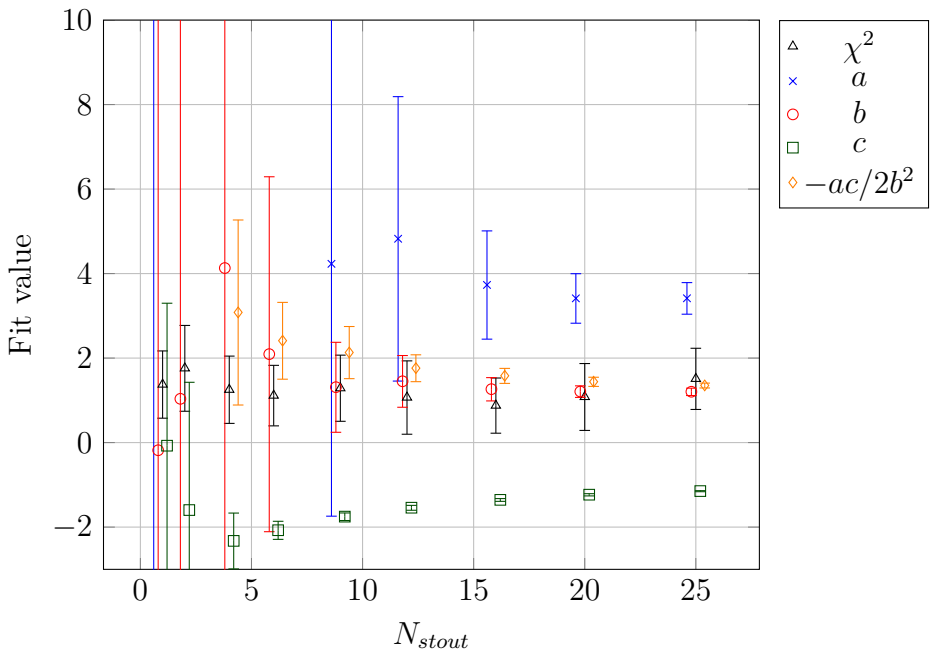

Figure 4.15: Parameters of fits of the data for the correlator $C_{12,12,\Delta}$ to the alternative ansatz of Equ. (4.42). The transport coefficient κ is proportional to $-ac/2b^2$. Points for the fit parameters are a bit shifted for better visibility.

4.3 Improved Holographic QCD

This section is devoted to a short presentation of some preliminary results of the comparison of quenched lattice data with the Improved Holographic QCD (IHQCD) model.[10] IHQCD, as outlined in section 2.4.2, is an approach specifically tailored to describe pure 4D Yang-Mills theory holographically by a classical theory of 5D gravity. As it does not include quantum corrections, it is most reliable in the infrared. The model has some free phenomenological parameters which have to be fixed e.g. by comparison to lattice simulations.

Quantities, which are used for that purpose already, are glueball masses, the topological susceptibility, and the equation of state. Additional quantities can be used to constrain parameters which are not sensitive to the quantities already in use, to overconstrain the parameters, or to check the predictions of IHQCD based on the already used parameters. A set of parameters, which is based on more or better data, will then lead to a better prediction of dynamic properties of the quantum field theory, which are out of principle not accessible by the pure lattice approach.

Additional quantities, which are accessible on both holography and the lattice,

[10] An updated and extended version of the results presented here will be part of an upcoming publication together with Francesco Nitti, Elias Kiritsis, and Umut Gürsoy on the holographic part of this project.

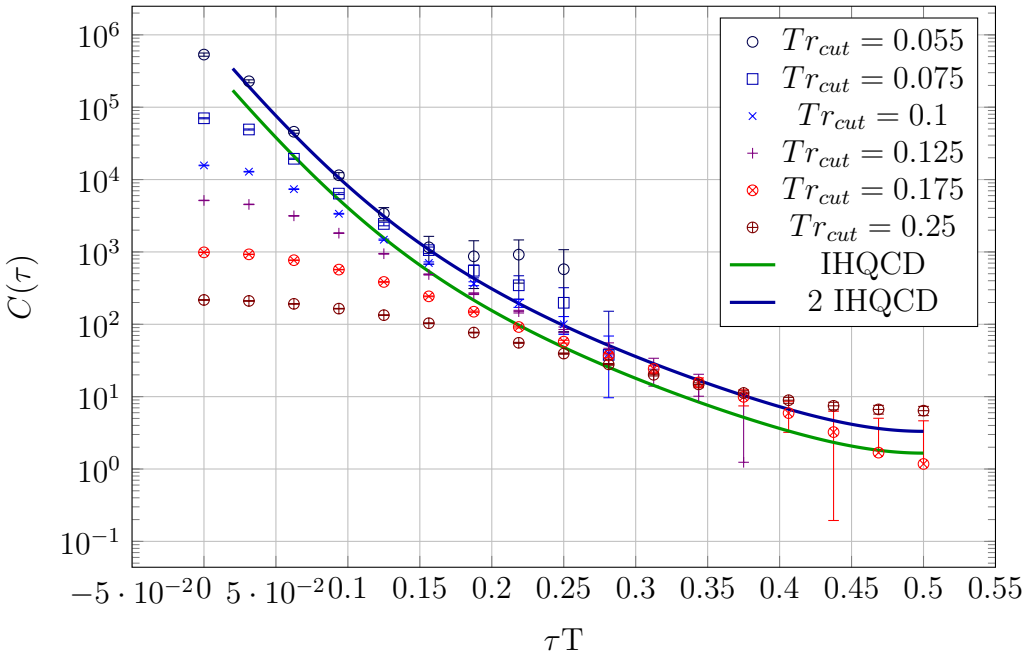

Figure 4.16: $C(\tau) = \frac{1}{T^5} \int \mathrm{d}\vec{x} \langle \Theta_{12}(0,0)\Theta_{12}(\tau,\vec{x})\rangle$, renormalized, $n_t = 32$, $T = 0.75T_c$. Errors are statistical Jackknife errors.

are correlators of the energy momentum tensor and the topological charge density. Both can be obtained from the traces of products of the field strength tensor. For a meaningful comparison, the holographic side would have to implement either something in the AdS bulk that corresponds to a lattice on the boundary or implement something in the bulk which corresponds to the Wilson flow on the boundary. Both options are not realistic in the foreseeable future, especially as the lattice side only has a conceptually very simple thing to do to provide contact with the continuum results of holography: Perform a continuum limit. But this is not without problems, too, as the signal in the correlators of the energy momentum tensor decays very fast in Euclidean time and the most interesting regime for the comparison to holography is the large distance infrared part of the correlators. Of course, one may hope that the infrared part is not strongly affected by the smearing and by the lattice spacing, such that one can go to rather large smearing radii to suppress the statistical noise.

The lattice data used here is the same as given in section 4.1 with the parameters listed in Tab. 4.3. Figs. 4.16 and 4.17 show a comparison of lattice data at a fixed lattice spacing and different smearings to the continuum holographic result in leading order in $1/N_c$ in the confined phase at $T = 0.75T_c$. Fig. 4.16 shows the correlator of the shear channel. The lattice correlator is renormalized separately for each smearing with the strategy outlined in section 2.2.1 and compared with the renormalized holographic result. For Euclidean distances in the range $0.05 \lesssim \tau T \lesssim 0.35$, the holographic correlator is off by about a factor of 2 with respect to

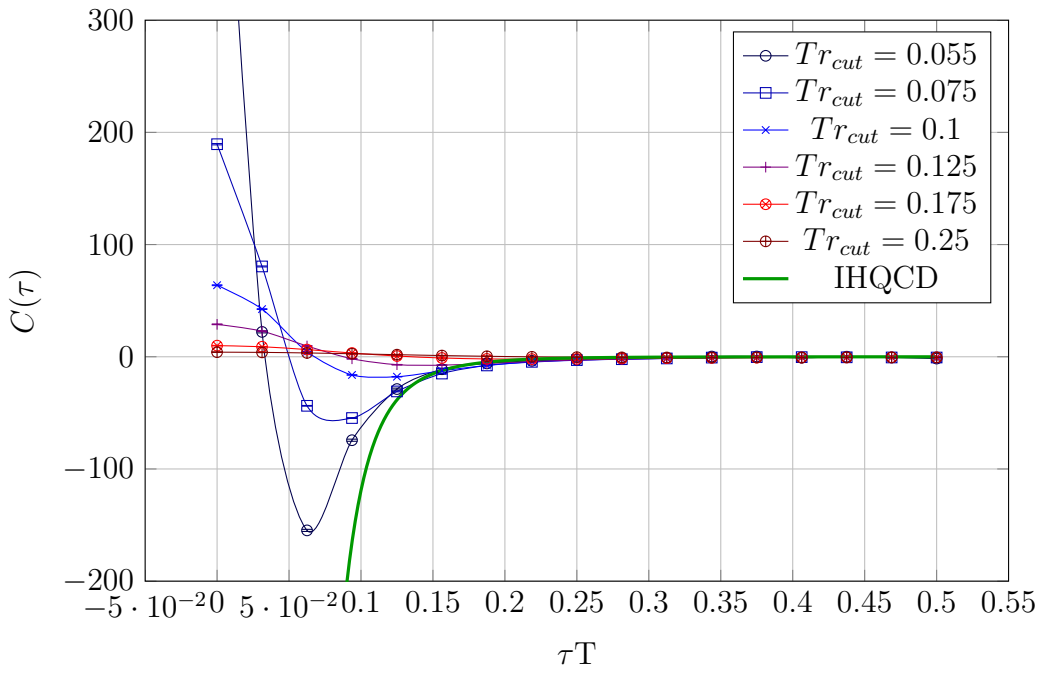

Figure 4.17: $C(\tau) = \frac{1}{T^5} \int \mathrm{d}\vec{x} \langle q(0,0) q(\tau, \vec{x}) \rangle$, unrenormalized, $n_t = 32$, $T = 0.75 T_c$. The lines between lattice data points are a smooth interpolation to guide the eye. Errors are statistical Jackknife errors.

the envelope of the lattice results for different smearings. This factor originates from a different normalization of the holographic result and is also present when one compares the perturbative $SU(3)$ result for high frequencies with the one from IHQCD. If one corrects by this factor, one sees a large region of Euclidean distances, in which the two results agree very well. Only for the largest Euclidean distances one can see a deviation between the two results.[11]

Fig. 4.17 shows the correlator of the topological charge density. For the different smearing radii on the lattice, one sees the expected behaviour also seen in e.g. [24, 52]: The region of negative values shrinks and the small τ core of positive values widens, as the smearing increases. This trend is an artefact of the increasing non-locality of the effective topological charge density operator. In the continuum result of holography, the operators are point-like and the correlator is negative for all positive Euclidean distances. This makes the (re)normalization on the holographic side difficult and the result plotted here is scaled such that it fits the lattice results for large distances.

[11] If one assumes that this result at finite lattice spacing from a combination of different smearings is consistent with the full continuum extrapolated result, one could interpret the undershoot of the holographic result with a larger low energy contribution maybe from transport contributions. That could be explained with the viscosity in the holographic setup giving the very low universal value of $1/4\pi$ in leading order in $1/N_c$. But as long as there are no fully continuum extrapolated results for the full correlator available, this remains speculative. Simulations to settle this are already planned.

At the example of the comparison of the topological charge correlators, one can see that the comparison of the correlator for shorter distances is not useful, as it is dominated by lattice artefacts. The holographic result should be most reliable in the infrared, anyway. Therefore a set of infrared quantities constructed from the correlator should be optimal for comparison. Section 3.5.3 already identified such quantities in the thermal moments of the correlators from Equ. (3.68):

$$C_T^{(n)} = \left.\frac{\mathrm{d}^n C_T}{\mathrm{d}^n(\tau T)}\right|_{\tau T=1/2} = \int_0^\infty \mathrm{d}\omega \left(\frac{\omega}{T}\right)^n \frac{A_T(\omega)}{\sinh(\omega\beta/2)}.$$

Ratios of the first few moments are especially interesting, as they are unaffected by normalization and (multiplicative) renormalization problems. To compare the region in the shear correlator at medium Euclidean distances, where the results coincide best, one can analogously define moments at $\tau T = 1/4$[12]

$$C_T^{(n)} = \left.\frac{\mathrm{d}^n C_T}{\mathrm{d}^n(\tau T)}\right|_{\tau T=1/4} = \int_0^\infty \mathrm{d}\omega \left(\frac{\omega}{T}\right)^n \frac{A_T(\omega)}{\sinh(\omega\beta/2)} \begin{cases} \cosh(\omega\beta/4), & n \text{ even} \\ \sinh(\omega\beta/4), & n \text{ odd} \end{cases}.$$

4.4 Equation of State with the Wilson flow

This section will present some results obtained in the determination of the equation of state using the Wilson flow. The corrsponding concepts were presented in the sections 2.2.2 and 2.3.5. The most important equations for this section are Equs. (2.143) and (2.148), reproduced here

$$T_{\mu\mu}(x) = \frac{1}{\alpha_E^{eff}(t)}[E(t,x) - \langle E(t,x)\rangle] + \mathcal{O}(t) \tag{4.43}$$

$$\alpha_E^{eff}(t) = \frac{w_0^4}{0.6} V_4 \left\langle E(w_0^2)(E(t) - \langle E(t)\rangle)\right\rangle. \tag{4.44}$$

It is important to note that for finite temperature studies the expectation value in Equ. (4.43) has to be understood as the zero temperature vacuum expectation value. This is enough to calculate the equation of state with a non-perturbatively determined renormalization factor α_E^{eff}.[13]

The data was generated with a modified version of the "cellsu3" pure gauge code for the QPACE machine. The parameters of the finite temperature run are

[12] At these distances both results are quite dominated by their high energy limits such that the sensitivity of such analyses might be be limited.

[13] Reference [10] also constructed the equation of state, but using a perturbatively defined α_E.

given in Tab. 4.7[14] and those for the zero temperature reference in Tab. 4.8. The action is the same as used in section 4.1.

T/T_c	n_t	n_s	β	dt	t_{max}	N_{conf}	N_{sep}	$N_{streams}$
0.8	4	16	3.94519	0.04	0.654587	138593	1	1
0.8	6	24	4.17598	0.04	1.75432	68025	7	1
0.8	8	32	4.35699	0.04	3.41784	17454	12	1
0.9	4	16	4.01265	0.04	0.915313	114307	1	1
0.9	6	24	4.24708	0.04	2.23343	53798	9	1
0.9	8	32	4.43619	0.04	4.32344	13863	15	1
1.0	4	16	4.07252	0.04	1.18596	126300	1	1
1.0	6	24	4.31466	0.04	2.77073	43384	11	1
1.0	8	32	4.50919	0.04	5.34147	11137	19	1
1.1	4	16	4.12643	0.04	1.58692	172104	2	3
1.1	6	24	4.37744	0.04	3.63497	24587	14	4
1.1	8	32	4.57803	0.04	6.47854	9226	23	1
1.2	4	16	4.17598	0.04	1.90051	154836	2	3
1.2	6	24	4.43619	0.04	3.99086	30378	16	1
1.2	8	32	4.64231	0.04	7.68675	7790	27	1
1.3	4	16	4.2236	0.04	2.06617	62344	3	1
1.3	6	24	4.49145	0.04	4.68565	25607	19	1
1.3	8	32	4.70238	0.04	8.98688	6635	32	1
1.5	4	16	4.31466	0.04	2.77073	47076	4	1
1.5	6	24	4.59452	0.04	6.25545	19100	26	1
1.5	8	32	4.81143	0.04	11.9776	4963	43	1
2.0	4	16	4.50919	0.04	4.93059	26837	7	1
2.0	6	24	4.81143	0.04	11.0563	10813	46	1
2.0	8	32	5.03746	0.04	21.423	2780	77	1

Table 4.7: Parameters of the finite temperature run for the determination of the equation of state with the Wilson flow.

In the continuum and small flow time limit, the equation of state determined with the Wilson flow should coincide with the equation of state determined with the standard procedure. Fig. 4.18 shows the continuum extrapolated equation of state determined with this completely non-perturbative procedure for three values of the Wilson flow time. While the error for $tT^2 = 0$ is rather large, it is consistent with the equation of state determined in reference [17]. This indicates that the non-perturbatively determined values for α_E^{eff} can also be used to renormalize the trace of the energy momentum tensor at zero flow time. For $tT^2 = 0.005$ the statistical errors are reduced considerably, while the result is still consistent with the reference equation of state. This is probably due to the fact that the Wilson

[14]The β values given here for a fixed temperature do not fit exactly with those cited in section 4.1. This is due to a change to a more accurate interpolation procedure for the beta function in section 4.1. Both procedures are consistent within at most about 1%.

n_t	n_s	β	dt	t_{max}	N_{conf}	N_{sep}	$N_{streams}$
16	16	3.94519	0.04	0.654587	47957	1	1
24	24	4.17598	0.04	1.75432	8688	7	4
32	32	4.35699	0.04	3.41784	11753	12	3
16	16	4.01265	0.04	0.915313	20775	1	1
24	24	4.24708	0.04	2.23343	13699	9	1
32	32	4.43619	0.04	4.32344	9348	15	3
16	16	4.07252	0.04	1.18596	26070	1	1
24	24	4.31466	0.04	2.77073	11017	11	1
32	32	4.50919	0.04	5.34147	7511	19	3
16	16	4.12643	0.04	1.46485	17743	2	1
24	24	4.37744	0.04	3.63497	7556	14	4
32	32	4.57803	0.04	6.47854	6227	23	3
16	16	4.17598	0.04	1.75432	16374	2	1
24	24	4.43619	0.04	3.99086	7716	16	1
32	32	4.64231	0.04	7.68675	5263	27	3
16	16	4.2236	0.04	2.06617	12303	3	1
24	24	4.49145	0.04	4.68565	6523	19	1
32	32	4.70238	0.04	8.98688	4483	32	3
16	16	4.31466	0.04	2.77073	9230	4	1
24	24	4.59452	0.04	6.25545	4850	26	1
32	32	4.81143	0.04	11.9776	3361	43	3
16	16	4.50919	0.04	4.93059	6930	7	1
24	24	4.81143	0.04	11.0563	2749	46	1
32	32	5.03746	0.04	21.423	1892	77	3

Table 4.8: Parameters of the zero temperature reference run for the determination of the equation of state with the Wilson flow.

flow smears out ultraviolet fluctuations, which are responsible for a large part of the error. At larger values of the flow time, e.g. at $tT^2 = 0.01$, the $\mathcal{O}(t)$ corrections in Equ. (4.43) become large, such that deviations from the reference equation of state become visible.

These results are based on a continuum extrapolation of lattices with $n_t = 4, 6, 8$ only. For a more reliable continuum extrapolation a simulation for a least $n_t = 10$ is desirable. However, this completely non-perturbatively determined equation of state does not rely on the validity of a model, such as the hadron/glueball resonance gas model for low temperatures, and therefore is an important independent crosscheck of the previous results.

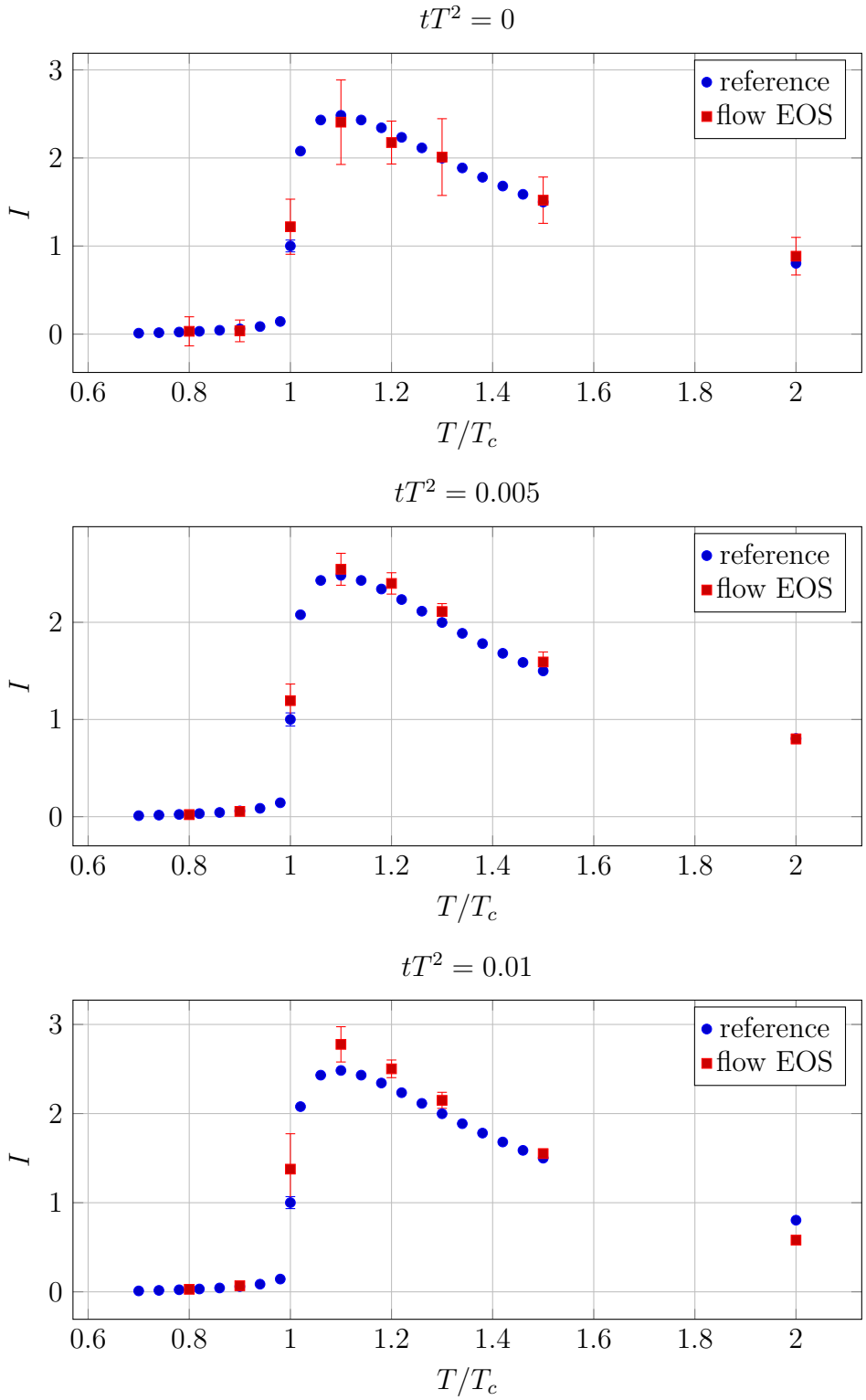

Figure 4.18: Equation of state determined non-perturbatively with the Wilson flow. The label "reference" refers to reference [17].

Chapter 5

Conclusion and Outlook

This chapter concludes the main part of the thesis by giving a summary of the most important new developments and numerical results.

The PhD project started out as an effort to determine spectral properties of hadronic bound states around and above the phase transition with dynamical fermions. This resulted in some new developments for the improvement of the reconstruction of spectral information from Euclidean correlator data. These include possible extensions of the classical effective mass analysis to reconstruct also the width of the states, which are also applicable to the Correlation Matrix Method or variational method. The project lead to the development of a way to overcome the problem of increasing numerical noise in the variational method which is introduced if one uses too many correlators in the correlation matrix. This is done by combining the generalized eigenvalue problem with a singular value decomposition. Also improvements of MEM were investigated, like the combination of CMM and MEM. For MEM, usually a lot of data points in Euclidean time are needed. This can be achieved e.g. by using anisotropic lattices which introduces the need to tune the bare anisotropy. A procedure to do this using the Wilson flow is presented. While all these efforts contributed to the two publications [20, 21], some of the activity sparked the interest in other properties of the quark gluon plasma, like transport coefficients.

A lot of important transport coefficients are related to correlators of the energy momentum tensor. Therefore, a part of the project was to work out a non-perturbative prescription to determine the renormalization coefficients of the energy momentum tensor and of its correlators. In this context, also a non-perturbative prescription for the renormalization of the trace of the energy momentum tensor using the Wilson flow has been studied and applied to perform a completely independent determination of the equation of state for pure $SU(3)$ Yang-Mills theory. The parts of the correlators of the energy momentum tensor, which are relevant for transport, are those at large Euclidean distances. They

are especially difficult to obtain sufficiently precise, because the signal in these correlators decays very fast due to the dimensionality of the energy momentum tensor.

A very interesting transport coefficient of the quark gluon plasma is the shear viscosity η. This coefficient has so far only been determined for pure Yang-Mills theory, using a noise reduction technique that is not available for dynamical simulations, the multilevel algorithm. Therefore, the Wilson flow has been explored as an alternative to reduce the statistical noise and at the same time to be more sensitive to low energy quantities by suppressing contributions of high frequencies. As the Wilson flow does not rely on locality, the proposed method also works for simulations with dynamical fermions. This method has then been tested for the quenched case and produced values for the ratio of shear viscosity over entropy density η/s, which are consistent with the values in the literature, albeit having larger errors. This analysis is published in [23].

The large errors on η/s make its determination in the dynamic case not feasible with current computational resources. The remaining difficulties come partially from the analytic continuation of the correlator to obtain the spectral function, which is needed, because η is a dynamical transport coefficient. The thermodynamic transport coefficients κ and λ_3 have also been investigated in this work, but the data were insufficient to determine the value of the coefficients. For this, much larger statistics and smaller momenta i.e. larger volumes are necessary – both requirements, which dynamical simulations currently cannot provide.

In contrast to lattice studies, analytic approaches building on the AdS/CFT duality, do not have problems with analytic continuation. Models, which aim at describing real QCD like Improved Holographic QCD, depend on non-perturbative methods to constrain their phenomenological parameters. Improved Holographic QCD currently only describes pure Yang-Mills theory. Therefore, lattice studies are the most important source of constraints. To provide some constraints, measurements of Euclidean correlators of gluonic observables can be used, like the topological charge density or the energy momentum tensor. These calculations have the potential of large synergies with quenched calculations for transport coefficients. Some comparisons between lattice simulations and holography are presented in this work. Additionally, some convenient infrared properties for the comparison have been proposed, which are insensitive to the lattice cutoff and to the current use of classical gravity on the holographic side. This is part of ongoing research and a publication is already in preparation.

Appendix A

Calculation of Wilson Flow Smeared Correlators

This appendix gives the detailed calculation of the effect of the Wilson flow on correlators of the energy momentum tensor to leading order in perturbation theory, using Equ. (2.125) of section 2.3.2.

The energy momentum tensor at finite flow time is built directly from the field strength tensor $F^t_{\mu\nu}$, which is in turn built from the $A^t_\mu(x)$

$$\Theta^t_{\mu\nu}(x) = F^t_{\mu\sigma}(x)F^t_{\nu\sigma}(x) - \frac{1}{4}\delta_{\mu\nu}F^t_{\rho\sigma}(x)F^t_{\rho\sigma}(x) \tag{A.1}$$

$$F^t_{\mu\nu}(x) = g_0\partial_\mu A^t_\nu(x) - g_0\partial_\nu A^t_\mu(x) + g_0^2[A^t_\mu(x), A^t_\nu(x)]. \tag{A.2}$$

That gives

$$\begin{aligned}
F^t_{\mu\nu}(x) &= g_0\frac{\partial}{x_\mu}\int \mathrm{d}^4y K^t(x-y)A_\nu(y) - (\mu \leftrightarrow \nu) + \mathcal{O}(g_0^2) \\
&= g_0\int \mathrm{d}^4y \left(\frac{\partial}{x_\mu}K^t(x-y)\right) A_\nu(y) - (\mu \leftrightarrow \nu) + \mathcal{O}(g_0^2) \\
&= g_0\int \mathrm{d}^4y \left(-\frac{\partial}{y_\mu}K^t(x-y)\right) A_\nu(y) - (\mu \leftrightarrow \nu) + \mathcal{O}(g_0^2) \\
&= g_0\int \mathrm{d}^4y K^t(x-y) \left(\frac{\partial}{y_\mu}A_\nu(y)\right) - (\mu \leftrightarrow \nu) + \mathcal{O}(g_0^2) \\
&= g_0\int \mathrm{d}^4y K^t(x-y) \left(\frac{\partial}{y_\mu}A_\nu(y) - (\mu \leftrightarrow \nu)\right) + \mathcal{O}(g_0^2) \\
&= \int \mathrm{d}^4y K^t(x-y)F_{\mu\nu}(y) + \mathcal{O}(g_0)
\end{aligned} \tag{A.3}$$

and

$$\begin{aligned}
\Theta^t_{\mu\nu}(x) =& F^t_{\mu\sigma}(x)F^t_{\nu\sigma}(x) - \frac{1}{4}\delta_{\mu\nu}F^t_{\rho\sigma}(x)F^t_{\rho\sigma}(x) \\
&= \int \mathrm{d}^4y K^t(x-y)F_{\mu\sigma}(y) \int \mathrm{d}^4z K^t(x-z)F_{\nu\sigma}(z) \\
&-\frac{1}{4}\delta_{\mu\nu}\int \mathrm{d}^4y K^t(x-y)F_{\rho\sigma}(y) \int \mathrm{d}^4z K^t(x-z)F_{\rho\sigma}(z) + \mathcal{O}(g_0) \\
&= \int \mathrm{d}^4y K^t(x-y) \int \mathrm{d}^4z K^t(x-z)F_{\mu\sigma}(y)F_{\nu\sigma}(z) \\
&-\frac{1}{4}\delta_{\mu\nu}\int \mathrm{d}^4y K^t(x-y) \int \mathrm{d}^4z K^t(x-z)F_{\rho\sigma}(y)F_{\rho\sigma}(z) + \mathcal{O}(g_0) \\
&= \int \mathrm{d}^4y K^t(x-y) \int \mathrm{d}^4z K^t(x-z)\Theta_{\mu\nu}(y,z) + \mathcal{O}(g_0),
\end{aligned}$$

with

$$\Theta_{\mu\nu}(y,z) = F_{\mu\sigma}(y)F_{\nu\sigma}(z) - \frac{1}{4}F_{\rho\sigma}(y)F_{\rho\sigma}(z). \tag{A.4}$$

A general zero momentum correlator of two Gaussian smeared local observables O_1 and O_2 with

$$O^t(x) = \int \mathrm{d}^4y K^t(x-y)O(y) \tag{A.5}$$

then reads

$$\begin{aligned}
C^t_{O_1,O_2}(\tau) =& \left\langle \int \mathrm{d}^3x O^t_1(\tau,\vec{x})O^t_2(0,0)\right\rangle \\
=& \frac{1}{V_4}\left\langle \int \mathrm{d}^3x \int \mathrm{d}^4x' O^t_1(\tau+x'_0,\vec{x}+\vec{x}')O^t_2(x'_0,\vec{x}')\right\rangle \\
=& \frac{1}{V_4}\left\langle \int \mathrm{d}^4x \int \mathrm{d}^4x' \delta(x_0-\tau)O^t_1(x+x')O^t_2(x')\right\rangle \qquad \text{(A.6)} \\
=& \frac{1}{V_4}\left\langle \int \mathrm{d}^4x \int \mathrm{d}^4x' \int \mathrm{d}^4y \int \mathrm{d}^4y' \delta(x_0-\tau)\right. \\
& \left. K^t(x+x'-y)O_1(y)K^t(x'-y')O_2(y')\right\rangle \\
=& \frac{1}{V_4}\left\langle \int \mathrm{d}^4x \int \mathrm{d}^4x' \int \mathrm{d}^4y \int \mathrm{d}^4y' \delta(x_0-\tau)\right. \\
& \left. K^t_3(\vec{x}+\vec{x}'-\vec{y})K^t_1(x_0+x'_0-y_0)K^t_3(\vec{x}'-\vec{y}')K^t_1(x'_0-y'_0)O_1(y)O_2(y')\right\rangle \\
=& \frac{1}{V_4}\left\langle \int \mathrm{d}x_0 \int \mathrm{d}x'_0 \int \mathrm{d}^4y \int \mathrm{d}^4y' \delta(x_0-\tau)\right. \\
& \left. K^t_1(x_0+x'_0-y_0)K^t_1(x'_0-y'_0)O_1(y)O_2(y')\right\rangle \\
=& \frac{1}{V_4}\left\langle \int \mathrm{d}x'_0 \int \mathrm{d}^4y \int \mathrm{d}^4y' K^t_1(\tau+x'_0-y_0)K^t_1(x'_0-y'_0)O_1(y)O_2(y')\right\rangle \\
=& \frac{1}{V_4}\left\langle \int \mathrm{d}^4y \int \mathrm{d}^4y' K^{2t}_1(\tau-(y_0-y'_0))O_1(y)O_2(y')\right\rangle \qquad \text{(A.7)}
\end{aligned}$$

or analogous for finite spacial momentum

$$
\begin{aligned}
C^t_{O_1,O_2}(\tau,\vec{p}) =& \left\langle \int \mathrm{d}^3x e^{i\vec{p}\cdot\vec{x}} O_1^t(\tau,\vec{x}) O_2^t(0,0) \right\rangle \\
=& \frac{1}{V_4} \left\langle \int \mathrm{d}^3x \int \mathrm{d}^4x' e^{i\vec{p}\cdot(\vec{x}+\vec{x}')} e^{-i\vec{p}\cdot\vec{x}'} O_1^t(\tau+x_0',\vec{x}+\vec{x}') O_2^t(x_0',\vec{x}') \right\rangle \\
=& \frac{1}{V_4} \left\langle \int \mathrm{d}^4x \int \mathrm{d}^4x' e^{i\vec{p}\cdot(\vec{x}+\vec{x}')} e^{-i\vec{p}\cdot\vec{x}'} \delta(x_0-\tau) O_1^t(x+x') O_2^t(x') \right\rangle \\
=& \frac{1}{V_4} \left\langle \int \mathrm{d}^4x \int \mathrm{d}^4x' \int \mathrm{d}^4y \int \mathrm{d}^4y' \delta(x_0-\tau) \right. \\
& \left. e^{i\vec{p}\cdot(\vec{x}+\vec{x}')} K^t(x+x'-y) O_1(y) e^{-i\vec{p}\cdot\vec{x}'} K^t(x'-y') O_2(y') \right\rangle \\
=& \frac{1}{V_4} \left\langle \int \mathrm{d}x_0 \int \mathrm{d}x_0' \int \mathrm{d}^4y \int \mathrm{d}^4y' \delta(x_0-\tau) e^{-\vec{p}\cdot(\vec{p}t-i\vec{y})} e^{-\vec{p}\cdot(\vec{p}t+i\vec{y}')} \right. \\
& \left. K_1^t(x_0+x_0'-y_0) K_1^t(x_0'-y_0') O_1(y) O_2(y') \right\rangle \\
=& \frac{1}{V_4} \left\langle \int \mathrm{d}x_0' \int \mathrm{d}^4y \int \mathrm{d}^4y' e^{-\vec{p}\cdot(\vec{p}t-i\vec{y})} e^{-\vec{p}\cdot(\vec{p}t+i\vec{y}')} \right. \\
& \left. K_1^t(\tau+x_0'-y_0) K_1^t(x_0'-y_0') O_1(y) O_2(y') \right\rangle \\
=& \frac{1}{V_4} e^{-2t\vec{p}^2} \left\langle \int \mathrm{d}^4y \int \mathrm{d}^4y' e^{i\vec{p}\cdot\vec{y}} e^{-i\vec{p}\cdot\vec{y}'} K_1^{2t}(\tau-(y_0'-y_0)) O_1(y) O_2(y') \right\rangle \\
=& TV_3 e^{-2t\vec{p}^2} \left\langle \int \mathrm{d}y_0 \int \mathrm{d}y_0' K_1^{2t}(\tau-(y_0'-y_0)) O_1(y_0,\vec{p}) O_2(y_0',-\vec{p}) \right\rangle \qquad \text{(A.8)} \\
=& TV_3 e^{-2t\vec{p}^2} \left\langle \int \mathrm{d}y_0 \int \mathrm{d}y_0' K_1^{2t}(\tau-y_0') O_1(y_0,\vec{p}) O_2(y_0'+y_0,-\vec{p}) \right\rangle \\
=& TV_3 e^{-2t\vec{p}^2} \left\langle \int \mathrm{d}y_0 \int \mathrm{d}y_0' K_1^{2t}(\tau-y_0') O_1(0,\vec{p}) O_2(y_0',-\vec{p}) \right\rangle \\
=& V_3 e^{-2t\vec{p}^2} \left\langle \int \mathrm{d}y_0' K_1^{2t}(\tau-y_0') O_1(0,\vec{p}) O_2(y_0',-\vec{p}) \right\rangle \\
=& V_3 e^{-2t\vec{p}^2} \int \mathrm{d}y_0' K_1^{2t}(\tau-y_0') \left\langle O_1(0,\vec{p}) O_2(y_0',-\vec{p}) \right\rangle \\
=& e^{-2t\vec{p}^2} \int \mathrm{d}y_0' K_1^{2t}(\tau-y_0') C_{O_1,O_2}(y_0',\vec{p}) \qquad \text{(A.9)} \\
=& e^{-2t\vec{p}^2} \int \mathrm{d}y_0' K_1^{2t}(\tau-y_0') \int \mathrm{d}\omega K(\omega,y_0') \rho_{O_1,O_2}(\omega,\vec{p})
\end{aligned}
$$

using

$$K_n^t(x) = \frac{e^{-x^2/4t}}{(4\pi t)^{n/2}} \qquad \text{(A.10)}$$

$$\int \mathrm{d}^n x K_n^{t_1}(x-y) K_n^{t_2}(x-z) = K_n^{t_1+t_2}(y-z) \qquad \text{(A.11)}$$

$$K_n^{2t}(\sqrt{2}x) = K_n^t(x) \frac{1}{(2)^{n/2}} \qquad \text{(A.12)}$$

$$K_1^t(z) K_1^t(\tau+z) = K_1^{2t}(2z+\tau) K_1^{t/2}(\tau/2) \qquad \text{(A.13)}$$

$$\int \mathrm{d}x K_1^t(x+y) e^{ipx} = e^{-p(pt+iy)} \qquad \text{(A.14)}$$

$$O(x_0,\vec{p}) = \frac{1}{V_3} \int \mathrm{d}^3x e^{i\vec{p}\cdot\vec{x}} O(x). \qquad \text{(A.15)}$$

A general zero momentum correlator of two Gaussian smeared products O_1 and O_2 of local observables with

$$O^t(x) = \int \mathrm{d}^4 y K^t(x-y) \int \mathrm{d}^4 z K^t(x-z) O(y,z) \tag{A.16}$$

then reads

$$\begin{aligned}
C^t_{O_1,O_2}(\tau) =& \left\langle \int \mathrm{d}^3 x O_1^t(\tau,\vec{x}) O_2^t(0,0) \right\rangle \\
=& \frac{1}{V_4} \left\langle \int \mathrm{d}^3 x \int \mathrm{d}^4 x' O_1^t(\tau + x_0', \vec{x} + \vec{x}') O_2^t(x_0', \vec{x}') \right\rangle \\
=& \frac{1}{V_4} \left\langle \int \mathrm{d}^4 x \int \mathrm{d}^4 x' \delta(x_0 - \tau) O_1^t(x + x') O_2^t(x') \right\rangle \\
=& \frac{1}{V_4} \Big\langle \int \mathrm{d}^4 x \int \mathrm{d}^4 x' \int \mathrm{d}^4 y \int \mathrm{d}^4 y' \int \mathrm{d}^4 z \int \mathrm{d}^4 z' \delta(x_0 - \tau) \\
& K^t(x + x' - y) K^t(x' - y') K^t(x + x' - z) K^t(x' - z') O_1(y,z) O_2(y',z') \Big\rangle \\
=& \frac{1}{V_4} \Big\langle \int \mathrm{d} x_0 \int \mathrm{d} x_0' \int \mathrm{d}^4 y \int \mathrm{d}^4 y' \int \mathrm{d}^4 z \int \mathrm{d}^4 z' \delta(x_0 - \tau) \\
& K_1^t(x_0 + x_0' - y_0) K_1^t(x_0' - y_0') K_1^t(x_0 + x_0' - z_0) K_1^t(x_0' - z_0') \\
& K_3^{2t}(\vec{y} - \vec{z}) K_3^{2t}(\vec{y}' - \vec{z}') O_1(y,z) O_2(y',z') \Big\rangle \\
=& \frac{1}{V_4} \Big\langle \int \mathrm{d}^4 y \int \mathrm{d}^4 y' \int \mathrm{d}^4 z \int \mathrm{d}^4 z' K_1^t(\tau - (y_0 - y_0' + z_0 - z_0')/2) \\
& K^{2t}(y - z) K^{2t}(y' - z') O_1(y,z) O_2(y',z') \Big\rangle \\
=& \frac{1}{V_4} \Big\langle \int \mathrm{d}^4 x \int \mathrm{d}^4 x' \int \mathrm{d}^4 \delta x \int \mathrm{d}^4 \delta x' K_1^t(\tau - (x_0 - x_0')) \\
& K^{2t}(\delta x) K^{2t}(\delta x') O_1\left(x + \frac{\delta x}{2}, x - \frac{\delta x}{2}\right) O_2\left(x' + \frac{\delta x'}{2}, x' - \frac{\delta x'}{2}\right) \Big\rangle \\
=& \frac{1}{V_4} \left\langle \int \mathrm{d}^4 x \int \mathrm{d}^4 x' K_1^t(\tau - (x_0 - x_0')) \breve{O}_1^t(x) \breve{O}_2^t(x') \right\rangle
\end{aligned} \tag{A.17}$$

using

$$\begin{aligned}
\int \mathrm{d} x_0' K_1^t(x_0 + x_0' - y_0) K_1^t(x_0 + x_0' - z_0) K_1^t(x_0' - y_0') K_1^t(x_0' - z_0') = \\
K_1^t(x_0 - (y_0 - y_0' + z_0 - z_0')/2) K_1^{2t}(y_0 - z_0) K_1^{2t}(y_0' - z_0')
\end{aligned} \tag{A.18}$$

with

$$\breve{O}^t(x) = \int \mathrm{d}^4 \delta x K^{2t}(\delta x) O\left(x + \frac{\delta x}{2}, x - \frac{\delta x}{2}\right) \tag{A.19}$$

$$= O(x) + 2t\, \partial_{\delta x}^2 O\left(x + \frac{\delta x}{2}, x - \frac{\delta x}{2}\right)\Big|_{\delta x = 0} + \mathcal{O}(t^2) \tag{A.20}$$

by series expansion of O in δx. Additionally, one can derive an exact relation for

the higher orders. As the Gaussian kernel K factorizes for the directions and for a single variable

$$\int \mathrm{d}x K^t(x) f(x) = \left(e^{t\partial^2} f\right)(0), \tag{A.21}$$

it can be also shown that

$$\breve{O}^t(x) = e^{2t\partial^2_{\delta x}} O\left(x + \frac{\delta x}{2}, x - \frac{\delta x}{2}\right)\Bigg|_{\delta x = 0}. \tag{A.22}$$

This is basically a reformulation of the smearing statement: With increasing flow time the operator becomes less local.

For finite spatial momentum, this gives

$$
\begin{aligned}
C^t_{O_1,O_2}(\tau,\vec{p}) =& \left\langle \int \mathrm{d}^3x e^{i\vec{p}\cdot\vec{x}} O_1^t(\tau,\vec{x}) O_2^t(0,0) \right\rangle \\
=& \frac{1}{V_4} \left\langle \int \mathrm{d}^3x \int \mathrm{d}^4x' e^{i\vec{p}\cdot(\vec{x}+\vec{x}')} e^{-i\vec{p}\cdot\vec{x}'} O_1^t(\tau+x_0',\vec{x}+\vec{x}') O_2^t(x_0',\vec{x}') \right\rangle \\
=& \frac{1}{V_4} \left\langle \int \mathrm{d}^4x \int \mathrm{d}^4x' e^{i\vec{p}\cdot(\vec{x}+\vec{x}')} e^{-i\vec{p}\cdot\vec{x}'} \delta(x_0-\tau) O_1^t(x+x') O_2^t(x') \right\rangle \\
=& \frac{1}{V_4} \left\langle \int \mathrm{d}^4x \int \mathrm{d}^4x' \int \mathrm{d}^4y \int \mathrm{d}^4y' \int \mathrm{d}^4z \int \mathrm{d}^4z' \delta(x_0-\tau) e^{i\vec{p}\cdot(\vec{x}+\vec{x}')} e^{-i\vec{p}\cdot\vec{x}'} \right. \\
& \left. K^t(x+x'-y) K^t(x'-y') K^t(x+x'-z) K^t(x'-z') O_1(y,z) O_2(y',z') \right\rangle \\
=& \frac{1}{V_4} e^{-t\vec{p}^2} \left\langle \int \mathrm{d}x_0 \int \mathrm{d}x_0' \int \mathrm{d}^4y \int \mathrm{d}^4y' \int \mathrm{d}^4z \int \mathrm{d}^4z' \delta(x_0-\tau) \right. \\
& K_1^t(x_0+x_0'-y_0) K_1^t(x_0'-y_0') K_1^t(x_0+x_0'-z_0) K_1^t(x_0'-z_0') \\
& \left. K_3^{2t}(\vec{y}-\vec{z}) K_3^{2t}(\vec{y}'-\vec{z}') e^{i\frac{1}{2}\vec{p}\cdot(\vec{y}+\vec{z})} e^{-i\frac{1}{2}\vec{p}\cdot(\vec{y}'+\vec{z}')} O_1(y,z) O_2(y',z') \right\rangle \\
=& \frac{1}{V_4} e^{-t\vec{p}^2} \left\langle \int \mathrm{d}^4y \int \mathrm{d}^4y' \int \mathrm{d}^4z \int \mathrm{d}^4z' K_1^t(\tau-(y_0-y_0'+z_0-z_0')/2) \right. \\
& \left. K^{2t}(y-z) K^{2t}(y'-z') e^{i\frac{1}{2}\vec{p}\cdot(\vec{y}+\vec{z})} e^{-i\frac{1}{2}\vec{p}\cdot(\vec{y}'+\vec{z}')} O_1(y,z) O_2(y',z') \right\rangle \\
=& \frac{1}{V_4} e^{-t\vec{p}^2} \left\langle \int \mathrm{d}^4x \int \mathrm{d}^4x' \int \mathrm{d}^4\delta x \int \mathrm{d}^4 K_1^t(\tau-(x_0-x_0'))\delta x' e^{i\vec{p}\cdot\vec{x}} e^{-i\vec{p}\cdot\vec{x}'} \right. \\
& \left. K^{2t}(\delta x) K^{2t}(\delta x') O_1\left(x+\frac{\delta x}{2}, x-\frac{\delta x}{2}\right) O_2\left(x'+\frac{\delta x'}{2}, x'-\frac{\delta x'}{2}\right) \right\rangle \\
=& \frac{1}{V_4} e^{-t\vec{p}^2} \left\langle \int \mathrm{d}^4x \int \mathrm{d}^4x' K_1^t(\tau-(x_0-x_0')) e^{i\vec{p}\cdot\vec{x}} e^{-i\vec{p}\cdot\vec{x}'} \breve{O}_1^t(x) \breve{O}_2^t(x') \right\rangle \\
=& T V_3 e^{-t\vec{p}^2} \left\langle \int \mathrm{d}x_0 \int \mathrm{d}x_0' K_1^t(\tau-(x_0-x_0')) \breve{O}_1^t(x_0,\vec{p}) \breve{O}_2^t(x_0',-\vec{p}) \right\rangle \\
=& T V_3 e^{-t\vec{p}^2} \left\langle \int \mathrm{d}x_0 \int \mathrm{d}x_0' K_1^t(\tau-(x_0-x_0')) O_1(x_0,\vec{p}) O_2(x_0',-\vec{p}) \right\rangle + \mathcal{O}(t)
\end{aligned}
\tag{A.23}
$$

$$
\begin{aligned}
=& T V_3 e^{-t\vec{p}^2} \left\langle \int \mathrm{d}x_0 \int \mathrm{d}x_0' K_1^t(\tau-x_0) O_1(x_0+x_0',\vec{p}) O_2(x_0',-\vec{p}) \right\rangle + \mathcal{O}(t) \\
=& T V_3 e^{-t\vec{p}^2} \left\langle \int \mathrm{d}x_0 \int \mathrm{d}x_0' K_1^t(\tau-x_0) O_1(x_0,\vec{p}) O_2(0,-\vec{p}) \right\rangle + \mathcal{O}(t) \\
=& V_3 e^{-t\vec{p}^2} \left\langle \int \mathrm{d}x_0 K_1^t(\tau-x_0) O_1(x_0,\vec{p}) O_2(0,-\vec{p}) \right\rangle + \mathcal{O}(t) \\
=& e^{-t\vec{p}^2} \int \mathrm{d}x_0 K_1^t(\tau-x_0) C_{O_1,O_2}(x_0,\vec{p}) + \mathcal{O}(t) \\
=& e^{-t\vec{p}^2} \int \mathrm{d}x_0 K_1^t(\tau-x_0) \int \mathrm{d}\omega K(\omega,x_0) \rho_{O_1,O_2}(\omega,\vec{p}) + \mathcal{O}(t)
\end{aligned}
$$

using

$$
\int \mathrm{d}^n x K_n^t(x-y) K_n^t(x-z) e^{ipx} = K_n^{2t}(y-z) e^{\frac{1}{2}p(-pt+i(y+z))}. \tag{A.24}
$$

Note that Equ. (A.8) for a correlator of a smeared local operator and Equ.

(A.23) for a correlator of a product of two smeared local operators is the same apart from a replacement of the flow time $t \to t/2$ for the case of the product.

Apart from 2-point correlators also integrated 3-point correlators with the same operators

$$O^t(x) = \int \mathrm{d}^4 y K^t(x-y) \int \mathrm{d}^4 z K^t(x-z) O(y,z) \tag{A.25}$$

are of interest for this thesis. For finite momentum, they read

$$
\begin{aligned}
C^t_{O_1,O_2,O_3}(p,q) =& \left\langle \int \mathrm{d}^4x e^{ipx} O_1^t(x) \int \mathrm{d}^4y e^{iqy} O_2^t(y) O_3^t(0) \right\rangle \\
=& \frac{1}{V_4} \left\langle \int \mathrm{d}^4x \int \mathrm{d}^4x' \int \mathrm{d}^4x'' e^{ip(x+x'')} e^{iq(x'+x'')} e^{-i(p+q)x''} \right. \\
& \left. O_1^t(x+x'') O_2^t(x'+x'') O_3^t(x'') \right\rangle \\
=& \frac{1}{V_4} \left\langle \int \mathrm{d}^4x \int \mathrm{d}^4x' \int \mathrm{d}^4x'' e^{ip(x)} e^{iq(x')} e^{-i(p+q)x''} \right. \\
& \left. O_1^t(x) O_2^t(x) O_3^t(x'') \right\rangle \\
=& \frac{1}{V_4} \left\langle \int \mathrm{d}^4x \int \mathrm{d}^4y \int \mathrm{d}^4z \int \mathrm{d}^4x' \int \mathrm{d}^4y' \int \mathrm{d}^4z' \int \mathrm{d}^4x'' \int \mathrm{d}^4y'' \int \mathrm{d}^4z'' \right. \\
& e^{ipx} e^{iqx'} e^{-i(p+q)x''} K^t(x-y) K^t(x-z) \\
& K^t(x'-y') K^t(x'-z') K^t(x''-y'') K^t(x''-z'') \\
& \left. O_1(y,z) O_2(y',z') O_3(y'',z'') \right\rangle \\
=& \frac{1}{V_4} \left\langle \int \mathrm{d}^4y \int \mathrm{d}^4z \int \mathrm{d}^4y' \int \mathrm{d}^4z' \int \mathrm{d}^4y'' \int \mathrm{d}^4z'' \right. \\
& K_n^{2t}(y-z) e^{\frac{1}{2}p(-pt+i(y+z))} O_1(y,z) \\
& K_n^{2t}(y'-z') e^{\frac{1}{2}q(-qt+i(y'+z'))} O_2(y',z') \\
& \left. K_n^{2t}(y''-z'') e^{\frac{1}{2}(p+q)(-(p+q)t+i(y''+z''))} O_3(y'',z'') \right\rangle \\
=& \frac{1}{V_4} e^{-\frac{1}{2}(p^2+q^2+(p+q)^2)t} \left\langle \int \mathrm{d}^4y \int \mathrm{d}^4z \int \mathrm{d}^4y' \int \mathrm{d}^4z' \int \mathrm{d}^4y'' \int \mathrm{d}^4z'' \right. \\
& K_n^{2t}(y-z) e^{\frac{1}{2}p(-pt+i(y+z))} O_1(y,z) \\
& K_n^{2t}(y'-z') e^{\frac{1}{2}q(-qt+i(y'+z'))} O_2(y',z') \\
& \left. K_n^{2t}(y''-z'') e^{\frac{1}{2}(p+q)(-(p+q)t+i(y''+z''))} O_3(y'',z'') \right\rangle \\
=& \frac{1}{V_4} e^{-\frac{1}{2}(p^2+q^2+(p+q)^2)t} \left\langle \int \mathrm{d}^4x \int \mathrm{d}^4\delta x \int \mathrm{d}^4x' \int \mathrm{d}^4\delta x' \int \mathrm{d}^4x'' \int \mathrm{d}^4\delta x'' \right. \\
& K_n^{2t}(\delta x) e^{ipx} O_1\left(x + \frac{\delta x}{2}, x - \frac{\delta x}{2}\right) \\
& K_n^{2t}(\delta x') e^{iqx'} O_2\left(x' + \frac{\delta x'}{2}, x' - \frac{\delta x'}{2}\right) \\
& \left. K_n^{2t}(\delta x'') e^{i(p+q)x''} O_3\left(x'' + \frac{\delta x''}{2}, x'' - \frac{\delta x''}{2}\right) \right\rangle \\
=& \frac{1}{V_4} e^{-\frac{1}{2}(p^2+q^2+(p+q)^2)t} \left\langle \int \mathrm{d}^4x \int \mathrm{d}^4x' \int \mathrm{d}^4x'' \right. \\
& \left. e^{ipx} \breve{O}_1(x) e^{iqx'} \breve{O}_2(x') e^{i(p+q)x''} \breve{O}_3(x'') \right\rangle \\
=& V_4^2 e^{-\frac{1}{2}(p^2+q^2+(p+q)^2)t} \left\langle \breve{O}_1(p) \breve{O}_2(q) \breve{O}_3(p+q) \right\rangle .
\end{aligned}
$$

References

[1] ATLAS Collaboration, Georges Aad et al. Observation of a new particle in the search for the Standard Model Higgs boson with the ATLAS detector at the LHC. *Phys.Lett.*, B716:1–29, 2012, 1207.7214. doi: 10.1016/j.physletb.2012.08.020.

[2] G. Aarts, C. Allton, S. Kim, M.P. Lombardo, M.B. Oktay, et al. What happens to the Upsilon and eta_b in the quark-gluon plasma? Bottomonium spectral functions from lattice QCD. *JHEP*, 1111:103, 2011, 1109.4496. doi: 10.1007/JHEP11(2011)103.

[3] Gert Aarts and Jose Maria Martinez Resco. Transport coefficients, spectral functions and the lattice. *JHEP*, 0204:053, 2002, hep-ph/0203177. doi: 10.1088/1126-6708/2002/04/053.

[4] Gert Aarts, Chris Allton, Justin Foley, Simon Hands, and Seyong Kim. Spectral functions at small energies and the electrical conductivity in hot, quenched lattice QCD. *Phys.Rev.Lett.*, 99:022002, 2007, hep-lat/0703008. doi: 10.1103/PhysRevLett.99.022002.

[5] ALICE Collaboration, Betty Abelev et al. J/ψ suppression at forward rapidity in Pb-Pb collisions at $\sqrt{s_{NN}} = 2.76$ TeV. *Phys.Rev.Lett.*, 109:072301, 2012, 1202.1383. doi: 10.1103/PhysRevLett.109.072301.

[6] PHENIX Collaboration, A. Adare et al. J/ψ suppression at forward rapidity in Au+Au collisions at $\sqrt{s_{NN}} = 200$ GeV. *Phys.Rev.*, C84:054912, 2011, 1103.6269. doi: 10.1103/PhysRevC.84.054912.

[7] Ofer Aharony, Steven S. Gubser, Juan Martin Maldacena, Hirosi Ooguri, and Yaron Oz. Large N field theories, string theory and gravity. *Phys.Rept.*, 323:183–386, 2000, hep-th/9905111. doi: 10.1016/S0370-1573(99)00083-6.

[8] B. Alles, Massimo D'Elia, and A. Di Giacomo. Topology at zero and finite T in SU(2) Yang-Mills theory. *Phys.Lett.*, B412:119–124, 1997, hep-lat/9706016. doi: 10.1016/S0370-2693(97)01059-9.

[9] M. Asakawa, T. Hatsuda, and Y. Nakahara. Maximum entropy analysis of the spectral functions in lattice QCD. *Prog.Part.Nucl.Phys.*, 46:459–508, 2001, hep-lat/0011040. doi: 10.1016/S0146-6410(01)00150-8.

[10] FlowQCD Collaboration, Masayuki Asakawa, Tetsuo Hatsuda, Etsuko Itou, Masakiyo Kitazawa, and Hiroshi Suzuki. Thermodynamics of SU(3) gauge theory from gradient flow on the lattice. *Phys.Rev.*, D90(1):011501, 2014, 1312.7492. doi: 10.1103/PhysRevD.90.011501.

[11] H. Baier, H. Boettiger, M. Drochner, N. Eicker, U. Fischer, et al. QPACE: A QCD parallel computer based on Cell processors. *PoS*, LAT2009:001, 2009, 0911.2174.

[12] Rudolf Baier, Paul Romatschke, Dam Thanh Son, Andrei O. Starinets, and Mikhail A. Stephanov. Relativistic viscous hydrodynamics, conformal invariance, and holography. *JHEP*, 0804:100, 2008, 0712.2451. doi: 10.1088/1126-6708/2008/04/100.

[13] G.S. Bali, F. Bruckmann, G. Endrodi, and A. Schafer. Paramagnetic squeezing of QCD matter. *Phys.Rev.Lett.*, 112:042301, 2014, 1311.2559. doi: 10.1103/PhysRevLett.112.042301.

[14] Michel Le Bellac. *Thermal Field Theory*. Cambridge University Press, 2000.

[15] Sayantani Bhattacharyya. Constraints on the second order transport coefficients of an uncharged fluid. *JHEP*, 1207:104, 2012, 1201.4654. doi: 10.1007/JHEP07(2012)104.

[16] Jean-Paul Blaizot and Edmond Iancu. The Quark gluon plasma: Collective dynamics and hard thermal loops. *Phys.Rept.*, 359:355–528, 2002, hep-ph/0101103. doi: 10.1016/S0370-1573(01)00061-8.

[17] Sz. Borsanyi, G. Endrodi, Z. Fodor, S.D. Katz, and K.K. Szabo. Precision SU(3) lattice thermodynamics for a large temperature range. *JHEP*, 1207: 056, 2012, 1204.6184. doi: 10.1007/JHEP07(2012)056.

[18] Szabocls Borsanyi, Zoltan Fodor, Christian Hoelbling, Sandor D. Katz, Stefan Krieg, et al. Full result for the QCD equation of state with 2+1 flavors. *Phys.Lett.*, B730:99–104, 2014, 1309.5258. doi: 10.1016/j.physletb.2014.01.007.

[19] Szabolcs Borsanyi, Stephan Durr, Zoltan Fodor, Christian Hoelbling, Sandor D. Katz, et al. High-precision scale setting in lattice QCD. *JHEP*, 1209: 010, 2012, 1203.4469. doi: 10.1007/JHEP09(2012)010.

[20] Szabolcs Borsanyi, Stephan Durr, Zoltan Fodor, Sandor D. Katz, Stefan Krieg, et al. Anisotropy tuning with the Wilson flow. 2012, 1205.0781.

[21] Szabolcs Borsanyi, Stephan Dürr, Zoltan Fodor, Christian Hoelbling, Sandor D. Katz, et al. Charmonium spectral functions from 2+1 flavour lattice QCD. *JHEP*, 1404:132, 2014, 1401.5940. doi: 10.1007/JHEP04(2014)132.

[22] Szabolcs Borsanyi, Zoltan Fodor, Christian Hoelbling, Sandor D. Katz, Stefan Krieg, et al. Recent results on the Equation of State of QCD. 2014, 1410.7917.

[23] Szabolcs Borsanyi, Zoltan Fodor, Simon Mages, Andreas Schäfer, and Kalman Szabo. Shear Viscosity from Lattice QCD. *PoS*, LATTICE2014, 2014.

[24] Falk Bruckmann, Florian Gruber, Nigel Cundy, Andreas Schafer, and Thomas Lippert. Topology of dynamical lattice configurations including results from dynamical overlap fermions. *Phys.Lett.*, B707:278–285, 2012, 1107.0897. doi: 10.1016/j.physletb.2011.12.030.

[25] Tommy Burch, Christof Gattringer, Leonid Ya. Glozman, Christian Hagen, Dieter Hierl, et al. Excited hadrons on the lattice: Baryons. *Phys.Rev.*, D74: 014504, 2006, hep-lat/0604019. doi: 10.1103/PhysRevD.74.014504.

[26] Tommy Burch, Christof Gattringer, Leonid Ya. Glozman, Christian Hagen, C.B. Lang, et al. Excited hadrons on the lattice: Mesons. *Phys.Rev.*, D73: 094505, 2006, hep-lat/0601026. doi: 10.1103/PhysRevD.73.094505.

[27] CMS Collaboration, Serguei Chatrchyan et al. Suppression of non-prompt J/ψ, prompt J/ψ, and Y(1S) in PbPb collisions at $\sqrt{s_{NN}} = 2.76$ TeV. *JHEP*, 1205:063, 2012, 1201.5069. doi: 10.1007/JHEP05(2012)063.

[28] CMS Collaboration, Serguei Chatrchyan et al. Observation of a new boson at a mass of 125 GeV with the CMS experiment at the LHC. *Phys.Lett.*, B716: 30–61, 2012, 1207.7235. doi: 10.1016/j.physletb.2012.08.021.

[29] Saumen Datta and Peter Petreczky. Zero mode contribution in quarkonium correlators and in-medium properties of heavy quarks. *J.Phys.*, G35:104114, 2008, 0805.1174. doi: 10.1088/0954-3899/35/10/104114.

[30] Saumen Datta, Frithjof Karsch, Peter Petreczky, and Ines Wetzorke. Behavior of charmonium systems after deconfinement. *Phys.Rev.*, D69:094507, 2004, hep-lat/0312037. doi: 10.1103/PhysRevD.69.094507.

[31] Luigi Del Debbio, Agostino Patella, and Antonio Rago. Space-time symmetries and the Yang-Mills gradient flow. *JHEP*, 1311:212, 2013, 1306.1173. doi: 10.1007/JHEP11(2013)212.

[32] H.-T. Ding, A. Francis, O. Kaczmarek, H. Satz, F. Karsch, et al. Charmonium correlation and spectral functions at finite temperature. *PoS*, LATTICE2010: 180, 2010, 1011.0695.

[33] H.-T. Ding, A. Francis, O. Kaczmarek, F. Karsch, E. Laermann, et al. Thermal dilepton rate and electrical conductivity: An analysis of vector current correlation functions in quenched lattice QCD. *Phys.Rev.*, D83:034504, 2011, 1012.4963. doi: 10.1103/PhysRevD.83.034504.

[34] H.-T. Ding, A. Francis, O. Kaczmarek, F. Karsch, H. Satz, et al. Charmonium dissociation and heavy quark transport in hot quenched lattice QCD. *EPJ Web Conf.*, 70:00061, 2014, 1210.0292. doi: 10.1051/epjconf/20147000061.

[35] H.T. Ding, A. Francis, O. Kaczmarek, F. Karsch, H. Satz, et al. Charmonium properties in hot quenched lattice QCD. *Phys.Rev.*, D86:014509, 2012, 1204.4945. doi: 10.1103/PhysRevD.86.014509.

[36] Michael R. Douglas. The Statistics of string / M theory vacua. *JHEP*, 0305: 046, 2003, hep-th/0303194. doi: 10.1088/1126-6708/2003/05/046.

[37] J. Engels and O. Vogt. Longitudinal and transverse spectral functions in the three-dimensional O(4) model. *Nucl.Phys.*, B832:538–566, 2010, 0911.1939. doi: 10.1016/j.nuclphysb.2010.02.006.

[38] J. Engels, J. Fingberg, F. Karsch, D. Miller, and M. Weber. Nonperturbative thermodynamics of SU(N) gauge theories. *Phys.Lett.*, B252:625–630, 1990. doi: 10.1016/0370-2693(90)90496-S.

[39] Z. Fodor and S.D. Katz. A New method to study lattice QCD at finite temperature and chemical potential. *Phys.Lett.*, B534:87–92, 2002, hep-lat/0104001. doi: 10.1016/S0370-2693(02)01583-6.

[40] Z. Fodor and S.D. Katz. The Phase diagram of quantum chromodynamics. 2009, 0908.3341.

[41] A. Frommer, K. Kahl, S. Krieg, B. Leder, and M. Rottmann. An adaptive aggregation based domain decomposition multilevel method for the lattice wilson dirac operator: multilevel results. 2013, 1307.6101.

[42] Andreas Frommer, Karsten Kahl, Stefan Krieg, Björn Leder, and Matthias Rottmann. Adaptive Aggregation Based Domain Decomposition Multigrid for the Lattice Wilson Dirac Operator. *SIAM J.Sci.Comput.*, 36:A1581–A1608, 2014, 1303.1377. doi: 10.1137/130919507.

[43] Charles Gale, Sangyong Jeon, Bjorn Schenke, Prithwish Tribedy, and Raju Venugopalan. Event-by-event anisotropic flow in heavy-ion collisions from combined Yang-Mills and viscous fluid dynamics. *Phys.Rev.Lett.*, 110:012302, 2013, 1209.6330. doi: 10.1103/PhysRevLett.110.012302.

[44] Christof Gattringer and Christian B. Lang. *Quantum Chromodynamics on the Lattice: An Introductory Presentation*, volume 788 of *Lecture Notes in Physics*. Springer, 2010.

[45] S.L. Glashow. Partial Symmetries of Weak Interactions. *Nucl.Phys.*, 22: 579–588, 1961. doi: 10.1016/0029-5582(61)90469-2.

[46] U. Gürsoy, I. Iatrakis, E. Kiritsis, F. Nitti, and A. O'Bannon. The Chern-Simons Diffusion Rate in Improved Holographic QCD. *JHEP*, 1302:119, 2013, 1212.3894. doi: 10.1007/JHEP02(2013)119.

[47] U. Gursoy and E. Kiritsis. Exploring improved holographic theories for QCD: Part I. *JHEP*, 0802:032, 2008, 0707.1324. doi: 10.1088/1126-6708/2008/02/032.

[48] U. Gursoy, E. Kiritsis, and F. Nitti. Exploring improved holographic theories for QCD: Part II. *JHEP*, 0802:019, 2008, 0707.1349. doi: 10.1088/1126-6708/2008/02/019.

[49] U. Gursoy, E. Kiritsis, L. Mazzanti, and F. Nitti. Improved Holographic Yang-Mills at Finite Temperature: Comparison with Data. *Nucl.Phys.*, B820: 148–177, 2009, 0903.2859. doi: 10.1016/j.nuclphysb.2009.05.017.

[50] Michael Haas, Leonard Fister, and Jan M. Pawlowski. Gluon spectral functions and transport coefficients in Yang–Mills theory. *Phys.Rev.*, D90(9): 091501, 2014, 1308.4960. doi: 10.1103/PhysRevD.90.091501.

[51] A. Ikeda, M. Asakawa, and M. Kitazawa. Charmonium spectra and dispersion relation with improved Bayesian analysis in lattice QCD. 2014, 1412.0357.

[52] E.-M. Ilgenfritz, D. Leinweber, P. Moran, K. Koller, G. Schierholz, et al. Vacuum structure revealed by over-improved stout-link smearing compared with the overlap analysis for quenched QCD. *Phys.Rev.*, D77:074502, 2008, 0801.1725. doi: 10.1103/PhysRevD.77.074502,10.1103/PhysRevD.77.07450210.1103/PhysRevD.77.099902,10.1103/PhysRevD.77.099902.

[53] A. Jakovac, P. Petreczky, K. Petrov, and A. Velytsky. Quarkonium correlators and spectral functions at zero and finite temperature. *Phys.Rev.*, D75:014506, 2007, hep-lat/0611017. doi: 10.1103/PhysRevD.75.014506.

[54] Shamit Kachru, Renata Kallosh, Andrei D. Linde, and Sandip P. Trivedi. De Sitter vacua in string theory. *Phys.Rev.*, D68:046005, 2003, hep-th/0301240. doi: 10.1103/PhysRevD.68.046005.

[55] F. Karsch and H.W. Wyld. Thermal Green's Functions and Transport Coefficients on the Lattice. *Phys.Rev.*, D35:2518, 1987. doi: 10.1103/PhysRevD.35.2518.

[56] P. Kovtun, Dan T. Son, and Andrei O. Starinets. Viscosity in strongly interacting quantum field theories from black hole physics. *Phys.Rev.Lett.*, 94:111601, 2005, hep-th/0405231. doi: 10.1103/PhysRevLett.94.111601.

[57] Mikko Laine. Thermal field theory, 2007. lecture notes.

[58] Lüscher, Martin. Properties and uses of the Wilson flow in lattice QCD. *JHEP*, 1008:071, 2010, 1006.4518. doi: 10.1007/JHEP08(2010)071.

[59] Lüscher, Martin and Wolff, Ulli. HOW TO CALCULATE THE ELASTIC SCATTERING MATRIX IN TWO-DIMENSIONAL QUANTUM FIELD THEORIES BY NUMERICAL SIMULATION. *Nucl.Phys.*, B339:222–252, 1990. doi: 10.1016/0550-3213(90)90540-T.

[60] M. Luscher and P. Weisz. On-Shell Improved Lattice Gauge Theories. *Commun.Math.Phys.*, 97:59, 1985. doi: 10.1007/BF01206178.

[61] Martin Luscher. Trivializing maps, the Wilson flow and the HMC algorithm. *Commun.Math.Phys.*, 293:899–919, 2010, 0907.5491. doi: 10.1007/s00220-009-0953-7.

[62] Martin Luscher and Peter Weisz. Locality and exponential error reduction in numerical lattice gauge theory. *JHEP*, 0109:010, 2001, hep-lat/0108014. doi: 10.1088/1126-6708/2001/09/010.

[63] Martin Luscher and Peter Weisz. Perturbative analysis of the gradient flow in non-abelian gauge theories. *JHEP*, 1102:051, 2011, 1101.0963. doi: 10.1007/JHEP02(2011)051.

[64] Simon Mages. Hadronic spectral functions in the qcd transition region - scale setting and anisotropy parameters for lattice qcd simulations. Master's thesis, University of Regensburg, 2011.

[65] Juan Martin Maldacena. The Large N limit of superconformal field theories and supergravity. *Int.J.Theor.Phys.*, 38:1113–1133, 1999, hep-th/9711200. doi: 10.1023/A:1026654312961.

[66] Harvey B. Meyer. The Yang-Mills spectrum from a two level algorithm. *JHEP*, 0401:030, 2004, hep-lat/0312034. doi: 10.1088/1126-6708/2004/01/030.

[67] Harvey B. Meyer. A Calculation of the shear viscosity in SU(3) gluodynamics. *Phys.Rev.*, D76:101701, 2007, 0704.1801. doi: 10.1103/PhysRevD.76.101701.

[68] Harvey B. Meyer. A Calculation of the bulk viscosity in SU(3) gluodynamics. *Phys.Rev.Lett.*, 100:162001, 2008, 0710.3717. doi: 10.1103/PhysRevLett.100.162001.

[69] Harvey B. Meyer. Transport properties of the quark-gluon plasma from lattice QCD. *Nucl.Phys.*, A830:641C–648C, 2009, 0907.4095. doi: 10.1016/j.nuclphysa.2009.09.053.

[70] Harvey B. Meyer. The Bulk Channel in Thermal Gauge Theories. *JHEP*, 1004:099, 2010, 1002.3343. doi: 10.1007/JHEP04(2010)099.

[71] Christopher Michael and A. McKerrell. Fitting correlated hadron mass spectrum data. *Phys.Rev.*, D51:3745–3750, 1995, hep-lat/9412087. doi: 10.1103/PhysRevD.51.3745.

[72] Müller, Berndt. Investigation of Hot QCD Matter: Theoretical Aspects. 2013, 1309.7616.

[73] Guy D. Moore and Kiyoumars A. Sohrabi. Kubo Formulae for Second-Order Hydrodynamic Coefficients. *Phys.Rev.Lett.*, 106:122302, 2011, 1007.5333. doi: 10.1103/PhysRevLett.106.122302.

[74] Guy D. Moore and Kiyoumars A. Sohrabi. Thermodynamical second-order hydrodynamic coefficients. *JHEP*, 1211:148, 2012, 1210.3340. doi: 10.1007/JHEP11(2012)148.

[75] Colin Morningstar and Mike J. Peardon. Analytic smearing of SU(3) link variables in lattice QCD. *Phys.Rev.*, D69:054501, 2004, hep-lat/0311018. doi: 10.1103/PhysRevD.69.054501.

[76] Atsushi Nakamura and Sunao Sakai. Transport coefficients of gluon plasma. *Phys.Rev.Lett.*, 94:072305, 2005, hep-lat/0406009. doi: 10.1103/PhysRevLett.94.072305.

[77] Chiho Nonaka, Masayuki Asakawa, Masakiyo Kitazawa, and Yasuhiro Kohno. Charmonium spectral functions at finite momenta in the gluon plasma from lattice QCD. *J.Phys.*, G38:124109, 2011. doi: 10.1088/0954-3899/38/12/124109.

[78] WHOT-QCD Collaboration, H. Ohno et al. Charmonium spectral functions with the variational method in zero and finite temperature lattice QCD. *Phys.Rev.*, D84:094504, 2011, 1104.3384. doi: 10.1103/PhysRevD.84.094504.

[79] Longgang Pang, Qun Wang, and Xin-Nian Wang. Effect of longitudinal fluctuation in event-by-event (3+1)D hydrodynamics. *Nucl.Phys.*, A904-905: 811c–814c, 2013, 1211.1570. doi: 10.1016/j.nuclphysa.2013.02.140.

[80] P. Petreczky, S. Datta, F. Karsch, and I. Wetzorke. Charmonium at finite temperature. *Nucl.Phys.Proc.Suppl.*, 129:596–598, 2004, hep-lat/0309012. doi: 10.1016/S0920-5632(03)02653-7.

[81] Owe Philipsen and Christian Schäfer. The second order hydrodynamic transport coefficient κ for the gluon plasma from the lattice. *JHEP*, 1402:003, 2014, 1311.6618. doi: 10.1007/JHEP02(2014)003.

[82] Paul Romatschke. Relativistic Viscous Fluid Dynamics and Non-Equilibrium Entropy. *Class.Quant.Grav.*, 27:025006, 2010, 0906.4787. doi: 10.1088/0264-9381/27/2/025006.

[83] S. Sakai, A. Nakamura, and T. Saito. Transport coefficients of quark gluon plasma from lattice gauge theory. *Nucl.Phys.*, A638:535–538, 1998, hep-lat/9810031. doi: 10.1016/S0375-9474(98)00364-9.

[84] Sunao Sakai and Atsushi Nakamura. Transport coefficient of gluon plasma from lattice QCD. *PoS*, LAT2005:186, 2006, hep-lat/0510100.

[85] Edward V. Shuryak. Correlation functions in the QCD vacuum. *Rev.Mod.Phys.*, 65:1–46, 1993. doi: 10.1103/RevModPhys.65.1.

[86] Dominik Steineder, Stefan A. Stricker, and Aleksi Vuorinen. Probing the pattern of holographic thermalization with photons. *JHEP*, 1307:014, 2013, 1304.3404. doi: 10.1007/JHEP07(2013)014.

[87] Hiroshi Suzuki. Energy–momentum tensor from the Yang–Mills gradient flow. *PTEP*, 2013(8):083B03, 2013, 1304.0533. doi: 10.1093/ptep/ptt059.

[88] K. Symanzik. Continuum Limit and Improved Action in Lattice Theories. 1. Principles and phi**4 Theory. *Nucl.Phys.*, B226:187, 1983. doi: 10.1016/0550-3213(83)90468-6.

[89] Derek Teaney. Finite temperature spectral densities of momentum and R-charge correlators in N=4 Yang Mills theory. *Phys.Rev.*, D74:045025, 2006, hep-ph/0602044. doi: 10.1103/PhysRevD.74.045025.

[90] CN WHOT-QCD Collaboration, T. Umeda, H. Ohno, and K. Kanaya. Charmonium dissociation temperatures in lattice QCD with a finite volume technique. 2008, 0810.1567.

[91] CP-PACS Collaboration, T. Umeda et al. Two flavors of dynamical quarks on anisotropic lattices. *Phys.Rev.*, D68:034503, 2003, hep-lat/0302024. doi: 10.1103/PhysRevD.68.034503.

[92] Takashi Umeda. A Constant contribution in meson correlators at finite temperature. *Phys.Rev.*, D75:094502, 2007, hep-lat/0701005. doi: 10.1103/PhysRevD.75.094502.

[93] M.B. Voloshin. Charmonium. *Prog.Part.Nucl.Phys.*, 61:455–511, 2008, 0711.4556. doi: 10.1016/j.ppnp.2008.02.001.

[94] Boram Yoon, Yong-Chull Jang, Chulwoo Jung, and Weonjong Lee. Covariance fitting of highly correlated data in lattice QCD. *J.Korean Phys.Soc.*, 63: 145–162, 2013, 1101.2248. doi: 10.3938/jkps.63.145.

Acknowledgments

This dissertation would not have been possible without all the people around me. First of all, I thank Prof. Andreas Schäfer, who has accompanied all the steps of this thesis, pointed me to ever new and interesting physics projects and engaged me in the collaborations on the lattice side with the Wuppertal group and the holography side with the creators of Improved Holographic QCD. I thank my collaborators Prof. Kálmán Szabó and Dr. Szabolcs Borsányi in Wuppertal for fruitful discussions, the access to their lattice QCD codes, and computing resources to run these codes on and Prof. Zoltán Fodor for making this collaboration possible. I thank my collaborators on the holographic side, Prof. Umut Gürsoy, Prof. Elias Kiritsis, and Prof. Francesco Nitti for inviting me to spend an extended period of time at University of Utrecht, at CERN, and at University of Heraklion and for showing me a whole new world outside lattice QCD. In that context I also want to thank Prof. Gerard 't Hooft for creating such a stimulating environment in Utrecht and Prof. Martin Lüscher for inspiring discussions at CERN. I am very grateful to all my fellow students, in particular Rudolf Rödl, Mykhaylo Filipenko, and Jakob Simeth for physics discussions and moral support. My special thanks go to Florian Rappl, for his steady support in all questions of my thesis and for all the fascinating and engaging projects, which we spent a large chunk of our rare spare time on. I also want to thank Prof. Tilo Wettig for introducing me into the fascinating world of high performance computing at the edge of the currently possible and to give me the opportunity to work on the QPACE2 supercomputer project. Moreover, I have to thank the SFB-TRR 55, which has supported all my journeys to enable collaboration with remote researchers, and the Elite Network of Bavaria in the framework of the "Elitestudiengang Physik mit integriertem Doktorandenkolleg" for their continuous accompaniment since my time as an undergraduate. I am grateful to the Studienstiftung des deutschen Volkes for their important financial and ideal support as part of the PhD scholarship. I wish to thank Dr. Gerry Bauer for motivating me years ago to pursue a career in high energy physics. Last but not least, I want to thank my parents for all their continuous and persistent support.